THESIS ON NATURAL AND EXACT SCIENCES B188

Study of Oxygen Vacancy Dynamics in Sc-doped Ceria with NMR Techniques

REIO PÕDER

TUT PRESS

TALLINN UNIVERSITY OF TECHNOLOGY
Faculty of Science
Department of Physics

This dissertation was accepted for the defence of the degree of Doctor of Philosophy in Engineering Physics on June 10, 2015

Supervisors: Dr. Juhan Subbi, senior research scientist, National Institute of Chemical Physics and Biophysics, Tallinn, Estonia

Dr. Pavel Suurvarik, associate professor, Director of Department of Physics, Tallinn University of Technology, Estonia

Opponents: Dr. Mihails Kusnezoff, Head of Department of Materials and Components, Fraunhofer IKTS, Dresden, Germany

Dr. Indrek Kivi, research scientist, Institute of Chemistry, University of Tartu, Estonia

Defence of the thesis: August 18, 2015

Declaration:

Hereby I declare that this doctoral thesis, my original work, submitted for the doctoral degree at Tallinn University of Technology, has not been submitted for any academic degree before.

/Reio Põder/

ISSN 1406-4723
ISBN 978-9949-23-815-6 (publication)
ISBN 978-9949-23-816-3 (PDF)

LOODUS- JA TÄPPISTEADUSED B188

Hapniku vakantsi dünaamika uurimine Sc-lisandiga tseeriumdioksiidis TMR abil

REIO PÕDER

TTÜ
KIRJASTUS

CONTENTS

LIST OF PUBLICATIONS INCLUDED IN THIS THESIS

Publication 1

J. Subbi, I. Heinmaa, R. Põder, H. Kooskora, *Solid state NMR investigation of oxygen dynamics in scandium doped ceria in 50 K to 1073 K temperature range*, Solid State Ionics 225 (2012) 488-492.

Publication 2

J. Subbi, I. Heinmaa, R. Põder, H. Kooskora, *Solid state NMR spin-lattice relaxation investigation of oxygen dynamics in scandium doped ceria from 60 to 1073 K*, Solid State Ionics 239 (2013) 15-20.

Publication 3

Reio Põder, Juhan Subbi, Helgi Kooskora, Ivo Heinmaa, *Vacancy association energy in scandium doped ceria: ^{45}Sc MAS NMR and 2D exchange spectroscopy study*, Solid State Ionics 267 (2014) 49-53.

Author's contribution

Publication 1: the author participated in planning and performing the experiments, analysed the data, and participated in writing of the article.

Publication 2: the author participated in planning and performing the experiments, analysed the data, and participated in writing of the article.

Publication 3: the author participated in planning and performing the experiments, analysed the data, and wrote the main part of the article.

INTRODUCTION

Solid state electrolyte based ionic conductors have a variety of applications in today's technical solutions, e.g. in gas sensors (Stefanik *et al.* 2001; Moos *et al.* 2011), fluorescent screens (Gomes, Serra 2008; Taniguchi *et al.* 2012), solid oxide fuel cells (Inaba, Tagawa 1996; Kilner 2000; Malavasi *et al.* 2010). Doped ceria is one of those electrolytes. Assumably, its widest field of application today is catalysts in car engine exhaust systems (Trovarelli *et al.* 1999; Gorte 2010), but from the future perspective, it may be part of solid oxide fuel cells where this material has some important advantages over other ionic conductors.

In most electrochemical applications, good charge transport properties, i.e. good ionic conductivity, is required. Ionic conductivity is determined by the concentration of the mobile ions and by their mobility in the crystal lattice of the electrolyte. In the macroscopic approach, i.e. the lattice-wide conductivity and its dependence on the dopant concentration and temperature, the ionic conductors are well studied and known. But there is limited knowledge about mobility and the mechanisms which determine it on the microscopic scale.

A method widely used for investgating the solid ionic conductors experimentally is conductivity measurement by impedance techniques. This method provides macroscopic data. On the atomic level, the nuclear magnetic resonance (NMR) is almost the only tool. In addition, calculations and simulations provide information about energy barriers, interactions and other details important for understanding the mobility of ions. The higher the computing power and the amount of experimental data, the more effective the computational methods are. Today they are an important tool.

Different dopants have different impact on the conductivity. Scandium Sc as a dopant in ceria is known to cause low conductivity. The reasons for that are low solubility of Sc in ceria due to ion size mismatch, which as a result, has a low dopant concentration, and high binding energy between Sc ions and oxygen vacancies, which diminishes the mobility. Because of this high binding energy, scandium doped ceria (SDC) is a model for a low conductivity solid electolyte with strongly bound charge carriers. In the ceria doped with several dopants Sc serves as the oxygen vacancy collector. The aim of this study was to determine experimentally the association energy between Sc and oxygen vacancies in SDC, and to measure the energy barrier heights for vacancy movement in the vicinity of the Sc ions. The results are presented in three articles. In article 1, NMR line

shape analysis was performed on SDC spectra which revealed processes involving vacancy movement. In article 2, spin-lattice relaxation analysis was made to find activation energies of the processes in the lattice. In article 3, the activation energy of the lattice-wide movement of oxygen vacancies was determined with two-dimensional NMR spectrometry.

In this thesis, first solid ionic conductors, particularly doped ceria, are reviewed. The potential energy landscape in doped ceria is covered, and the parameters from previous studies are presented. Next, the NMR spectrometry is explained, with emphasis on topics and methods used in this work. Finally, the results of the work are described and commented. The appendix contains the three articles involved.

ABBREVIATIONS

BPP	Bloembergen, Purcell and Pound (authors of NMR relaxation theory)
DFT	Density functional theory
EXSY	Exchange spectroscopy
FID	Free induction decay
MAS	Magic angle spinning
NMR	Nuclear magnetic resonance
SDC	Scandium doped ceria
SEM	Scanning electron microscope
SOFC	Solid oxide fuel cell
ssb	Spinning sideband

1. THEORETICAL BACKGROUND AND LITERATURE OVERVIEW

1.1. Ceramic ionic conductors

One of the characteristic properties of ceramics is related to diffusion and conductivity. This quality is very important also from the point of view of applications. Different ceramic compounds have diverse charge transport properties, which vary also with external conditions. Ceramics can be used in low conductivity applications, e.g. like in insulators used in electrical engineering, or where high conductivity is required, like in fuel cells.

Most ceramic compounds are crystalline, and possess a rigid regular structure. The first prerequisite for charge transport is defects in the crystal structure of a ceramic. The state of a system, e.g. a crystal lattice, is determined by the free energy G, which can be presented as

$$G = G_0 - TS \tag{1}$$

where G_0 is the free energy at the temperature T = 0 K, and S is the entropy. No matter what the exact external conditions are and which parameters the free energy depends on, G_0 is proportional to the potential energy of the system. Every system tends to minimize its free energy. If $T = 0$ K, the free energy can be diminished through diminishing the potential energy in the lattice, which results in regular spacings of components. If $T > 0$ K, the free energy starts diminishing through an increase in entropy. The increase in entropy results in defects in the lattice. Defects increase the potential energy in the lattice but this is neutralized by entropy. There are always defects present in a real crystal lattice.

From the aspect of conductivity in oxygen ion conductors, the defects introducing vacancies are the most important. There are two main groups of such defects – Frenkel and Schottky defects. A Frenkel type defect is a displacement of an ion from its regular position into an interstitial site (Figure 1).

A Schottky defect is the removal of some ions from the lattice (Figure 1). Vacancies will appear on the places left by ions. The charge neutrality in the lattice is retained through the removal of both positive and negative ions in the

stoichiometric ratio. Schottky defects can be introduced in large amounts through doping the lattice with ions of smaller charge than the host ions have.

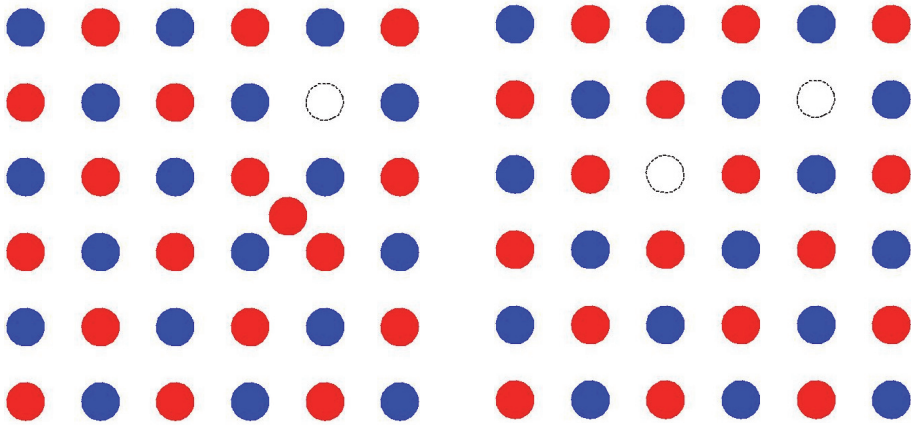

Figure 1. Frenkel (left) and Schottky defect illustrated with a 2D lattice.

Defects introduced through doping are called extrinsic defects. Defects in a lattice without impurities are called intrinsic defects. Vacancies create space for ions to move in the lattice (when ions and vacancies exchange places, for formal comfort it is often said that vacancies move), and mass transport can take place.

The fundamental mechanism behind transport in the lattice is based on diffusion. Directed diffusive movement in the lattice arises when there is a chemical potential gradient for the moving particles (e.g. vacancies), and the particles have enough energy to move. A general law describing these relations is the Fick's first law:

$$J = -D\frac{dC}{dx} \tag{2}$$

where J is the particle flux, C is the particle concentration, $\frac{dC}{dx}$ is the particle concentration gradient in the direction x, and D is the diffusion coefficient or diffusivity (Chiang *et al.* 1997). The diffusion coefficient is measured in area per time, and it depends on the temperature as

$$D = D_0 \exp\left(\frac{-E_a}{RT}\right) \tag{3}$$

where R is the universal gas constant, T is the temperature, E_a is the activation energy of the diffusive process, and D_0 is a constant consisting of the particle's vibrational frequency ν, the lattice constant λ, the number of surrounding sites where the particle can move into N_{sites}, and the entropy change associated with the movement ΔS_{move}:

$$D_0 = \frac{1}{N_{\text{sites}}} \lambda^2 \nu \exp\left(\frac{\Delta S_{\text{move}}}{k}\right) \tag{4}$$

where k is the Boltzmann coefficient. The diffusion coefficient can also be presented in the form

$$D = \frac{1}{N_{\text{sites}}} \lambda^2 \nu_{\text{jump}} \tag{5}$$

where ν_{jump} is the jump frequency of the diffusing particle into a neighbor site. The jump frequency is the product of the vibrational frequency of the particle, and the probability of the jump, which is determined by the energy barrier for the jump (that depends on the material, structure, and interactions inside the material) and by the energy the particle has (i.e. the temperature, as a result).

The diffusion coefficient determines the electrical mobility μ of the particle in a particular environment:

$$\mu = \frac{qD}{kT} \tag{6}$$

where q is the charge of the particle. The electrical mobility is defined as the velocity of the moving charged particle per electric field, the unit is $\frac{\text{m}^2}{\text{Vs}}$ where m is meter, V is voltage, and s is second.

The electrical mobility is directly related to the electrical conductivity σ:

$$\sigma = cq\mu \tag{7}$$

where c is the concentration of the particles. Electrical conductivity is measured in Siemens per meter S/m, sometimes expressed as 1/Ωm. Electrical conductivity is the parameter that determines the usability of the ionic conductor in applications.

It follows from equation (7) that the electrical conductivity is proportional to the concentration of conducting particles, e.g. vacancies, or to the level of doping of the material, if the conducting particles are introduced by doping.

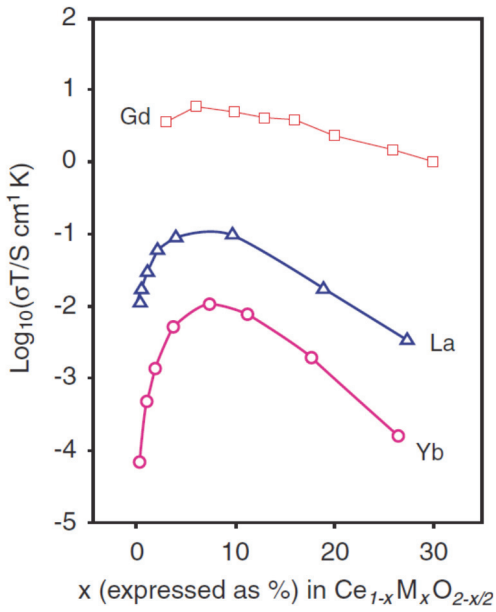

Figure 2. Conductivity dependence on the doping level (Skinner, Kilner 2003).

This is actually true in the case of low doping levels (Fig. 2). Conductivity is diminished at high doping levels through defect interactions and elastic strains introduced into the lattice by deformations occurring with doping (Skinner, Kilner 2003). For this reason, a maximum in conductivity always appears when the doping level is changed. But the conductivity can be enhanced by using dopants with an ionic radius similar to the replaced host ions. This diminishes the lattice deformations and supports conductivity but it does not change qualitatively the dependence of conductivity on the doping level, the maximum in the conductivity remains.

1.2. Ceria

Ceria CeO_2 is a crystalline material with the fluorite structure (Fig. 3). Cerium cations build up a face centered cubic sublattice, and oxygen anions have a cubic arrangement. In a perfect lattice, every cerium ion is surrounded by eight oxygen ions, and every oxygen ion is surrouded by four cerium ions, which are positioned tetrahedrally around the oxygen. Oxygen ions have a cubic arrangement around cerium ions.

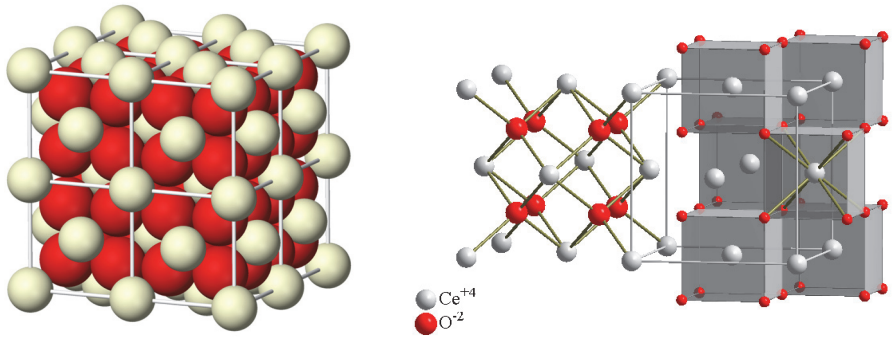

Figure 3. Ceria lattice. Red is oxygen and white is cerium.

Defects in ceria depend on several influences. One parameter of practical importance is the partial pressure P_{O_2} of oxygen around ceria. If the partial pressure of oxygen is low in the environment of ceria and the temperature is high enough to make oxygen mobile in the ceria lattice (beginning from around 300 ^{o}C), then oxygen ions start diffusing out of ceria and disjoint as gaseous oxygen. Oxygen vacancies are left into the lattice, and electrons from vacant oxygen ions reduce Ce^{4+} ions into Ce^{3+}. The process in the Kröger-Vink notation:

$$O_O^X = V_O^{\cdot\cdot} + 2Ce'_{Ce} + \frac{1}{2}O_2(g) \tag{8}$$

It is apparent that for every oxygen vacancy, two cerium cations are turned to Ce^{3+} because every oxygen leaves two electrons into the lattice. These electrons are weakly bonded by cerium ions and cause electronic conductivity. This is what happens on the anode side of a SOFC with a ceria based electrolyte. The partial pressure of oxygen is low at the anode, and quasi-free electrons are introduced into the electrolyte as a result. The concentration of electrons and the electronic conductivity are higher at the anode side (Riess 1981) but electrons

can move through the whole electrolyte to the cathode side. This diminishes the efficiency of ceria based SOFCs because the electrons that go to the cathode directly through the electrolyte are doing no usable work in the external circuit.

Ionic conductivity of ceria is enhanced by doping with aliovalent dopants, e.g. with gadolinium:

$$Gd_2O_3 \rightarrow 2Gd'_{Ce} + V_O^{\cdot\cdot} + \frac{1}{2}O_2(g) \quad (9)$$

Gadolinium ions Gd^{3+} have a smaller positive charge than the cerium ions Ce^{4+}, and at every lattice site where cerium is replaced with gadolinium, a negative charge -1 appears because the negative charges are not balanced with positive charges at that point. For every two gadolinium ions introduced, one oxygen ion leaves the lattice. The oxygen vacancy has a positive charge +2 compared to the regular lattice because positive charges are unbalanced at the location of vacancy. That retains the electroneutrality of the lattice.

The oxygen vacancies turn mobile at high temperatures, and doped ceria is useable as an ionic conductor. Ceria has considerable ionic conductivity at much lower temperatures than e.g. zirconia, already around 500 ^oC, but mainly due to the undesireable electronic conductivity in reducing conditions it is not considered a better electrolyte for fuel cells.

The preferable dopants for ceria are gadolinium Gd and samarium Sm due to their ionic radius similar to Ce.

1.3. Coordination spheres and energy barriers

Cerium ions in the ceria lattice are surrounded by eight oxygens. It means that in case of doped ceria, there are eight possible sites for an oxygen vacancy in the nearest neighborhood around a trivalent dopant. In the next nearest neighborhood, i.e. in the second coordination sphere around the dopant, there are 24 sites. A coordination sphere is a set or amount of lattice positions with the same distance from the dopant. The lattice constant of ceria is 5.41 Å, and the distance from the dopant (or the Ce^{4+} ions, in the case of undoped lattice) to the sites of the first coordination sphere is around 2.34 Å, depending on the lattice distortion. Depending on the dopant and the way it distorts the lattice, some coordination spheres around the dopant are energetically more favorable for a

vacancy to inhabit than other ones. On the potential energy landscape of the doped lattice (Fig. 4), potential holes and barriers can be distinguished. Potential holes are located between potential barriers. The potential energy near a vacancy is different from the energy in the undoped lattice. The corresponding energy difference is the association energy E_{asso} between the dopant and the vacancy. Energy barrier is the energy needed by the vacancy for moving from one site to another. The energy barrier height in the vicinity of a dopant can be different from the barrier height in the undoped lattice E_{bulk}. It means that the vacancy movement in the limits of one coordination sphere may have a different activation energy than the movement further in the lattice.

In order to move long distances in the lattice, the vacancy bound to a dopant needs to exit from the potential hole near the dopant and to overcome the energy barrier of the undoped ceria lattice. So, the activation energy for the latticewide movement of vacancies E_{a} is the sum of the association energy and the energy barrier height of the undoped lattice: $E_{\mathrm{a}} = E_{\mathrm{asso}} + E_{\mathrm{bulk}}$ (Fig. 4).

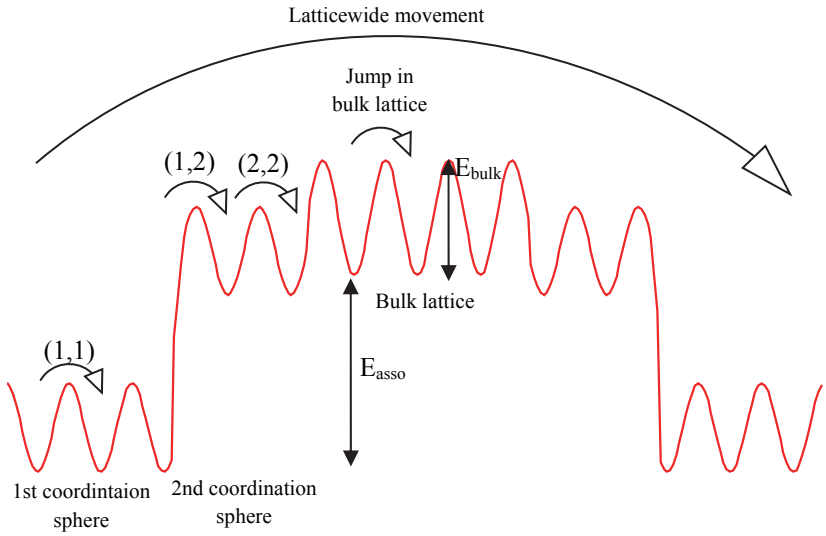

Figure 4. Idea of the potential landscape between two dopants (on the ends of the plot). Denotation (*a*,*b*) shows vacancy movement from sphere *a* to sphere *b*. E_{bulk} and E_{asso} present energy barrier heigth in the bulk lattice and association energy between vacancy and dopant, respectively.

The energy needed for the latticewide movement can be determined experimentally, e.g. with conductivity measurements. On the microscopic level,

the vacancy movement is hopping between the lattice sites, and to find the energies required for jumping over particular barriers, more selective and local measurements than conductivity are needed, e.g. NMR. The measurement of E_{bulk} is very difficult in practice because in the undoped lattice, the concentration of vacancies and conductivity are very low. Currently, the latest estimation of E_{bulk} in the ceria lattice is 0.47 eV (Dholabhai, Adams 2012). The distribution of the association energy between different coordination spheres is also difficult to determine experimentally. There are no universal and effective methods for that. However, here modeling and calculations provide some help.

Figure 5 from (Dholabhai, Adams 2012) shows the top view of a part of a doped ceria lattice and vacancy migration paths in the first three coordination spheres of a dopant, and Table 1 presents the activation energies of movements in these paths calculated by different authors with the DFT + U method for different dopants. The doping level of the modeled sample is shown by the source reference.

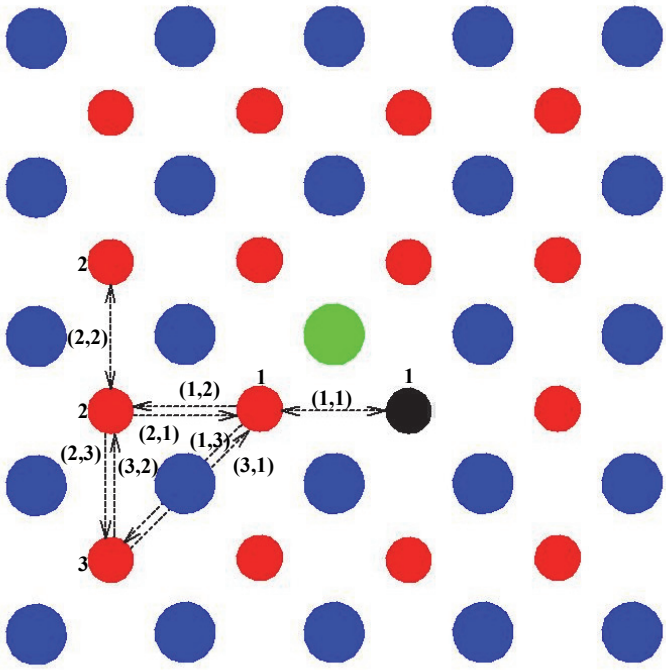

Figure 5. Blue is Ce, green is a trivalent dopant, red is O, and black is an oxygen vacancy. Numbers 1, 2, and 3 represent coordination spheres of the dopant. Denotation (*a*,*b*) shows vacancy movement from sphere *a* to sphere *b*.

Table 1. Calculated energies (in eV) required for vacancy movement for different dopants. The letters a-e refer to the following sources: a) Dholabhai, Adams 2012; b) Nakayama, Martin 2009; c) Andersson *et al.* 2006; d) Wang *et al.* 2013; e) Ismail *et al.* 2011. The doping level used in the corresponding calculation is shown by the reference (per cents).

Path	Ref./doping level	Sc	Y	Gd	Sm	Pr	La
1 → 1	a / 6.25%			0.59	0.66	0.78	
	b / 3%	0.32	0.53	0.56	0.64		0.84
1 → 2	a / 6.25%			0.5	0.47	0.41	
	b / 3%		0.6				
	c / 6.25%			0.52	0.44	0.29	0.2
	d / 18.75%		0.34	0.4	0.45	0.51	0.55
	e / 3.2%				0.48		
2 → 1	a / 6.25%			0.36	0.4	0.43	
	b / 3%		0.26				
	c / 6.25%			0.32	0.38	0.46	0.42
	d / 18.75%		0.68	0.75	0.73	0.66	0.65
	e / 3.2%				0.4		
1 → 3	a / 6.25%			2.61	2.69	2.79	
3 → 1	a / 6.25%			2.46	2.56	2.69	

If the goal is to determine the potential barriers for vacancy transitions, either experimentally or through calculations, low doping levels are more suitable. If the doping level is high, coordination spheres of different dopant ions are getting closer or overlap, and movements from a particular coordination sphere into a further sphere or into the lattice cannot be observed, and neither can the corresponding energies be determined. For the same reason the computations cannot be made in very small lattice models because there is not enough space for different coordination spheres.

As seen in Table 1, there is almost no data for Sc doped ceria. That motivated to determine experimentally the energies for vacancy movement in SDC, particularly in the first coordination sphere (path 1→1) and for macroscopic vacancy movement, i.e. to determine the association energy E_{asso} in SDC. The energy barrier height in the first coordination sphere refers to the state of lattice around the dopant. For instance, if the barrier is low, then there is space for the vacancy to move around the scandium ion. The association energy, on the other hand, determines the perspective to use the material as an ionic conductor. In

addition, there are experimental methods available to determine these values plausibly. Experimental data for SDC have been scarce, and experiments give input and references also for the calculational approach.

2. EXPERIMENTAL

2.1. Samples and synthesis

Sc doped ceria samples were produced with solution combustion synthesis. This is a relatively new method that allows nanoscale materials to be produced fast and easily in a single step. The essence of this process is exothermic redox reactions between metal nitrates and a fuel. In this study, glycine-nitrate combustion and citrate-nitrate combustion were used, where glycine and citric acid were fuels, respectively.

The ingredients for the synthesis were:
Cerium(III) nitrate hekshydrate of 99.99% purity from Aldrich
Scandium(III) nitrate of 99.99% purity from Alfa Aesar
Niobium(V) chloride of 99.95% purity from Alfa Aesar
Yttrium(III) nitrate of 99.9% purity from Alfa Aesar
Citric acid of 99.5% purity from Sigma-Aldrich company
Glycine of 99.5% purity from Alfa Aesar

In the citrate-nitrate method (Singh *et al.* 2006), cerium nitrate and dopant nitrates (chloride in the case of Nb) were dissolved in doubly distilled water (2 mol/l). Their ratios were chosen for doping levels of 0.2%, 0.5%, 1%, and 5%. Citric acid solution was added to the solution of nitrates, 2 mol citric acid per 1 mol of metal cations. Gelation under stirring at 80 ^{o}C takes two hours, then with the temperature raising, the water evaporates, solution becomes more viscose, and after simultaneous elimination of water and nitric oxides, the combustion of organics starts. The resulting powder was pyrolysed at 500 ^{o}C for three hours.

In the glycine-nitrate method (Rocha *et al.* 2003), cerium nitrate and dopant nitrate ratios were calculated for doping levels of 0.2%, 0.5% and 1%, and nitrates were dissolved in doubly distilled water. Glycine (0.7-0.8 mol per 1 mol nitrate) was dissolved separately and added under stirring to the solution. The solution was heated to evaporate water. At the temperature of 200-300 ^{o}C, the resulting viscous liquid swelled, autoignited and went through highly exothermic picturesque combustion, converting the precursor materials into fine nanopowder. The synthesized powders were pyrolysed at 500 ^{o}C for three hours. After that, the powders were calcined at different temperatures up to 1600 ^{o}C. For temperature dependent non-spinning NMR measurements, the powders were

pressed isostatically and sintered for three hours at 1600 °C into 20 mm rods with a diameter of 5 mm.

2.2. Grain size and properties of ceria powders

When doping CeO_2 with a trivalent dopant like Sc, for every two dopant ions one oxygen vacancy is introduced into the ceria lattice. Sc ions bind oxygen vacancies, and as there are twice as many Sc dopant ions as oxygen vacancies in the lattice, half the Sc ions can bind a vacancy into their neighborhood, and the other half cannot. The Sc ions coupled with a vacancy (7-coordinated Sc, because they are surrounded by seven oxygen ions and one vacancy) and the Sc ions without a vacancy (8-coordinated Sc, surrounded by eight oxygen ions) have different shieldings in the magnetic field, and so there are two different peaks in the NMR spectrum of Sc doped ceria (Fig. 6) – one at 20 ppm, corresponds to 7-coordinated Sc, the other at -35 ppm, to 8-coordinated Sc.

Sintering the powders at higher temperatures increases the grain size (Fig. 7). This influence is apparent also in Figure 6. In the case of small grain sizes (corresponding to lower temperatures), the peak of 7-coordinated Sc is missing or small. In nanosize powders (grain size ~25 nm), all the vacancies are bound by grain surfaces, and there are no 7-coordinated Sc in the lattice.

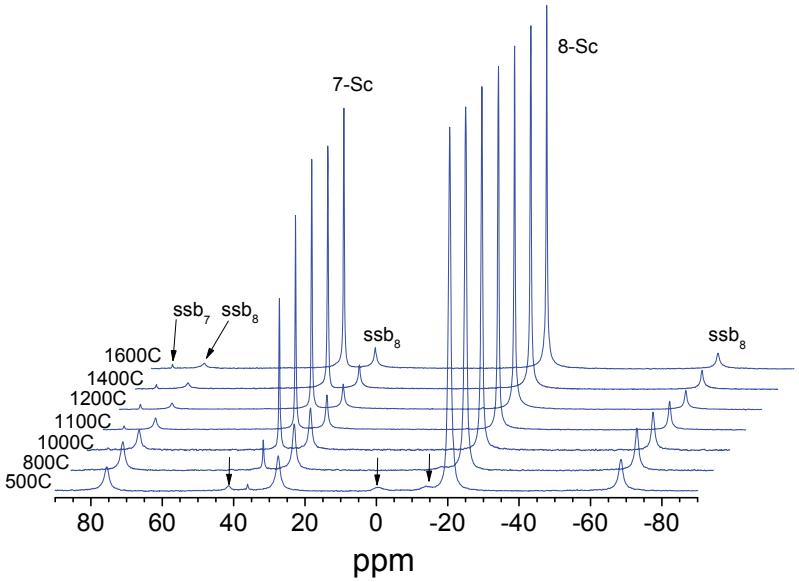

Figure 6. Dependence of 0.5% SDC MAS (Hz) NMR spectra on the SDC sintering temperature (500 – 1600 °C, shown left). Arrows show spinning sidebands.

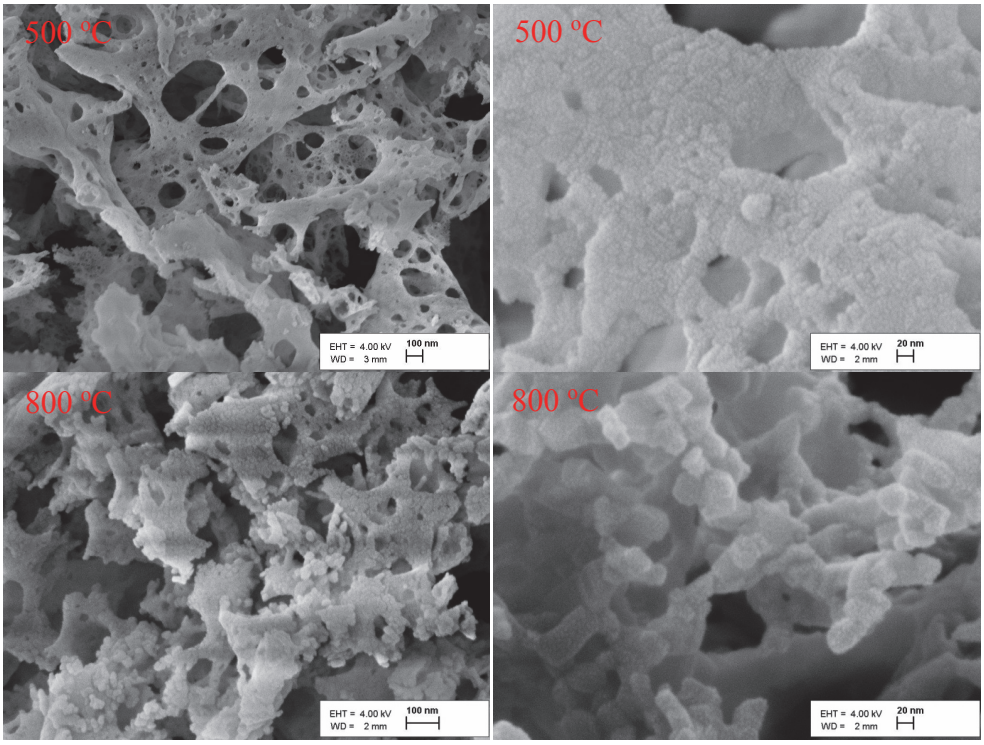

Figure 7. SEM pictures of 0.5% SDC. Probes are covered with gold for viewing with SEM.

It is remarkable that the spinning sidebands of the 8-coordinated Sc are large at low temperatures, and diminish as the temperature rises. It might be a sign that in the case of small nanosize grains, the lattice is more deformed and has additional asymmetries and unbalanced quadrupolar couplings. When the grains are larger, and vacancies are beside scandium ions, the lattice is more symmetric, and quadrupolar interactions are balanced out.

2.3. Sc solubility in ceria

As Sc^{3+} is small compared to Ce^{4+}, it does not fit into the ceria lattice in large amounts. If the doping level is increased, dimers are formed where one vacancy is bound to 2 Sc. Such multiple-Sc complexes create a small wing to the line of 7-coordinated Sc (Fig. 8). If the doping level is increased further, Sc_2O_3 clusters appear in the material as small crystallites, and a line for Sc_2O_3 appears in the spectrum (Fig. 8).

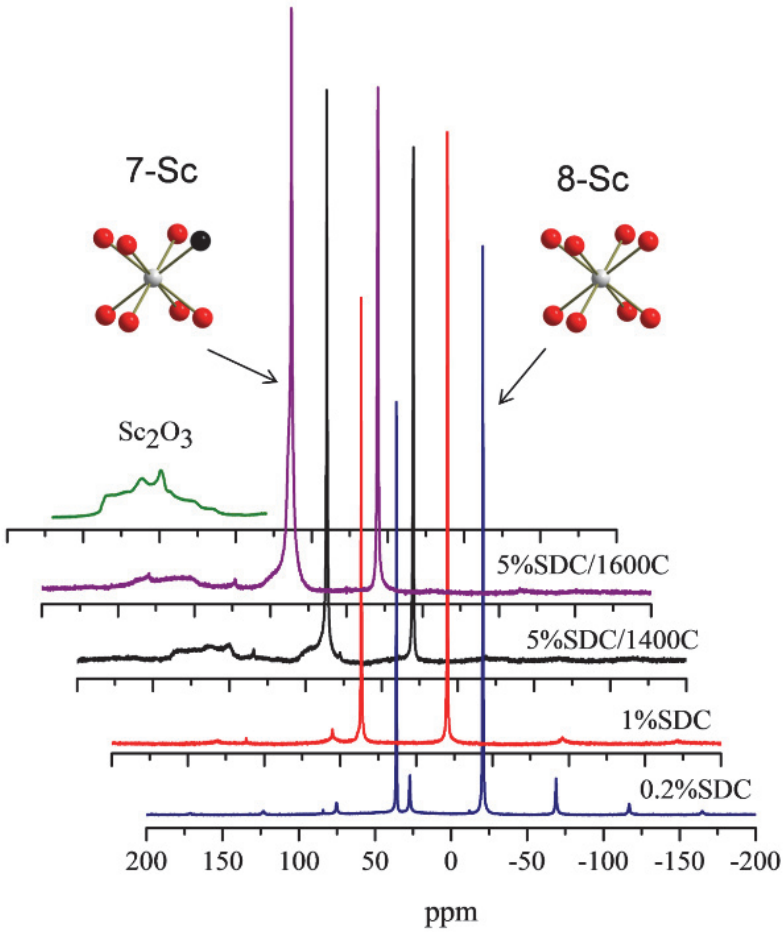

Figure 8. SDC spectra with different doping levels. At the doping level of 5%, Sc appears not to be completely dissolved - Sc_2O_3 clusters and multiple-Sc complexes appear.

Estimably, the solubility of Sc in ceria is 2 mol%. Randomly distributed single Sc ions in the lattice are achievable until that doping limit when using combustion synthesis. As the solubility is so low, this limit can easily be disregarded where NMR spectra of Sc doped ceria are not measured. Unlike many other methods, NMR shows the exceeded solubility limit very clearly.

3. SOLID STATE NMR TECHNIQUES

3.1. 1D Spectrometry

Solid state nuclear magnetic resonance spectrometry is special because it is strongly influenced by intrinsic interactions in the measured sample or material. Because the structure of solids is mainly static, there are interactions which are not averaged out like in liquids and may have a dependency on directions. Nuclei with spins larger than ½ are involved in the quadrupolar interaction which, when present, is the strongest and has the greatest influence on spectra in solids. Other important interactions in solids are dipolar coupling and chemical shielding. In some cases, there may be other interactions, e.g. *J*-coupling or in other words, indirect nuclear spin-spin coupling in some molecular structures and interactions related to the magnetism of the sample.

3.1.1. Chemical Shift

External magnetic field induces electron currents in the orbitals of atoms and molecules, through which local magnetic fields arise, which vary according to electron density in the material. The induced local fields are opposite to the external field, and in effect cause shielding against the external field.

As the positions of electron currents depend on the shape of the molecules and their orientation in the field, the external field and induced local fields are in general not aligned parallel.

Local field $\boldsymbol{B}^{\text{local}}$ in a site i is related to the external field $\boldsymbol{B}_0$ through the chemical shift tensor δ^{i}:

$$\boldsymbol{B}_{\text{i}}^{\text{local}} = (1 - \delta^{\text{i}})\boldsymbol{B}_0 \tag{10}$$

In solid state NMR spectrometry, the sample is usually polycrystalline, a single piece of a polycrystal, or a powder with polycrystalline grains. As there are all crystallite orientations present, many different chemical shifts are introduced into the spectrum. This results in a broad line called the powder line.

Chemical shifts can be averaged into the isotropic chemical shift with sufficiently fast motion. In liquids, it is achieved through the Brownian motion, in solids, fast spinning is used. As a result, a narrow line is achieved.

As Larmor frequencies depend on the magnetic field, spectra measured in different fields are not directly comparable. For this reason, frequencies are often not used in spectra. In order to reduce the dependence on the field, the measured frequency f_{sample} is compared with a reference frequency f_{ref}, and their difference is divided by the reference frequency f_{ref}:

$$\delta = \frac{f_{\text{sample}} - f_{\text{ref}}}{f_{\text{ref}}} \tag{11}$$

This quotient is in order of 10^{-6}, so the chemical shift δ is expressed in units of ppm. Also the reference sample must be mentioned when chemical shift referencing is used. Usually certain standard reference samples are used.

3.1.2. Quadrupolar coupling

Quadrupolar coupling is of a major importance in NMR because of its magnitude. It may be several hundred MHz. Quadrupolar coupling arises from electric rather than from magnetic interactions.

Quadrupolar interaction shifts the energy levels of different spins, causing splitting of spectrum lines. Considering the energy of spins, without the magnetic field and without the quadrupolar interaction, the energy levels according to the spin projection quantum numbers $-I, -I+1, \dots, I$ of a spin I are degenerate. In the magnetic field, these energy levels are separated through the Zeeman interaction (Fig. 9), and consecutive energy levels $E_m^{(0)}$ differ by an equal amount, which also determines the Larmor frequency ω_L:

$$E_m^{(0)} = -h\omega_L m \tag{12}$$

where m is the spin projection quantum number (if the spin is I, then m takes the values $-I, -I+1, \dots, I$).

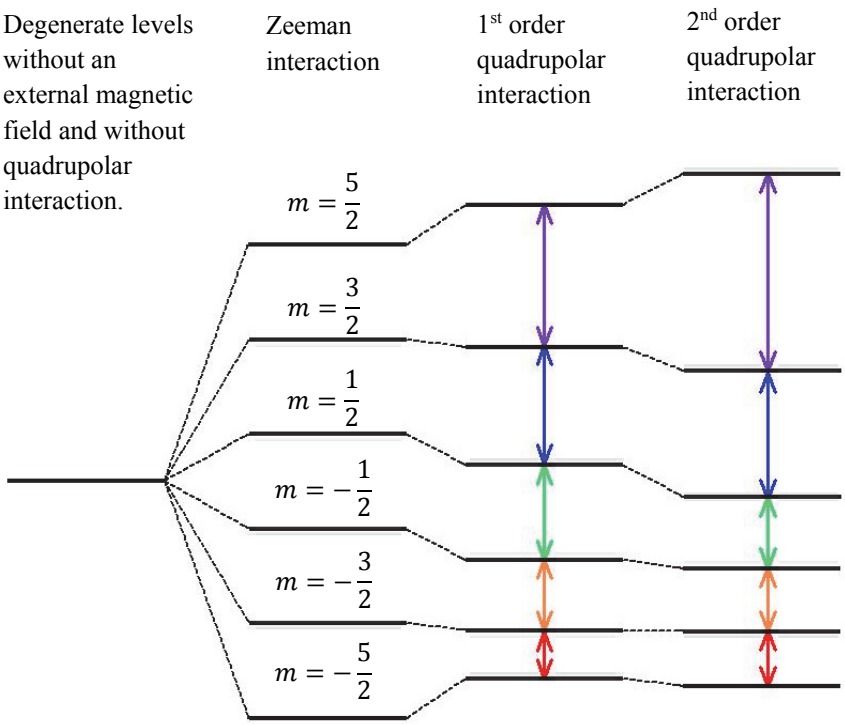

Figure 9. Spin energy levels, exemplified with a spin of 5/2. NOTE: degenerate levels in this figure are shown to illustrate the degenerated state and to demonstrate separately the influence of different interactions. If quadrupolar interaction is present, then the energy levels are shifted even without an external magnetic field, and they are never in such degenerate state.

Transitions between these states give a single line at the frequency ω_L in the spectrum. If the quadrupolar interaction is present, the energy levels are shifted (Fig. 9). Usually there are two orders of the quadrupolar interaction to consider. In the case of a symmetric field gradient, the energy levels resulting from the first order quadrupolar interaction are given as

$$E_m^{(1)} = \frac{3e^2qQ}{8I(2I-1)}(3(\cos\theta)^2 - 1)\left(m^2 - \frac{1}{3}I(I+1)\right) \qquad (13)$$

where Q is the electric quadrupole moment, e is the elementary charge, eq is the largest principal component of the electric field gradient, θ is the

angle between the applied field and the crystal axis. As a result, lines are split in the spectrum (Fig. 10).

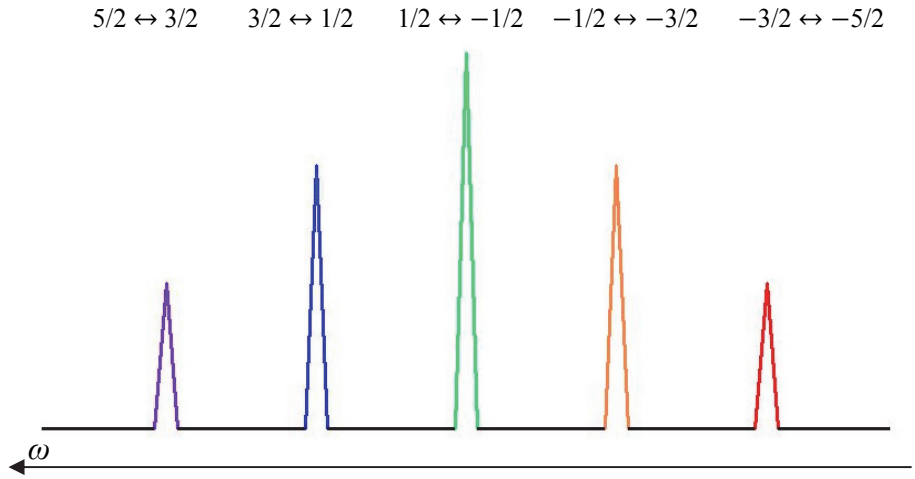

Figure 10. NMR spectrum due to quadrupolar interaction, corresponding to the scheme in Fig. 9.

Such spectrum with separate lines like in Figure 10 corresponds to a monocrystal. If there is a distribution of angles θ in the sample, e.g. in a powder, wide lines appear instead of narrow peaks, covering many different crystal orientations (Fig. 11).

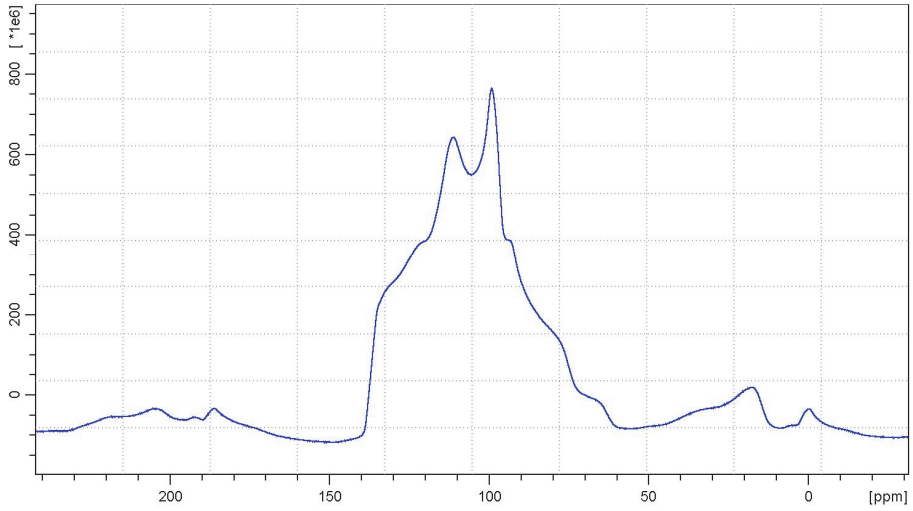

Figure 11. NMR MAS (13600 Hz) spectrum of Sc_2O_3.

Due to the dependence on the angle θ as $3(\cos\theta)^2 - 1$ in (13) it is possible to average the first order quadrupolar interaction out with the magic angle spinning under the angle 54.7°.

Quadrupolar coupling also has a second order term, which shifts the energy levels further and changes also the position of the central line (Fig. 9). The second order quadrupolar coupling can be averaged out by rotating the sample additionally at the angle of 30.6° or 70.1°. Special techniques like double rotation (Samoson *et al.* 1988), dynamic angle spinning (Chmelka *et al.* 1989; Llor, Virlet 1988), or multiple quantum NMR (Frydman, Harwood 1995) have been developed in order to average out both terms.

3.2. Exchange Spectroscopy

2D NMR spectrometry is a method that provides additional data about certain aspects of the spin system not achievable with 1D spectrometry. Many different 2D techniques of NMR are available, all of them designed for different purposes. But in general, 2D NMR is used in order to distinguish between different interactions in the spin system, to identify couplings between spins or to study dynamic processes in the sample (Ernst *et al.* 1997). The last is the case in this thesis where 2D spectrometry is used to study the vacancy exchange between dopant ions. The exact 2D technique is EXSY (Exchange Spectroscopy) developed by Jeener, Meier, Bachmann, and Ernst (Jeener *et al.* 1979).

The EXSY pulse sequence is shown in Figure 12. The pulse P_1 rotates the magnetization to the *xy*-plane where it precesses the time t_1, called the evolution time. The magnetization vectors from different sites dephase during that period.

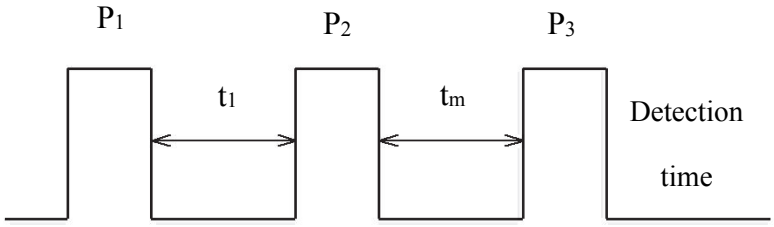

Figure 12. EXSY pulse sequence.

The P_2 pulse rotates the magnetization vectors to the *xz*-plane, and as only the *z*-components of the magnetization are important, the remaining *x*-components are usually removed by the use of a field gradient. Then, the *z*-component remains for the time t_m, called the mixing time, during which spin-lattice relaxation and exchange take place. After time t_m, the magnetization is again rotated to the *xy*-plane with the pulse P_3, and the FID is measured during the detection or acquisition time t_2, after which a FID corresponding to a 1D spectrum is gained.

The evolution time t_1 is varied in the experiment. In the beginning it is zero, then it is increased by small steps, and at every time the full procedure is followed until receiving the FID during the acquisition time. In this way, a large number of FIDs is gained, which build up a so-called 2D FID signal $M(t_1, t_2)$.

The 2D Fourier transform is performed on the data, and a 2D spectrum is obtained (Perrin, Dwyer 1990):

$$S(\omega_1, \omega_2) = \iint M(t_1, t_2) e^{-i\omega_1 t_1} e^{-i\omega_2 t_2} \, \mathrm{d}t_1 \mathrm{d}t_2 \tag{14}$$

where ω_1 and ω_2 are the corresponding frequencies.

The scheme of the resulting spectrum of a probe with two exchanging sites is shown in Figure 13.

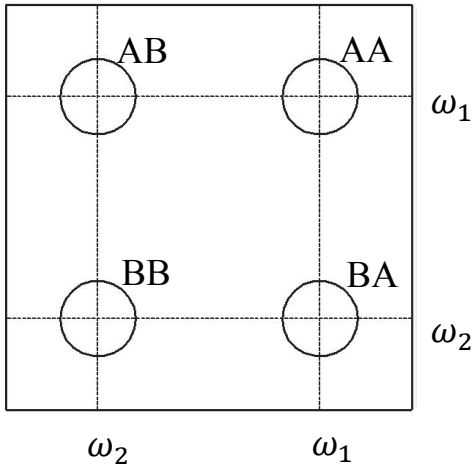

Figure 13. AA and BB are the diagonal peaks, AB is the cross peak of AA, and BA is the cross peak of BB.

The two axes correspond to two measurement times: the evolution time t_1 and the acquisition time t_2. The frequencies of the peaks measured during these times are presented on the frequency axes ω_1 and ω_2, gained through the 2D Fourier transform. The peaks which have the same Larmor frequency on both axes are called the diagonal peaks, and they correspond to the two different sites. If there is an exchange taking place between the two sites during the mixing time, the frequencies of the nuclei taking part of the exchange are different during the two measurement times. A nucleus at the site A produces a peak AA at the frequency ω_A during the time t_1, and after the exchange, a peak AB at the frequency ω_B during the time t_2. A nucleus at the site B taking part in the exchange produces the peaks BB and BA, analogously. The peaks occurring due to exchange are called the cross peaks. As the time t_2 comes after the mixing time, the cross peaks appear on the axis corresponding to t_2, i.e. on the axis of ω_2. The diagonal peaks are produced by the nuclei not taking part in the exchange, and having the same frequency during both t_1 and t_2.

The 2D magnetization $M(t_1, t_2)$ is given as (Jeener *et al.* 1979):

$$M(t_1, t_2) = -\sum_{i,j=\mathrm{A,\,B}} a_{ij}\,(t_\mathrm{m}) \cos\omega_i\, t_1 \cos\omega_j\, t_2 \times e^{-t_1\left(\frac{1}{T_{2i}}+(1-x_i)k\right)} e^{-t_2\left(\frac{1}{T_{2j}}+(1-x_j)k\right)} \tag{15}$$

where A and B are the two sites the exchange takes place between, k is the exchange rate, x_A and x_B are the mole fractions of the sites, t_m is the mixing time, $T_{2\mathrm{A}}$ and $T_{2\mathrm{B}}$ are the transverse relaxation times for sites A and B, respectively.

The mixing coefficients $a_{ij}(t_\mathrm{m})$ determine the integral intensities of the peaks in the 2D spectrum. For the diagonal peaks corresponding to the sites A and B:

$$\begin{aligned} a_{\mathrm{AA}}(t_\mathrm{m}) &= x_\mathrm{A} e^{-\sigma t_\mathrm{m}} \left[\cosh(D t_\mathrm{m}) - \frac{\delta}{D}\sinh(D t_\mathrm{m})\right] \\ a_{\mathrm{BB}}(t_\mathrm{m}) &= x_\mathrm{B} e^{-\sigma t_\mathrm{m}} \left[\cosh(D t_\mathrm{m}) + \frac{\delta}{D}\sinh(D t_\mathrm{m})\right] \end{aligned} \tag{16}$$

and for the crosspeaks:

$$a_{\mathrm{AB}}(t_{\mathrm{m}}) = a_{\mathrm{BA}}(t_{\mathrm{m}}) = x_{\mathrm{A}} x_{\mathrm{B}} \frac{k}{D} e^{-\sigma t_{\mathrm{m}}} \sinh(D t_{\mathrm{m}}) \tag{17}$$

where

$$\begin{aligned} \sigma &= \frac{1}{2}\left(\frac{1}{T_{1\mathrm{A}}} + x_{\mathrm{B}} k + \frac{1}{T_{1\mathrm{B}}} + x_{\mathrm{A}} k\right) \\ \delta &= \frac{1}{2}\left(\frac{1}{T_{1\mathrm{A}}} + x_{\mathrm{B}} k - \frac{1}{T_{1\mathrm{B}}} - x_{\mathrm{A}} k\right) \\ D &= \sqrt{\delta^2 + x_{\mathrm{A}} x_{\mathrm{B}} k^2} \end{aligned} \tag{18}$$

where $T_{1\mathrm{A}}$ and $T_{1\mathrm{B}}$ are the spin-lattice relaxation times for the sites A and B, respectively. Equations (17) and (18) are given for the case where no direct dipolar interaction occurs between the sites A and B, and the dipolar relaxation rate is zero.

Equation (15) is based on the assumption that the exchange is slow, which is the desirable condition for EXSY (Jeener *et al.* 1979). If the exchange is fast, the changes of intensities of the diagonal and crosspeaks cannot be analyzed and fitted with the mixing coefficients $a_{ij}(t_{\mathrm{m}})$ because the exchange process equalizes all peaks rapidly. In this case, it is difficult to achieve information from the spectra, e.g. the exchange rate *k*. If the exchange rate is even faster and approaches the distance of the peaks on the frequency scale, the exchange averages the two peaks into one, and the exchange cannot be seen at all.

The unsuitability for fast exchanges limits the applicability of EXSY to narrow temperature ranges. In SDC measurements, the temperatures of 240 – 300 °C could be used (the lower limit is determined with the activation energy of the exchange process).

Another limitation in practice is that the duration of measurement must be kept in reasonable limits. That diminishes accuracy and can affect the data analysis, so it is necessary to regulate the balance between the quality of data and the duration of measurement in the optimal way in every experiment.

4. NMR HARDWARE

MAS measurements were performed with the Bruker AVANCE-II-600 spectrometer in a 14.5 T magnetic field. Probes were built in-house and used with 4 mm zirconia rotors. Reference compound was $Sc(NO_3)_3$ solution in water.

For measurements with varied temperature the Bruker AMX 360 spectrometer was used. A magnetic field of 8.5 T was used, and for relaxation measurements also a 4.7 T field was used. The saturation recovery pulse sequence was used in relaxation measurements.

The high temperature probe (Fig. 14) was home-built and used with 5 mm quartz ampulas for the substance.

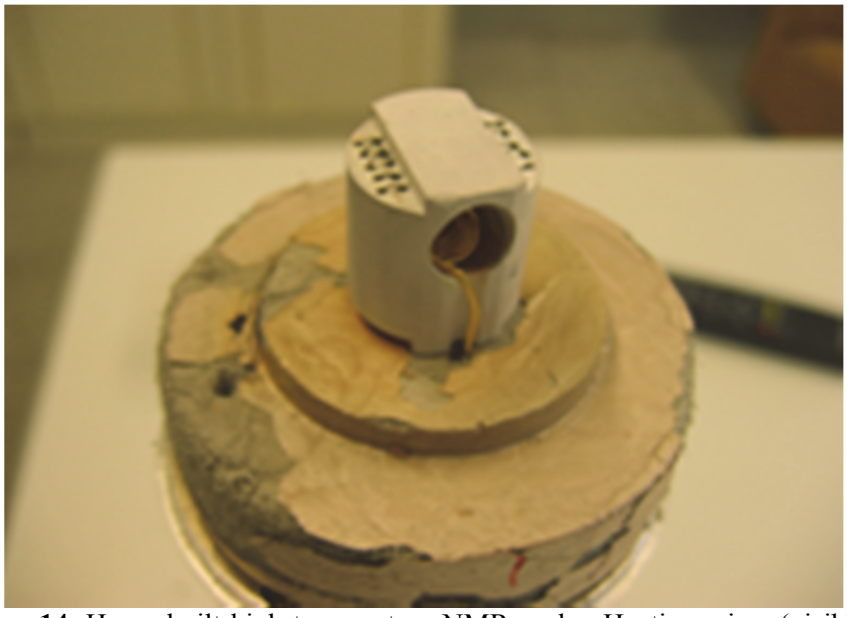

Figure 14. Home-built high temperature NMR probe. Heating wires (visible at sides on top of the probe) surround the coil.

Temperature at the coil was measured with an integrated K-type thermocouple, and kept constant on a desired level with an automatic controller, which regulated the heating current. Temperatures up to 800 ^{o}C were achieved.

Low temperature measurements were carried out with an in-house built probe combined with a He gas flow cryostat from Janis Research Company. The

temperature was regulated manually through changing the gas flow from the He vessel, and measured with a controller from Lake Shore Cryotronics. Temperatures as low as around 4 K were achievable with this setup, but for the experiments in this study, only 50 K was needed.

5. RESULTS

5.1. Overview of the study

Scandium doped ceria $Sc_xCe_{1-x}O_{2-x/2}$ with an x = 0.005 (0.5% SDC) probe was synthesized by the combustion synthesis and measured with NMR spectrometry. Chemical shift and line shape analysis of the spectra was performed, relaxation time temperature dependencies were measured in different magnetic fields, and EXSY measurements were performed for vacancy exchange analysis. Doping level of 0.5% was considered optimal for measuring separate scandium centers, which are available when scandium dopants are distributed randomly in the host lattice. The aim was to

- find the activation energy of the oxygen vacancy exchange between 7- and 8-coordinated Sc in the lattice
- find the activation energy of the vacancy movement in the first coordination sphere of the 7-coordinated Sc
- study the structure of SDC on the atomic level and to determine processes and possible phase transitions taking place in the lattice.

5.2. Vacancy dynamics in SDC [Publications 1, 2]

Scandium spectra in 0.5% SDC were measured at different temperatures between 100 K – 1073 K (Fig. 15).

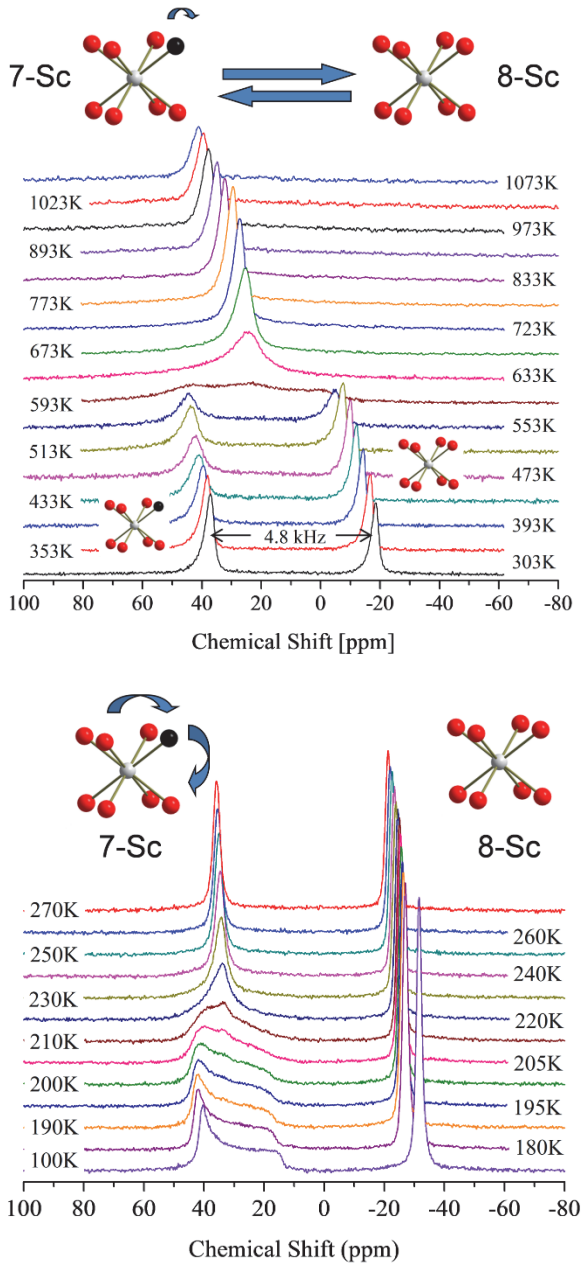

Figure 15. Sc spectra in 0.5% SDC at different temperatures.

There are two lines in the spectra. The line with a larger chemical shift (i.e corresponding to a higher Larmor frequency) belongs to the 7-coordinated Sc ion (which has one oxygen vacancy and seven oxygen ions in its neighborhood) because of smaller shielding due to vacancy, and the other line belongs to the 8-coordinated Sc ion (which has eight oxygen vacancies in its neighborhood). The 8-coordinated Sc line is narrow at all temperatures until around 500 K, i.e. it has a stable symmetric cubic environment which eliminates quadrupolar, dipolar, and chemical shift anisotropies. The 7-coordinated scandium, which has no symmetric environment due to the presence of the vacancy, has a line with a powder pattern shape at low temperatures, which corresponds to the distribution of shieldings, but between 230 K – 500 K it has a narrow line referring to symmetry. The symmetry that appears only at high temperatures is dynamic, it is caused by fast movement of vacancy around the Sc ion, and this averages out all anisotropies, resulting in a narrow line. It is remarkable that such movement begins already at slightly above 200 K. It means that vacancy movement in the nearest neighborhood of the Sc ion has very low activation energy (0.37 eV). At above 500 K, vacancies start moving into the lattice and vacancy exchange between Sc ions begins: both lines broaden and at 633 K, when the vacancy exchange frequency reaches the separation of the two lines on the frequency scale (4.8 kHz), they are averaged into a single line. The fact that the averaged line is in the middle of the two lines shows that the time spent by vacancies in the lattice away from Sc ions is very short, and the ratio of 7-and 8-coordinated Sc ions remains constant.

5.3. Neighborhood of 7Sc [Publication 1]

Low temperature measurements in different magnetic fields provided data about symmetries around the 7-coordinated Sc. Figure 16 shows the spectra measured at the temperature of 150 K in the field of 4.7 T and at 160 K in 8.5 T.

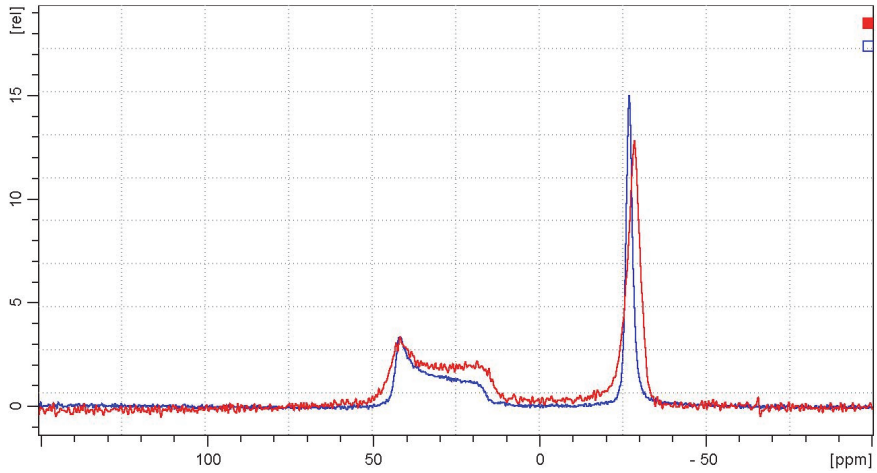

Figure 16. SDC spectra measured at 170 K in the field of 4.7 T (red line) and at 180 K in 8.5 T.

It is apparent that both the lines of the 7-coordinated Sc and 8-coordinated Sc are very similar, there are no large differences in line widths. This refers to zero or a very limited quadrupolar coupling. According to line shape simulations, the quadrupolar coupling constant can be around 1 kHz, which can be the cause of minor differences in line widths of both 7-coordinated and 8-coordinated Sc lines in two different magnetic fields.

The intensity differences in the lower frequency part of the line of the 7-coordinated Sc (the powder line) are caused by small relaxation rate differences in the environments with higher and lower shieldings. Such differences are more influential in lower fields.

In conclusion, the comparison of spectra measured in different fields illustrates that the oxygen cage around the 8-coordinated Sc remains cubic so that the quadrupolar coupling is neutralized, and when the oxygen vacancy movement around the 7-coordinated Sc stops, a structure is formed where quadrupolar interaction is still averaged out. In a work of O. Knop *et. al.* (Knop *et al.* 1975) it is clarified, which configurations are possible in the fluorite lattice to neutralize the quadrupolar coupling.

5.4. Activation energies of processes in SDC lattice [Publication 2]

5.4.1. Theoretical considerations

The energy transfer between nuclear spins and the lattice hosting these spins is achieved through the fluctuations of the local magnetic field caused by the thermal motion of the lattice, leading to the spin-lattice relaxation. The efficiency of this process is proportional to the spectral density of the fluctuations around the Larmor frequency.

If the fluctuations take place in an isotropic uniform medium, the relaxation process can be described by the theory presented by N. Bloembergen, E. M. Purcell and R. V. Pound in 1948 (Bloembergen *et al.* 1948). This theory, called the BPP theory, was developed for liquids with an assumption that nuclei in mutual interaction are moving randomly but it is applicable in solids too when the fluctuations are random and without any biases. According to the BPP theory, the autocorrelation function of the fluctuations decays as $\exp(-t/\tau_c)$, where τ_c is the correlation time, and the spectral density of fluctuations found through the Fourier transform is

$$J(\omega) = F_0^2 \frac{2\tau_c}{1 + \omega^2 \tau_c^2} \tag{19}$$

where F_0 is the amplitude of the fluctuations. The relaxation time depends on the density of the fluctuations at the Larmor frequency ω_L:

$$T_1^{-1} = K[J(\omega_L) + 4J(2\omega_L)] \tag{20}$$

The constant K is the strength of the coupling through which the fluctuations exchange energy with spins. If $J(\omega)$ is given with Eq. (19), then

$$T_1^{-1} = K\left(\frac{\tau_c}{1 + \omega_L^2 \tau_c^2} + \frac{4\tau_c}{1 + 4\omega_L^2 \tau_c^2}\right) \tag{21}$$

In the classical BPP theory, the constant K is defined for spin-1/2 nuclei as $K = \frac{3\mu_0^2}{160\pi^2}\frac{\hbar^2\gamma^4}{r^6}$, where μ_0 is the magnetic permeability of free space, $\hbar$ is the reduced Planck constant, γ is the gyromagnetic ratio of the nuclei, r is the distance

between the nuclei. In the case of quadrupolar nuclei, the constant K describes the strength of the coupling and the amplitude of the fluctuations of the quadrupolar interaction. It means that the relaxation rate depends on the relation between the Larmor frequency (which depends on the magnetic field) and the correlation time τ_c of the molecular motion. The correlation time depends on the activation energy of the motion E_a and temperature T as

$$\tau_c = \tau_0 e^{\frac{E_\mathrm{a}}{kT}} \tag{22}$$

where k is the Boltzmann constant and ${\tau_0}^{-1}$ is the attempt frequency. Relaxation is the fastest when $\tau_c \omega_L = \frac{1}{\sqrt{2}}$ (Fig. 17).

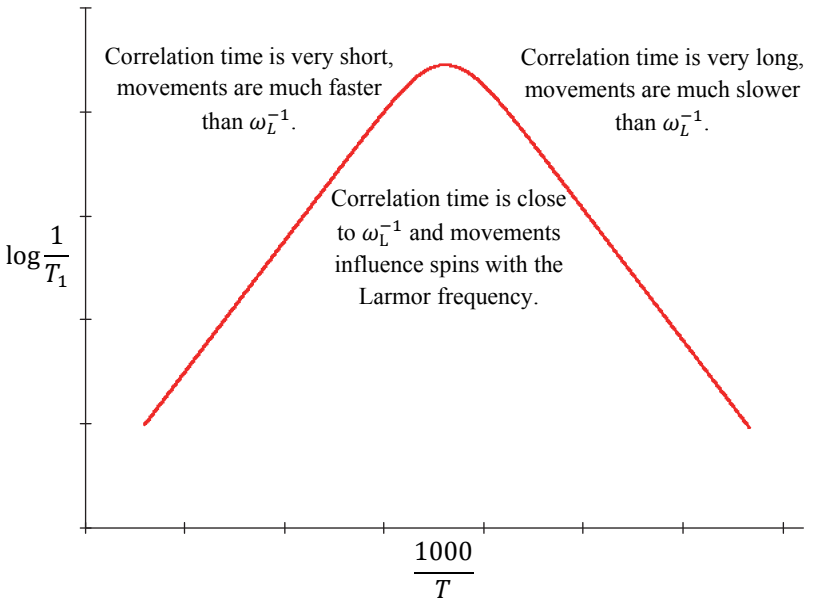

Figure 17. $1/T_1$ vs $1000/T$ plot shows how lattice movements affect the spin-lattice relaxation. Movements become faster and the correlation time decreases when the temperature T increases.

If the medium is not uniform, and the fluctuations do not take place between energetically equal configurations, then the system tends to spend less time in the higher energy states. As a result, there is a bias towards lower energy states. This situation can be modeled with oscillations in a double well with inequivalent minima (Fig. 18), and in this case, the BPP theory is applicable

with modifications (Blinc 1968). If the energies of the two different configurations are E_1 and E_2 and the difference between them $\Delta E = E_2 - E_1$, then the ratio of probabilities of occupancies of the configurations is

$$a = e^{-\Delta E/kT} \tag{23}$$

The spectral density of fluctuations in this case is

$$J(\omega) = F_0^2 \frac{2\tau_c}{1 + \omega^2\tau_c^2} \frac{4a}{(1+a)^2} \tag{24}$$

where the correlation time τ_c is the average time between the jumps or transitions, determined through the transition probabilities W_{12} and W_{21} between the two configurations:

$$\frac{1}{\tau_c} = W_{12} + W_{21} = (1+a)W_{12} \tag{25}$$

If the density of states in the different configurations is also different then the ratio of the densities of states in the different configurations a_0 has to be taken into account in the ratio of probabilities of occupancies of the configurations:

$$a = a_0 e^{-\Delta E/kT} \tag{26}$$

The influence of the modifications on the relaxation rate (transition probability per second) is shown in Figure 18, where the case of $\Delta E = 0$ and $a_0 = 1$ corresponds to the classical BPP model.

The ratio a adds other exponents into the relaxation rate equation, and as a result, the activation energy of the process is increased by ΔE, which means that the exact activation energy cannot be found from the slope of the Arrhenius plot if the value of ΔE is not known. Also, the maximum point of the relaxation rate is shifted, which means that the correlation time cannot be found directly from the maximum of the relaxation rate unless the parameter a is known.

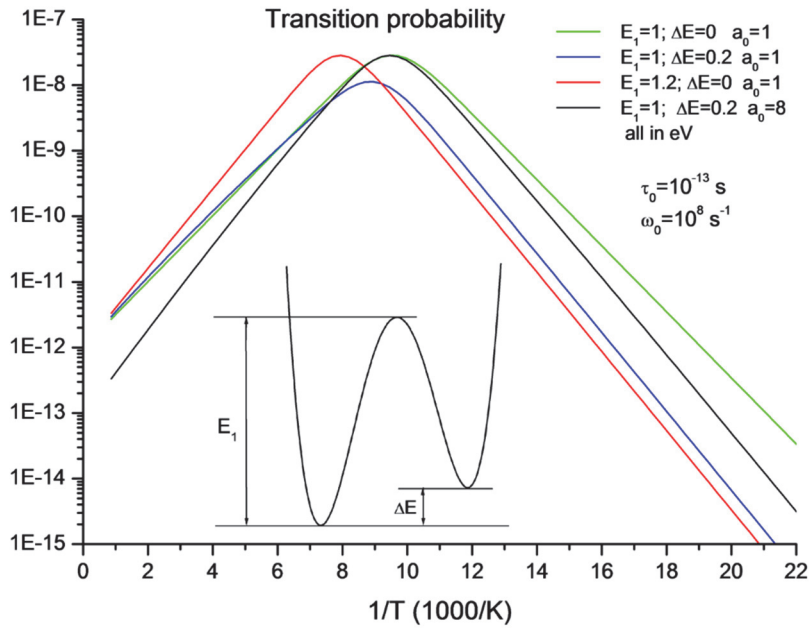

Figure 18. Influence of unequal energies of configurations where the fluctuations take place inbetween. The difference of energies ΔE changes the activation energy of the fluctuations to $E_a = E_1 + \Delta E$ instead of $E_a = E_1$, where E_1 is the height of the energy barrier between the configurations (compare the slopes of blue and red lines).

In some cases, e.g. at low temperatures, relaxation takes place due to thermal vibrations of the lattice. Relaxation is related to acoustical vibrations, which have relatively low frequency, and according to Abragam (Abragam 1961), direct and two-phonon processes causing relaxation can be distinguished, both in the frames of the Debye model. Direct process is the absorbtion or emission of a single phonon. Two-phonon process can be the absorbtion or emission of two phonons or the absorbtion of one and the emission of another phonon. The latter is called the Raman process.

If the frequency of one phonon in the two-phonon process is ω_1 and the frequency of another phonon is ω_2, then the first kind of the process must satisfy the condition $\omega_1 + \omega_2 = \omega_L$, and the Raman process, where one phonon is absorbed and another phonon emitted, must satisfy the condition $\omega_1 - \omega_2 = \omega_L$ in order to cause relaxation (ω_L is the Larmor frequency). In the direct process,

the frequency of the single phonon needs to be near ω_L. As phonon frequencies are mostly much higher than ω_L, only a small part of the phonon spectrum satisfies the conditions for the direct process and non-Raman two-phonon process, which makes the influence of these processes on the relaxation negligible. The Raman process, on the other hand, is efficient because phonons from all parts of the spectrum take part in it.

It is shown in detail in (Abragam 1961) that the relaxation rate P in the Raman process depends on the temperature T as $P = f(T^2)$ if the temperature is around the Debye temperature Θ of the material or higher, but if the temperature is considerably lower (0.02 Θ or less), then $P = f(T^7)$. Debye temperature is usually in the order of $10^2 – 10^3$ K.

On the other hand, the relaxation rate does not depend on the Larmor frequency and hence on the magnetic field if relaxation is caused by the Raman process because the condition $\omega_1 - \omega_2 = \omega_L$ is satisfied for a wide range of Larmor frequencies due to diversity of ω_1 and ω_2.

If the lattice is not uniform, and there are vibrations of a local extent around impurity centers which differ from lattice-wide vibrations, then the relaxation of the impurity nuclei depends on this characteristic local frequency. Relaxation rate is still independent of the magnetic field but varies exponentially with the temperature.

5.4.2. Experimental outcome

The temperature dependence of relaxation times of 7- and 8-coordinated scandium ions was measured in two different magnetic fields: 8.5 T and 4.7 T (Fig. 19).

It was revealed that there are processes dependent and independent on magnetic field, and at low and high temperatures there are different processes driving the relaxation. The low temperature processes do not depend on the magnetic field, as is apparent from the figure. Independence on the magnetic field is typical of phonon related relaxation (Raman process), and exponential temperature dependency refers to the local phonon relaxation mechanism. This is in accord with the fact that scandium ions are impurity centers in the ceria lattice, and their ionic radius is considerably smaller compared with cerium. The difference comes from the surround of the Sc ions in the lattice.

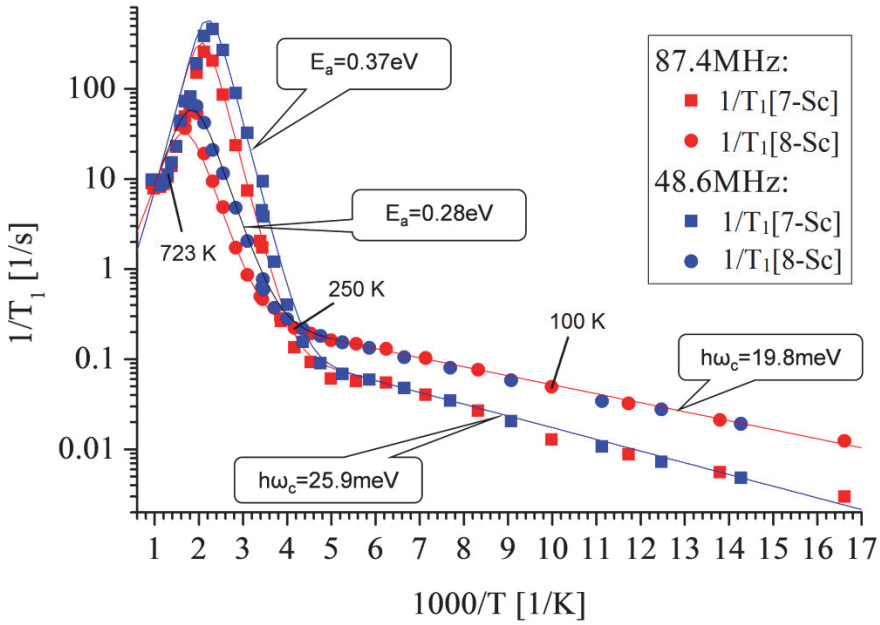

Figure 19. Longitudinal relaxation time temperature dependencies with magnetic fields of 4.7 T and 8.5 T.

The 7-coordinated Sc has a low symmetry environment but the 8-coordinated Sc has a symmetric cubic surround, and as the line shape analysis shows, the cubic symmetry remains at low temperatures too. The relaxation is expected to be caused by the movement of the Sc ion in the cubic box which is built for cerium, and is too large for a small Sc ion. The activation energy of the 8-coordinated Sc relaxation mechanism at low temperature is lower than that of the 7-coordinated Sc (0.0198 eV vs 0.0259 eV).

High temperature processes in the case of both 7- and 8-coordinated Sc have a temperature dependency typical of activated hopping: relaxation times become shorter and shorter when the hopping frequency approaches the Larmor frequency, and if the temperature continues rising, the hopping frequencies become higher than Larmor frequency, and the relaxation times become longer again as the spectral density of hopping frequency around the Larmor frequency decreases.

In the case of 7-coordinated Sc, the process is the vacancy hopping around the Sc ion, which according to the line shape analysis also began averaging the

powder line into a sharp peak around 250 K. The relaxation measurements allowed determination of the activation energy of that process: 0.37 eV.

The 8-coordinated Sc relaxation process, which has the activation energy of 0.28 eV, seems to be the fluctuation of the shape of the nest of the Sc ion. In the lowest energy configuration, the environment of the 8-coordinated Sc is cubic but there are metastable configurations with higher energies. It is important to mention that as explained above, the activation energy of the high temperature 8-coordinated Sc process is the sum of the energy barrier height between the configurations, and the energy difference of the configurations. As the exact configurations and their energies remain unknown in the frames of this study, the activation energy cannot be divided between the two parts, and it shows the maximum possible height of the energy barrier separating the two configurations (i.e. if the energy difference of configurations is zero, then the activation energy of the process is 0.28 eV).

5.5. Activation energy of the vacancy exchange in SDC [Publication 3]

2-dimensional NMR technique EXSY was used to determine the activation energy of the vacancy exchange process between 7- and 8-coordinated Sc ions in SDC. The crosspeaks in the EXSY spectrum appear due to the vacancy exchange, and the more frequent the exchange, the greater the crosspeaks are and the faster they grow. That means that the correlation times of the process can be found through the time dependence of the cross peak intensity growth (Fig. 20).

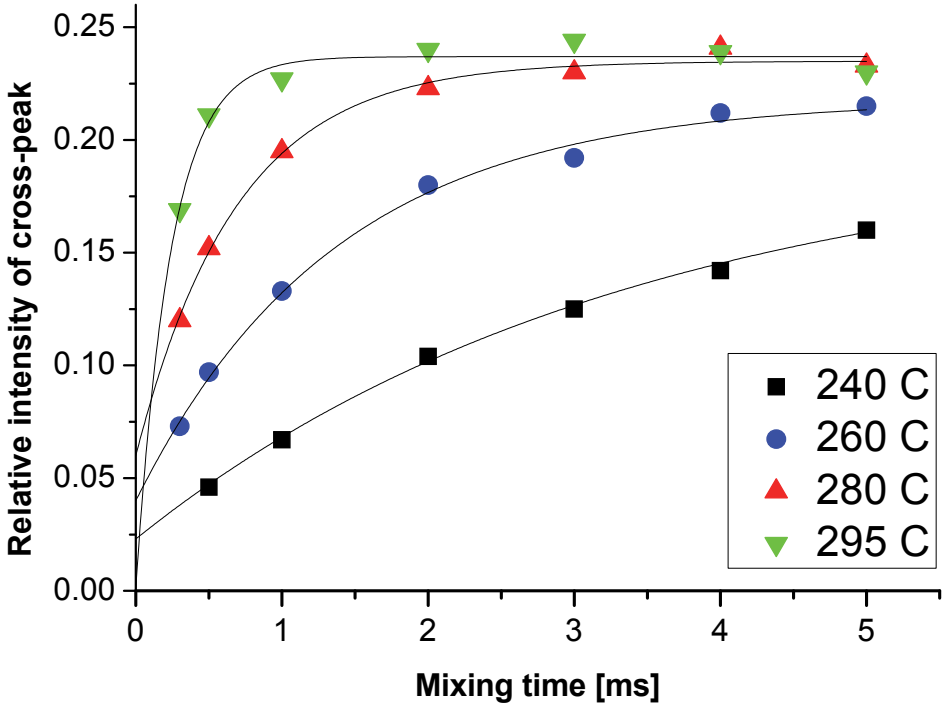

Figure 20. Cross peak growth at different temperatures.

The vacancy hopping frequency is the inverse of the correlation time, and through the hopping frequency, the exchange frequency can be found. The temperature dependence of the exchange frequency allows the activation energy of the exchange process to be found (Fig. 21). Just to compare and confirm the compliance of the data, the exchange rate corresponding to the averaging of two Sc spectrum lines into one at 633 K found from the Sc NMR spectra temperature dependence on Figure 15, is added to Figure 21. This exchange rate is not included in the fitting and finding of the activation energy.

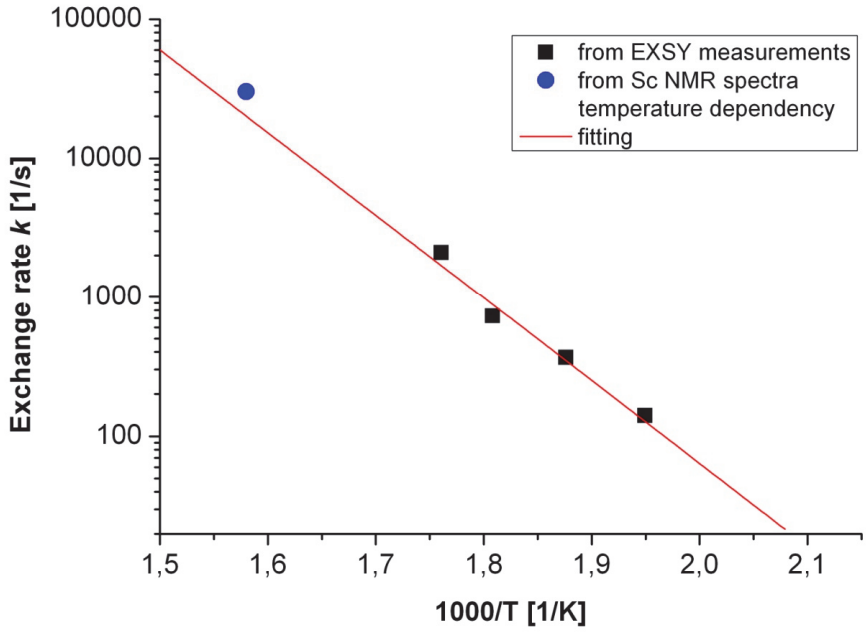

Figure 21. Vacancy exchange rates at different temperatures (an exchange rate corresponding to the averaging of two Sc spectrum lines into one is added for comparison as a blue dot).

The activation energy of the vacancy exchange in SDC was found to be 1.18 ± 0.1 eV. This is considerably higher than the activation energy needed for movement around the 7-coordinated Sc ion, and it is in good compliance with the values obtained in other studies (Sen *et al.* 2014). EXSY is a method allowing us to see the exchange "directly" and it is a very straightforward way to determine the exchange frequency and the activation energy of exchange.

5.6. Conclusions/Main results

1) The oxygen vacancy is always coupled with a Sc ion and moves around it. The activation energy of that movement is 0.37 eV, i.e. it takes place already at the room temperature.
2) The cubic oxygen-cage of the 8-coordinated Sc ion is stable and retains its symmetry at low and high temperatures but at high temperatures (around 250 K – 720 K), the cage structure fluctuates between the lowest energy cubic configuration and metastable higher energy configurations. Such structure fluctuations cause spin-lattice relaxation of the 8-coordinated Sc in the temperature range where they occur. Maximum height of the energy barrier between the configurations is 0.28 eV.
3) At low temperatures (under 200 K), the vacancy movement around 7-coordinated Sc and the structure fluctuations in the neighborhood of 8-coordinated Sc stop. Phonons dominate at low temperature in the lattice, and due to ion size mismatch there are local modes around Sc ions. The activation energies of fluctuations around the 7-coordinated and 8-coordinated Sc are 0.0259 eV and 0.0198 eV, respectively.
4) The vacancy exchange between 7- and 8-coordinated Sc ions starts at around 500 K, the activation energy of the exchange process is 1.18 eV. The time spent by vacancies in the lattice is negligible, the ratio of 7- and 8-coordinated Sc is retained.
5) The association energy of oxygen vacancy to the scandium ion in SDC is 1.18 eV – 0.47 eV = 0.71 eV.
6) With combustion synthesis, the Sc solubility in ceria is limited to 2%, and the exceeding of this limit can be clearly determined with NMR.

REFERENCES

A. Abragam, The principles of nuclear magnetism, Oxford University Press, London, 1961

S.B. Adler, J.W. Smith, J.A. Reimer, J. Chem. Phys. 98 (1993) 7613

M.D. Alba, P. Chain, P. Florian and D. Massiot, J. Phys. Chem. C 114 (2010) 12125

D.A. Andersson, S.I. Simak, N.V. Skorodumova, I.A. Abrikosov, B. Johansson, PNAS 2006, 103, 10, 3518-3521

M. Ando, I. Oikawa, Y. Noda, S. Ohki, M. Tansho, T. Shimizu, H. Kiyono, H. Maekawa, Solid State Ionics 192 (2011) 576

M. Ando, I. Oikawa, S. Ohki, M. Tansho, T. Shimizu, H. Maekawa, H. Kiyono, Chem. Lett. 42 (2013) 57

E.R. Andrew and D. P. Tunstall, Proc. Phys. Soc. 78 (1961) 1

H.J. Avila-Paredes, P. Jain, S. Sen, and S. Kim, Chem. Mater. 22 (2010) 893

S.P.S. Badwal, F.T. Ciacci and D. Milosevic, Solid State Ionics, 136-137 (2000) 91

R. Blinc, Adv. Magnetic Resonance 3 (1968) 141

N. Bloembergen, E.M. Purcell, R.V. Pound, Physical Review 73 (1948) 7, 679-712

T.E. Bull, S. Forsen D.L. Turner, J. Chem. Phys. 70 (1979) 3106

V. Butler, C.R.A. Catlow, B.E.F. Fender, J.H. Harding, Solid State Ionics 8 (1983) 109

Y.M. Chiang, D.P. Birnie III, W.D. Kingery, Physical Ceramics - Principles for Ceramic Science and Engineering, Wiley 1997

B.F. Chmelka, K.T. Mueller, A. Pines, J. Stebbins, Y. Wu, J.W. Zwanziger, Oxygen-17 NMR in Solids by Dynamic Angle Spinning and Double Rotation, Nature 339 (1989) 42-43

A.N. Cormack, C. R. A. Catlow and A. S. Nowick, J. Phys. Chem. Solid. 50. (1989) 177

T. Dahm, K. Ueda, Phys. Rev. Lett. 99 (2007) 187003

L.J.M. Davis, I. Heinmaa, G.R. Goward, Chem. Mater. 22 (2010) 769

H. Deguchia, H. Yoshida, T. Inagakia and M. Horiuchi, Solid State Ionics 176 (2005) 1817

P.P. Dholabhai, J.B. Adams, P. Crozier, R. Sharma, Phys. Chem. Chem. Phys. 12 (2010) 7904

P.P. Dholabhai, J.B. Adams, P. Crozier, R. Sharma, J. Chem. Phys. 132 (2010) 094104

P.P. Dholabhai, J.B. Adams, J. Mater. Sci. (2012) 47, 7530-7541

R.R. Ernst, G. Bodenhausen, A. Wokaun, Principles of Nuclear Magnetic Resonance in One and Two Dimensions, Oxford Science Publications 1997

J. Faber, G.C. Roux, A. Sylvestre, P. Abélard, Appl. Phys. A 49 (1989) 225

J.W. Fergus, J. Power Sources 162 (2006) 30

D.R. Figueroa, A. V. Chadwick, J. H. Strange, J. Phys. C: Solid State Phys. 11 (1978) 55

L. Frydman, J.S. Harwood, 'Isotropic Spectra of Halfinteger Quadrupole Spins from Bidimensional Magicangle Spinning NMR', J. Am. Chem. Soc., 117, 5367–5368 (1995)

K. Fuda, K. Kishio, S. Yamauchi, K. Fueki, J. Phys. Chem. Solids 4 (1984) 1253–1257

K. Fuda, K. Kishioa, S. Yamauchia, K. Fuekia, J. Phys. Chem. Solids 46 (1985) 1141

R. Gerhardt, W. -K. Lee and A. S. Nowick, J. Phys. Chem. Solids, 48 (1987) 563

R. Gerhardt-Anderson, A.S. Nowick, Solid State Ionics 5 (1981) 547

J. Gomes, O.A. Serra, J. Mater. Sci. 43 (2008) 546

M.I. Gordon M. J. R. Hoch, J. Phys. C: Solid State Phys. 11 (1978) 783

R.J. Gorte, AIChE Journal 56 (2010) 1126

H. Hayashia, R. Sagawaa, H. Inabaa, K. Kawamurab, Solid State Ionics 131 (2000) 281

I. Heinmaa, T. Joon, H. Kooskora, J. Subbi, Solid State Ionics 181 (2010) 1309

P. Heitjans, S. Indris, J. Phys.: Condens. Matter 15 (2003) R1257

J.V. Herle, T. Horita, T. Kawada, N. Sakai, H. Yokokawa and M. Dokiya, J. Am. Ceramic Soc. 80 (1997) 933

P.S. Hubbard, J. Chem. Phys. 53 (1970) 985

J. Hugo, P. Avila-Paredes, S. Jain, S. Sen, S. Kim, Chem. Mater. 22 (2010) 893

H. Inaba, H. Tagawa, Solid State Ionics 83 (1996) 1

A. Ismail, J. Hooper, J.B. Giorgi, T.K. Woo, Phys. Chem. Chem. Phys. 13 (2011) 6116–6124

P. Jain, Hugo J. Avila-Paredes, C. Gapuz, S. Sen, and S. Kim, J. Phys. Chem. C113 (2009) 6553

J. Jeener, B.H. Meier, P. Bachmann, R.R. Ernst, J. Chem. Phys. 71 (1979) 4546

J.A. Kilner, Solid State Ionics 129 (2000) 13

N.J. Kim, J. F. Stebbins, Chem. Mater. 19 (2007) 5742

S. Kim, P. Jain, Hugo J. Avila-Paredes, A. Thron, K. van Benthem, S. Sen, J. Mater. Chem. 20 (2010) 3855

O. Knop, E.M. Palmer, R.W. Robinson, Acta Crystallogr., A 31 (1975) 19-31

J.Van Kranendonk, Physica 20 (1954) 781

P. Li, I. Chen, J. E. Penner-Hahn and T. Tien, J. Am. Ceram. Soc. 74 (1991) 950

A. Llor, J. Virlet, Towards high-resolution NMR of more nuclei in solids: Sample spinning with time-dependent spinner axis angle, Chem. Phys. Lett. 152 (1988) 248-253

H. Maekawa, K. Kawata, Y. Xiong, N. Sakai, H. Yokokawa, Solid State Ionics 180 (2009) 314

L. Malavasi, C.A.J. Fisher, S.M. Islam, Chem. Soc. Rev. 39 (2010) 4370

L. Minervini, M. O. Zacate, R. W. Grimes, Solid State Ionics 116 (1999) 339

M. Mogensen, D. Lybye, N. Bonanos, P.V. Hendriksen and F.W. Poulsen, Solid State Ionics 174 (2004) 279

M. Mogensen, N.M. Sames, G.A. Topsett, Solid State Ionics 129 (2000) 65

R. Moos, N. Izu, F. Rettig, S. Reiß, W. Shin, I. Matsubara, Sensors 11 (2011) 3439

Y. Nakai, K. Ishida, H. Sugawara, D. Kikuchi and H. Sato, Phys. Rev. B77 (2008) 041101

M. Nakayama, M. Martin, Phys. Chem. Chem. Phys. 11 (2009) 3241–3249

W.M. O'Neill, M.A. Morris, Chem. Phys. Lett. 305 (1999) 389

C.L. Perrin, T.J. Dwyer, Chem. Rev. 1990, 90, 935-967

J. Reuben and Z. Luz, J. Phys. Chem. 80 (1976) 1357

I. Riess, J. Electrochem. Soc. 128 (1981), 2077-2081

R.A. Rocha, E.N.S. Mucillo, Materials Research Bulletin 38 (2003) 1979-1986

A. Samoson, E. Lippmaa, A. Pines, 'High Resolution Solid State NMR Averaging of Second-order Effects by Means of a Double-rotor', Mol. Phys., 65, 1013–1018 (1988)

S. Sen, Hugo J. Avila-Paredes and S. Kim, J. Mater. Chem. 18 (2008) 3915

S. Sen, T. Edwards, S.K. Kim, S. Kim, Chem. Mater. 26 (2014) 1918

K. Singh, S.A. Acharya, S.S. Bhoga, Indian Journal of Engineering and Materials Sciences vol.13 (2006), 525-530

S.J. Skinner, J.A. Kilner, Materials Today 2003, 30

T.S. Stefanik, H.L. Tuller, J. Eur. Ceram. Soc. 21 (2001) 1967

J. Subbi, I. Heinmaa, R. Põder, H. Kooskora, Solid State Ionics 225 (2012) 488

J. Subbi, I. Heinmaa, R. Põder, H. Kooskora, Solid State Ionics 239 (2013) 15

T. Taniguchi, Y. Sonoda, M. Echikawa, Y. Watanabe, K. Hatakeyama, S. Ida, M. Koinuma and Y. Matsumoto, ACS Appl. Mater. Interfaces 4 (2012) 1010

A. Trovarelli, C. de Leitenburg, M. Boaro, G. Dolcetti, Catal. Today 50 (1999) 353

D.Y. Wang, D.S. Park, J. Griffith, A.S. Nowick, Solid State Ionics 2 (1981) 95

H. Wang, A. Chroneos, U. Schwingenschlögl, J. Chem. Phys. 138 (2013) 224705

V.W.J. Verhoeven, I.M. de Shepper, G. Nachtegaal, A.P.M. Kentgens, E.M. Kelder, J. Schoonman, F.M. Mulder, Phys. Rev. Lett. 86 (2001) 4314

T. Viefhaus, T. Bolse, K. Müller, Solid State Ionics 177 (2006) 3063

L. Vivier, D. Duprez, ChemSusChem 3 (2010) 654

S. Yamazaki, T. Matsui, T. Ohashi and Y. Arita, Solid State Ionics 136–137 (2000) 913

M. Yashima, M. Kakihana and M. Yoshimura, Solid State Ionics 86-88 (1996) 1131

ACKNOWLEDGMENTS

Hereby I would like to thank my supervisors for working with me, and all my colleagues who have helped me in my studies. In our rather small institute, all people and their works are closely connected, and many colleagues from my department have contributed to this thesis in a rather direct manner, e.g. by providing liquid helium, constructing hardware for experiments, or melted glass for ampulas. I appreciate all that help. I am grateful to the university personnel for their help and advice with official paperwork and all the organizational tasks, allowing me to focus always on my thesis. Special thanks go to the Archimedes Foundation for funding my practical training in the Fraunhofer Institute for Ceramic Technologies and Systems in Germany.

ABSTRACT

The atomic level structure and oxygen vacancy dynamics in Sc doped ceria were studied in this research. Sc doped ceria probes with different doping levels were synthesized with the combustion synthesis method, and through the NMR measurements of the probes it was estimated that Sc solubility limit in ceria is 2%. A probe with the doping level of 0.5% was used in the study. Through the NMR line shape analysis and spectrum temperature dependency it was found that oxygen vacancy is strongly bound to the first coordination sphere of Sc ion, but it can move in that coordination sphere already at room temperature. At around 500 K, vacancy exchange between Sc ions starts. Temperature dependency of Sc spin-lattice relaxation time in two different magnetic fields revealed different lattice processes taking place at different temperatures in ceria. At low temperatures, the phonon mechanism drives the spin-lattice relaxation. At high temperature, vacancy movement (for 7-coordinated Sc) and lattice structure changes (around 8-coordinated Sc) cause the relaxation. The aim was to find the activation energy of vacancy movement in the first coordination sphere around Sc, and the activation energy of the vacancy exchange between Sc ions in the lattice. According to the measured relaxation temperature dependence, the former was 0.37 eV. Through EXSY measurements the activation energy of the vacancy exchange between Sc ions was found to be 1.18 eV. With these values, this study provides experimental data that are scarce for low-conducting SDC, and through that it enhances the understanding of doped ceria based ionic conductors. It also provides experiment-based starting points for simulations and computational studies.

KOKKUVÕTE

Töös uuriti Sc-lisandiga tseeriumdioksiidi atomaarset struktuuri ja hapniku vakantsi dünaamikat. Leeksünteesiga valmistati erineva legeerimisastmega Sc-lisandiga CeO_2 proovid ja tuumamagnetresonantsmõõtmistega (TMR) hinnati Sc lahustuvuse piiriks tseeriumdioksiidis 2%. Uuringutes kasutati 0.5% legeerimisastmega proovi. TMR spektrijoone kuju analüüsi ja spektrite temperatuurisõltuvuse kaudu tehti kindlaks, et hapniku vakants on tugevalt seotud skandiumi lähiümbrusse, aga saab skandiumi ümber liikuda juba toatemperatuuril. 500 K ümbruses hakkavad vakantsid liikuma läbi CeO_2 võre Sc ioonide vahel. Kahes erinevas magnetväljas mõõdetud Sc spinn-võre relaksatsiooni temperatuurisõltuvus näitas erinevaid protsesse, mis legeeritud CeO_2 võres eri temperatuuridel aset leiavad. Madalal temperatuuril põhjustab relaksatsiooni foononmehhanism. Kõrgel temperatuuril on relaksatsioonimehhanismiks vakantsi liikumine (7-koordineeritud Sc puhul) ja võre struktuurimuutused (8-koordineeritud Sc ümber). Eesmärk oli leida hapniku vakantsi liikumise aktivatsioonienergia Sc ümber ja vakantsi liikumise aktivatsioonienergia läbi võre erinevate Sc ioonide vahel. Esimene oli mõõdetud relaksatsiooni temperatuurisõltuvuse järgi 0.37 eV. 2D TMR mõõtmistega leiti vakantsi võres liikumse aktivatsioonienergia väärtuseks 1.18 eV. Nende tulemustega pakub töö uusi eksperimentaalseid andmeid Sc-lisandiga CeO_2 kohta, mida on selle madala ioonjuhtivusega materjali kohta vähe. Seeläbi parandab see töö arusaamist legeeritud CeO_2 põhistest ioonjuhtidest ja ühtlasi pakub katsepõhiseid lähteandmeid simulatsioonidele ja arvutuslikele töödele.

CURRICULUM VITAE

Name:	Reio Põder
Date of birth:	19.02.1985
Employment:	2004-2006 Tallinn University of Technology, Institute of Cybernetics, technician
	2007- National Institute of Chemical Physics and Biophysics, engineer
Education:	2004 German Gymnasium of Kadriorg
	2007 University of Tartu (BSc in physics)
	2009 Tallinn University of Technology (MSc in engineering physics)
	2009- Tallinn University of Technology, PhD studies (in engineering physics)
	2011 practical training in the Fraunhofer Institute for Ceramic Technologies and Systems, Germany
Speciality:	Solid oxide fuel cells and related materials

ELULOOKIRJELDUS

Nimi:	Reio Põder
Sünniaeg:	19.02.1985
Teenistuskäik:	2004-2006 TTÜ Küberneetika Instituut, tehnik
	2007- Keemilise ja Bioloogilise Füüsika Instituut, insener
Haridus:	2004 Kadrioru Saksa Gümnaasium
	2007 Tartu Ülikool (BSc füüsika erialal)
	2009 Tallinna Tehnikaülikool (MSc tehnilise füüsika erialal)
	2009- Tallinna Tehnikaülikool, doktoriõpe (tehnilise füüsika erialal)
	2011 praktika Fraunhoferi Keraamikatehnoloogiate ja -süsteemide Instituudis Saksamaal
Uurimis- ja arendustöö põhisuunad:	Tahke oksiidi kütuseelemendid ja nendega seotud materjalid

APPENDIX

PUBLICATION 1

J. Subbi, I. Heinmaa, R. Põder, H. Kooskora, *Solid state NMR investigation of oxygen dynamics in scandium doped ceria in 50 K to 1073 K temperature range*, Solid State Ionics 225 (2012) 488-492.

Solid State Ionics 225 (2012) 488–492

Contents lists available at SciVerse ScienceDirect

Solid State Ionics

journal homepage: www.elsevier.com/locate/ssi

Solid state NMR investigation of oxygen dynamics in scandium doped ceria in 50 K to 1073 K temperature range

Juhan Subbi *, Ivo Heinmaa, Reio Põder, Helgi Kooskora

National Institute of Chemical Physics and Biophysics, 23 Akadeemia tee, Tallinn 12618, Estonia

ARTICLE INFO

Article history:
Received 6 September 2011
Received in revised form 27 January 2012
Accepted 21 February 2012
Available online 13 March 2012

Keywords:
Ceria
Scandium
Oxygen dynamics
Solid state ^{45}Sc NMR

ABSTRACT

In this work we investigate the solubility of scandium in ceria, and present a detailed investigation of oxygen dynamics in 0.5% scandium doped ceria from 50 K to 1073 K by ^{45}Sc solid state NMR line shape, chemical shift, and spin-lattice relaxation analysis. We show that oxygen vacancy is strongly attached to the scandium in the seven-coordinated scandium–oxygen vacancy complex (7-Sc), but even at room temperature the vacancy is moving freely around the scandium atom between eight equivalent sites in millisecond time scale. The activation energy of that vacancy jump is 0.37 eV. The eight-coordinated (8-Sc) scandium ion retains cubic environment down to 50 K. The exchange rate between 7-Sc and 8-Sc sites exceeds 10^3 Hz above $T > 600$ K.

1. Introduction

Cerium oxide has found use in diverse technological applications from synthesis catalyst and automotive three-way catalyst to solid oxide fuel cells and possibly fluorescent screens. For most applications, cerium oxide is doped with different ions that enhance ionic conductivity, improve catalytic properties or supply necessary fluorescent centers.

Ionic conductivity in cerium oxide operates through diffusion of oxygen vacancies created by doping with aliovalent nuclei. Optimization of ionic conductivity in ceria is commonly approached by choosing dopants that keep the lattice constant close to the undoped value, e.g. Gd, Sm (minimal stress), and in the concentration range 10–20 at.%. At higher dopant concentrations the ion conductivity decreases, generally believed due to defect interactions [1,2]. Other, bigger and smaller dopants give lower ionic conductivity attributed to stronger deformation of the local structure and, consequently, to the higher barriers for ion hopping.

There is a considerable amount of theoretical modeling work done in this direction [3–5]. However, detailed experimental information about dopant distribution and interaction with vacancies has been hard to obtain. Gerhardt et al. [6] investigated scandium doped ceria with dielectric relaxation methods, and found several relaxation processes in low temperature region. Later EXAFS methods were applied to doped ceria [7,8] to determine defect association, however, uncertainties in this method are still large.

Solid state NMR provides a powerful and unique tool for investigating both dopant and vacancy distributions and dynamics. Cerium oxide has fluorite structure with cubic symmetry, hence both cations and anions have cubic neighborhoods in pure ceria. This eliminates quadrupolar coupling, and both dipolar and quadrupolar nuclei have comparatively narrow lines, if introduced to the lattice in low concentrations. However, for high resolution NMR we need dopants without unpaired electrons to avoid inhomogeneous magnetic field due to electronic magnetism. This leaves us with four trivalent candidates: La, Lu, Y and Sc. NMR spectra of ^{139}La, ^{89}Y and ^{45}Sc in doped ceria have been measured before [9–11]. ^{17}O-NMR has been used as well, but generally isotopic enrichment is needed due to low natural abundance of ^{17}O.

In the paper by Avila-Peres et al., [11] it was shown that around 400 °C oxygen vacancies become mobile in NMR timescales, and this averages Sc sites chemical shifts into a single line, known as motional averaging. It was shown, that in particular cases there are immobile vacancies in Sc doped ceria. We discuss this later.

Scandium is the smallest of these ions, and its solubility in ceria is limited due to size mismatch [12]. Due to small ion radius, 0.87 A for Sc^{3+}, compared to 0.97 A for Ce^{4+}, scandium ion neighborhood and dynamics are expected to be different from those of cerium. It is expected to bind vacancy stronger than bigger dopant ions, and provide lower ion conductivity [1,3].

On the other hand, scandium doped zirconium oxide is a better ion conductor than yttrium doped zirconium oxide, despite Sc^{3+} being too small for stable fluorite structure, and has very complicated phase diagram [13]. This observation contradicts the common view that the least lattice deforming dopants provide the best ion conductivity [14]. In this work we provide one possible explanation to this, showing that for a vacancy hopping between eight equivalent sites

* Corresponding author. Tel.: +372 56687370.
E-mail address: subbi@kbfi.ee (J. Subbi).

0167-2738/$ – see front matter © 2012 Elsevier B.V. All rights reserved.
doi:10.1016/j.ssi.2012.02.039

around scandium ion, the barrier is significantly lower than for vacancy escape from the parent ion. If enough scandium could be introduced into the lattice, scandium neighborhoods may form percolating paths throughout the whole lattice.

Scandium is a good NMR nucleus with high sensitivity and limited quadrupole coupling that has been widely investigated in solid state NMR [15]. It is giving two resonance lines in the NMR spectrum of Sc doped ceria: an eight-coordinated scandium (8-Sc) and a seven-coordinated scandium–oxygen vacancy complex (7-Sc) [11].

In this work we present a detailed investigation of oxygen dynamics in scandium doped ceria from 50 K to 1073 K by solid state NMR relaxation, chemical shift and line shape analysis. We show that oxygen vacancy is strongly attached to the scandium in the seven-coordinated scandium–oxygen vacancy complex, but even at room temperature the vacancy is moving freely around scandium atom between eight equivalent sites in a millisecond time scale.

2. Experimental

Scandium doped ceria $Sc_xCe_{1-x}O_{2-x/2}$ with $x = 0.002$, 0.005, 0.01 and 0.05 were synthesized by citrate route from corresponding nitrates [16,17] (in the following we use notation 0.2%SDC, 0.5%SDC, 1%SDC and 5%SDC). Appropriate amounts of $LaNO_3$ and $CeNO_3$ aqueous solutions were added to neutralized oxalic acid solution. After precipitation the product was washed, dried and subsequently heated to 500 °C. For temperature dependent measurements the powders were isostatically pressed into 5 mm rods with length of 20 mm, and sintered at 1600 °C for 3 h. Part of the powder was calcined at 1600 °C without pressing for MAS NMR analysis. A portion of 5%SDC was calcined at 1400 °C to test the solubility.

^{45}Sc MAS NMR spectra were recorded on Bruker AVANCE-II-600 spectrometer, in 14.5 T magnetic field (^{45}Sc resonance frequency 145.8 MHz) using home built MAS probe and 4 mm zirconia rotors. The spectra were referenced to the resonance frequency of $Sc(NO_3)_3$ solution in water. Different spinning speeds were used, but already 7 kHz was adequate for suppressing dipolar broadening.

Temperature dependencies of ^{45}Sc spin-lattice relaxation of the static SDC samples were measured at two magnetic fields 8.5 T and 4.7 T using saturation recovery pulse sequence. These measurements were carried out on Bruker spectrometer AMX 360 using home built high-temperature probe. The probe has NMR coil in appropriate oven for samples in 5 mm quartz ampulas. Due to good thermal insulation the temperatures up to 800 °C were obtained within 15 W heating power. The low temperature measurements were carried out using home built probe in He gas flow cryostat from Janis Research Company.

3. Results and discussion

3.1. ^{45}Sc MAS NMR spectra and Sc solubility in ceria

In this work we are interested in properties of separated scandium centres, so the scandium solubility in ceria and possible defect association had to be investigated first. ^{45}Sc MAS NMR spectra of 0.2%SDC, 1%SDC and 5%SDC powders and that of a commercial Sc_2O_3 sample are presented in Fig. 1. Only two narrow lines in SDC, corresponding to isolated 7-Sc, and 8-Sc centres at 36 ppm and −21 ppm, respectively, are visible in the spectra of 0.2%SDC and 1%SDC. In 5%SDC the situation has changed. We can see clearly both undissolved Sc_2O_3 (similar Sc_2O_3 band can be seen in 5%SDC spectra of Jain et al. [18] as well) and Sc–Sc associates that form a shoulder to the 7-coordinated line. The small intensity of Sc_2O_3 resonances can be deceiving as this represent only central transitions of the quadrupole broadened spectra. So 5%SDC was under our preparation conditions clearly above the simple solubility limit. Increasing calcination temperature from 1400 °C to 1600 °C increased the shoulder at 7-Sc line, but did not add free scandium centres to the lattice.

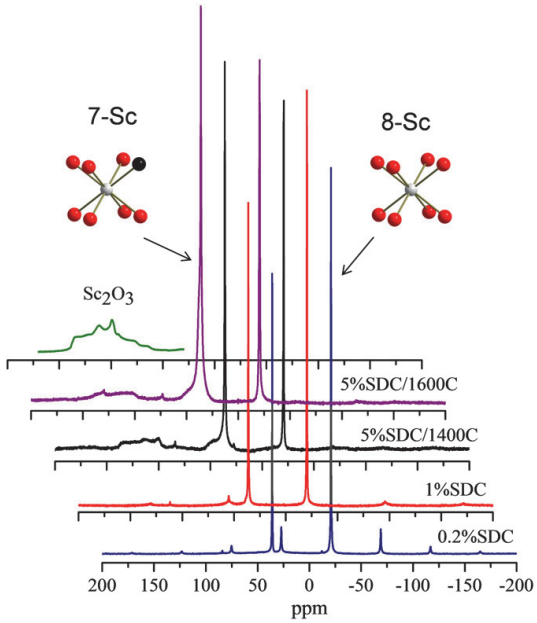

Fig. 1. ^{45}Sc MAS NMR spectra of 0.2%SDC, 1%SDC, 5%SDC and scandium oxide powders in 14.5 T magnetic field, at room temperature. All small lines are rotational sidebands.

The solubility of scandium in ceria is a complicated problem. If there would be just randomly distributed scandium in ceria and precipitated Sc_2O_3, there would be a simple solubility limit. However, if there is a strong energetic benefit from forming scandium dimer–oxygen vacancy complexes, and dissolving these in ceria, the analysis gets more complicated. Higher multimers can be involved as well, but dimers are probably the first to form. The scandium in these dimer–vacancy complexes is 7-coordinated, as the lowest energy position for the vacancy is between scandium ions, and corresponding lines are close to 7-coordinated single scandium line. But these complexes have lower than cubic symmetry, and this shows in quadrupole broadening of scandium lines. Higher scandium complexes are not necessarily 7-coordinated, and as the complexes get bigger, scandium coordination eventually approaches effective 6 of scandium oxide. The almost linear chemical shift dependence on coordination can be seen in Fig. 1. The Vergaard slope analysis of XRD line shifts, used routinely for solubility tests, however, does not necessarily separate dissolved monomers from dimers, and shows only macroscopic phase separation. Equilibrium structures in the scandia–ceria system and their formation is an interesting problem in itself, and solid state NMR could be helpful here, but this remains outside the scope of this work.

Our goal here is to investigate separated scandium centres, and despite the fact that 3 h at 1600 °C may not be enough to achieve equilibrium distribution of scandium complexes in 5%SDC, some trends are clearly visible. While in 0.2%SDC, 0.5%SDC and 1%SDC there is a small but detectable amount of 7-coordinated scandium dimers or higher complexes, in 5%SDC we have separation of phases at 1400 °C. At 1600 °C the separated scandium oxide phase is still visible, and the additional dissolution of scandium oxide creates a strong wing to the 7-coordinated single scandium peak, without increasing the 8-coordinated scandium line intensity. This means that mainly neutral multiple-scandium–vacancy complexes are formed, and no ideal solution can be achieved. To avoid complications due to scandium dimers and higher complexes, we chose 0.5%SDC for the

detailed investigations. 0.2%SDC and 1%SDC spectra were measured to confirm the concentration independence of the spectral features we were investigating.

The ratio of 7-Sc and 8-Sc ions depends on scandium concentration, defect association and availability of additional centres capable to bind oxygen vacancies. In the lattice of ceria every cation has 12 nearest neighbour cations. Therefore, in 0.5%SDC, in the case of random distribution of scandium ions, 6% of scandium ions form dimers, and the spectra are dominated by single scandium ion lines. If the vacancies would be distributed randomly in the lattice, the intensity of the 7-Sc line would be about 2%. On the other hand, if there is significant attraction between scandium ions and vacancies, as suggested by earlier experiments [6,18] and calculations [3], we will see an equal amount of 7-Sc and 8-Sc and a small amount of neutral scandium dimer–vacancy pairs. This result is not altered, if the dimer concentration is somewhat higher than predicted from random distribution of scandium ions. Experimentally, the exact ratio of 7-Sc to 8-Sc was hard to determine from spectra, as the distribution of intensity between sidebands was different for these sites. While MAS spectra gave 7-Sc to 8-Sc ratio 47:53, static spectra gave the ratio 54:46. Overall, the simple model of strong attraction of vacancies to scandium ions works well, and we rely on it in this work.

A surprising feature in the MAS NMR spectra is the almost complete lack of rotational sidebands of 7-Sc–vacancy complex that should be of lower symmetry than 8-Sc. The explanation comes from low temperature measurements in the next section: the narrow 7-Sc line is a result of dynamical narrowing, at room temperature the vacancy is rapidly rotating around scandium ion, averaging out both quadrupolar and chemical shift anisotropies.

3.2. Vacancy dynamics at high temperature

All temperature dependent measurements were conducted in static samples. As the cation in the CeO_2 lattice has cubic symmetry, both chemical shift anisotropy and quadrupolar coupling are missing, if the lattice symmetry is retained around the dopant site. Remaining line broadening at room temperature is mainly due to inhomogeneous macroscopic magnetic susceptibility of the sample, and amounts to 3 ppm in our case.

^{45}Sc spectra from room temperature to 1073 K are presented in Fig. 2. At temperature around 500 K both lines started to broaden and at 633 K coalesced into one line in the middle, due to fast oxygen vacancy hopping between 7-Sc and 8-Sc scandium ions. The vacancy movement averages two lines into a single line, if the vacancy exchange frequency is higher than the line separation, $2\pi \times 4.8\ 10^3\ s^{-1}$ in our case. However, this process is not a simple hopping between two equivalent sites. Since the average distance between the Sc ions in 0.5%SDC is about 6 lattice units ($\sqrt[3]{200}$), many jumps are needed for a vacancy to find another scandium ion. It cannot be local hopping near the 7-Sc ion, as in this case 8-Sc would not be involved, and the 8-Sc line would be unmoved. According to a recent modelling study [3], the vacancy association energy to scandium is 0.4 eV negative, and the vacancy is essentially bound, spending most of the time in scandium neighbourhood, despite frequent hops into ceria lattice. Due to this potential well the barrier for leaving scandium ion neighborhood is higher than the barrier for hopping in the pure ceria lattice, and accordingly the frequency of hopping in pure lattice is high compared to the frequency of leaving the scandium neighbourhood. So the vacancy in pure lattice finds soon another scandium to stay with, and spectra on Fig. 2 show that all scandium ions are equivalent in this process: All visible intensity is in the averaged line, and its average coordination number is close to 7.5. At higher temperature the vacancy should spend more time in ceria lattice, the scandium–vacancy complex "dissociates", and average coordination number of scandium should diminish, if the temperature is high enough, see below.

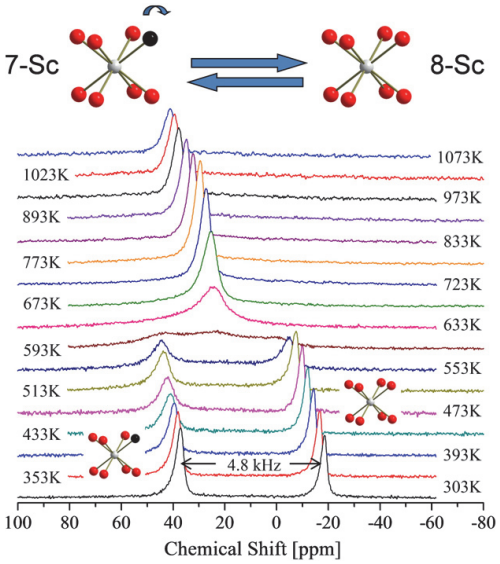

Fig. 2. High-temperature ^{45}Sc static powder NMR spectra of 0.5%SDC in 8.4 T magnetic field.

High-temperature averaging of scandium lines into one line has been reported recently by Avila-Peres et al. [11], where 5% scandium doped ceria was investigated. They saw immobile oxygen vacancies and interpreted their spectra by a simple double well jumping model. However, we have shown here that 5% of scandium oxide cannot be dissolved in ceria under standard preparation conditions, and indeed a scandium oxide band is clearly visible in their spectra [18]. Because of incomplete solvation of scandium, all kind of trapping sites for vacancies can be formed with different binding energies and temperatures of dissociation. We have shown here that in 0.5%SDC, where single scandium centres dominate, the vacancies associated with them are all mobile.

3.3. Vacancy dynamics at low temperature

^{45}Sc low temperature spectra are presented on Fig. 3. 7-Sc and 8-Sc lines have different temperature behaviours. Going down from room temperature, the 7-Sc line first broadened at 218 K and then obtained a characteristic powder line shape due to axially symmetrical chemical shift anisotropy at 188 K, with the full width of 2.3 kHz. We interpret this as a freezing of the vacancy rotation around the scandium ion, i.e. at temperature below $T<220$ K the vacancy hopping frequency becomes lower than 2.3 kHz. 8-Sc, on the other hand, retains narrow symmetrical line down to 50 K, pointing to high symmetry of the 8-Sc site.

There is surprisingly small quadrupolar coupling in 7-Sc even in this frozen state. From our experiments, quadrupolar broadening must be much smaller than chemical shift anisotropy broadening. The chemical shift anisotropy as the source of broadening is supported by the line shape and magnetic field independence of the broadening, tested in a lower field 4.7 T magnet. We do not know the reason for this.

3.4. Chemical shift temperature dependence and spin-lattice relaxation

An interesting parameter in the spectra is chemical shift temperature dependence, presented in Fig. 4. In the low temperature range, where 7-Sc and 8-Sc behave as individual centres, this characterizes temperature change of chemical shielding by local neighbourhood.

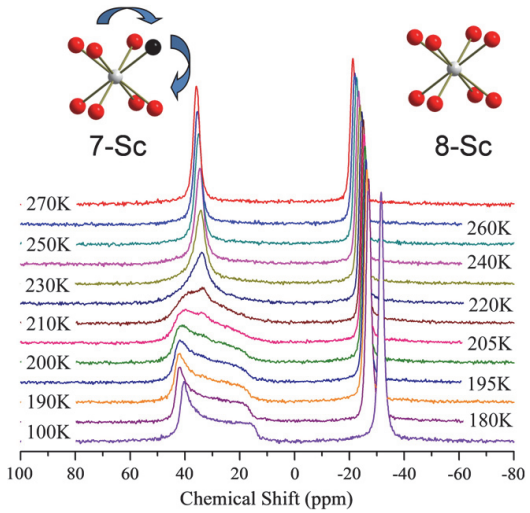

Fig. 3. Low temperature ^{45}Sc NMR spectra of 0.5%SDC in 8.4 T magnetic field. The 7-Sc line shape at 100 K corresponds to chemical shift anisotropy broadening with axially symmetric chemical shift tensor, $\delta_{\parallel} = 14$ ppm and $\delta_{\perp} = 42$ ppm.

The shielding is smaller for 7-Sc than for 8-Sc, and diminishes with thermal expansion of the lattice according to the change of local environment.

At high temperature, where the lines coalesce due to fast oxygen vacancy hopping, the chemical shift reflects the average environment of the scandium ion. It depends on the average coordination number of scandium ion and on the chemical shifts of both centres, 7-Sc and 8-Sc. Remarkably, in the low temperature range the temperature dependence of the chemical shift of 8-Sc is much stronger than that of 7-Sc. We believe this reflects soft, large amplitude motion of small scandium ion in a too big cage of 8-Sc. However, the 8-Sc neighbourhood remains cubic down to the lowest temperatures. Some doubts in this respect have been presented by Cormack et al. [19].

In the high-temperature range, where there is just one averaged NMR line, the chemical shift of that line reflects the fact that there are twice less vacancies than scandium ions. The temperature dependence of the chemical shift of the high-temperature line is also average between the extrapolations of low-T 7-Sc and 8-Sc shifts.

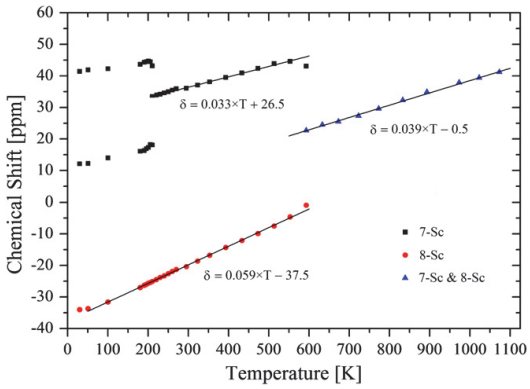

Fig. 4. Temperature dependence of the chemical shift δ of ^{45}Sc static powder NMR spectra of 0.5%SDC in 8.4 T magnetic field.

Its linearity shows that vacancies spend most of the time near scandium ions and there is no effective dissociation of scandium–vacancy complex up to 1073 K.

The spin-lattice relaxation behaviour of scandium ions has many features and its detailed analysis goes out of the scope of this publication. However, in the temperature range from 250 to 550 K the relaxation of Sc in 7-Sc site reflects activated rotation of the vacancy around scandium ion with activation energy 0.37 eV. The correlation time for vacancy hopping around scandium ion, calculated from spin-lattice relaxation, is 70 μs at 220 K and agrees well with observed freezing of rotational averaging at the same temperature.

The activation energy for vacancy hopping around scandium ion is much lower than activation energy for oxygen ion transport in any doped ceria. We believe this is due to the small size of scandium ion, therefore leaving more space around it and making the barrier for vacancy hopping lower, as less deformation is needed from the surrounding lattice to accomplish the jump. This is in accordance with the results of model calculations by Nakayama and Martin [3], showing the lowest activation energy for any doped ceria for jumps between cerium and scandium ions.

These results point to an interesting speculation: If we could introduce so much scandium into ceria lattice that scandium neighbourhoods would touch, we could have a very good ion conductor. Unfortunately, the ion size mismatch that lowers vacancy jumping barrier, also severely limits the scandium solubility in ceria. However, in scandium doped zirconia (SSZ) the small size of scandium ion can be the reason for high conductivity, despite of the fact that scandium ion is too small for stabilizing cubic structure in zirconia, resulting in an extremely complicated phase diagram, and causing problems with practical use due to unstable microstructure [20]. At 20% scandium doping, where the ion conductivity is the highest, scandium neighbourhoods are well connected in SSZ, and may form favourable ion transport channels.

In general, this indicates that for best oxygen conductivity we need stressed crystal structures with long metal–metal distances. Unfortunately, these systems may not have enough thermodynamic stability for practical applications.

4. Conclusions

Scandium solubility in ceria is limited, and 5% scandium is not dissolved in 3 h at 1600 °C. In dissolved part mainly scandium complexes are formed, and to investigate isolated scandium centres, doping should be preferably below 1%.

Oxygen vacancies are strongly attached to scandium ions and spend most of the time in the nearest neighbour position up to temperature T = 1073 K, despite jumps into ceria lattice with frequency, growing over 5 kHz above 600 K. In the same time they rotate freely around scandium ions even at room temperature, with low activation energy of 0.37 eV. The rotation frequency becomes lower than 2 kHz below T < 200 K.

8-Sc cage in ceria lattice has cubic equilibrium structure. However, the potential surface of the cage can be complicated with lower symmetry configurations with local potential minimums energetically close.

Acknowledgments

This study has been supported by the Estonian Science Foundation grant 8198, by grant SF0690034s09 from the Estonian Ministry of Education and by AS Elcogen.

References

[1] J. Faber, G.C. Roux, A. Sylvestre, P. Abélard, Appl. Phys. A 49 (1989) 225.
[2] M. Mogensen, N.M. Sammes, G.A. Topsett, Solid State Ionics 129 (2000) 65.
[3] M. Nakayama, M. Martin, Phys. Chem. Chem. Phys. 11 (2009) 3241.

[4] H. Hayashia, R. Sagawaa, H. Inabaa, K. Kawamurab, Solid State Ionics 131 (2000) 281.
[5] L. Minervini, M.O. Zacate, R.W. Grimes, Solid State Ionics 116 (1999) 339.
[6] R. Gerhardt, W.-K. Lee, A.S. Nowick, J. Phys. Chem. Solids 48 (1987) 563.
[7] S. Yamazaki, T. Matsui, T. Ohashi, Y. Arita, Solid State Ionics 136–137 (2000) 913.
[8] H. Deguchia, H. Yoshida, T. Inagakia, M. Horiuchi, Solid State Ionics 176 (2005) 1817.
[9] W.M. O'Neill, M.A. Morris, Chem. Phys. Lett. 305 (1999) 389.
[10] N. Kim, J. Stebbins, Chem. Mater. 19 (2007) 5742.
[11] H.J. Avila-Paredes, P. Jain, S. Sen, S. Kim, Chem. Mater. 22 (2010) 893.
[12] P. Li, I. Chen, J.E. Penner-Hahn, T. Tien, J. Am. Ceram. Soc. 74 (1991) 950.
[13] M. Yashima, M. Kakihana, M. Yoshimura, Solid State Ionics 86–88 (1996) 1131.
[14] M. Mogensen, D. Lybye, N. Bonanos, P.V. Hendriksen, F.W. Poulsen, Solid State Ionics 174 (2004) 279.
[15] M.D. Alba, P. Chain, P. Florian, D. Massiot, J. Phys. Chem. C 114 (2010) 12125.
[16] J.V. Herle, T. Horita, T. Kawada, N. Sakai, H. Yokokawa, M. Dokiya, J. Am. Ceram. Soc. 80 (1997) 933.
[17] I. Heinmaa, T. Joon, H. Kooskora, J. Pahapill, J. Subbi, Solid State Ionics 181 (2010) 1309.
[18] P. Jain, H.J. Avila-Paredes, C. Gapuz, S. Sen, S. Kim, J. Phys. Chem. C 113 (2009) 6553.
[19] A.N. Cormack, C.R.A. Catlow, A.S. Nowick, J. Phys. Chem. Solids 50 (1989) 177.
[20] S.P.S. Badwal, F.T. Ciacci, D. Milosevic, Solid State Ionics 136–137 (2000) 91.

PUBLICATION 2

J. Subbi, I. Heinmaa, R. Põder, H. Kooskora, *Solid state NMR spin-lattice relaxation investigation of oxygen dynamics in scandium doped ceria from 60 to 1073 K*, Solid State Ionics 239 (2013) 15-20.

Solid State Ionics 239 (2013) 15–20

Contents lists available at SciVerse ScienceDirect

Solid State Ionics

journal homepage: www.elsevier.com/locate/ssi

Solid state NMR spin-lattice relaxation investigation of oxygen dynamics in scandium doped ceria from 60 to 1073 K

Juhan Subbi *, Ivo Heinmaa, Reio Põder, Helgi Kooskora

National Institute of Chemical Physics and Biophysics, 23 Akadeemia tee, Tallinn 12618, Estonia

ARTICLE INFO

Article history:
Received 13 July 2012
Received in revised form 27 February 2013
Accepted 3 March 2013
Available online 9 April 2013

Keywords:
Ceria
Scandium
Oxygen dynamics
^{45}Sc NMR
Spin-lattice relaxation

ABSTRACT

Scandium spin dynamics in scandium doped ceria has been addressed first time through spin-lattice relaxation temperature dependence. Scandium spin-lattice relaxation temperature dependence in 0.5% scandium doped ceria matrix has been measured in the range between 60 K and 1073 K in magnetic fields 4.7 T and 8.5 T. The temperature dependence revealed four separate processes, two for 8-coordinated scandium and two for 7-coordinated scandium. However, none of these processes could be associated with oxygen vacancy hopping processes, directly responsible for ion conductivity in scandium doped ceria.

We have established that for 7-Sc, the high temperature process is vacancy hopping around the scandium ion with activation energy 0.37 eV and the low temperature process is a Raman process involving local vibrations with characteristic energy 26 meV (208 cm^{-1}).

For 8-Sc, the high temperature process is assigned to hopping between potential wells with different energy minima with apparent activation energy of 0.28 eV. We have shown that in this case the apparent activation energy of the process does not correspond to barrier height for hopping, but to barrier height plus energy difference between minima of corresponding wells. The low temperature process is again a Raman process involving local vibrations with even lower characteristic energy 20 meV (160 cm^{-1}).

1. Introduction

Cerium oxide has found use in diverse technological applications from synthesis catalyst [1] and automotive three-way catalyst [2,3] to solid oxide fuel cells and potentially fluorescent screens [4,5]. For most applications, cerium oxide is doped with different ions that enhance ion conductivity, improve catalytic properties or supply necessary fluorescent centers.

Ion conductivity in ceria operates through diffusion of oxygen vacancies created by doping with aliovalent nuclei. Optimization of ion conductivity in ceria is commonly approached by choosing dopants that keep the lattice constant close to the undoped value, e.g. Gd, Sm (minimal stress), and in the concentration range 10–20 at.%. At higher dopant concentrations the ion conductivity decreases, generally believed due to defect interactions [6,7]. Other bigger and smaller dopants give lower ion conductivity attributed to higher deformation of the local structure and consequent higher barriers for ion hopping.

Theoretical modeling of oxygen vacancy energetics in doped ceria lattice [8–10] provides us preferred configurations of dopants and vacancies, and also potential barriers for transfer of ions between different configurations. Experimental data about these barriers are generally obtained from measurements of the temperature dependence of ionic conductivity. Macroscopic conductivity is, however, an averaged property, and gives only indirect information about local ion hopping dynamics.

Solid state NMR provides here a powerful tool for investigating both dopant and vacancy distributions and dynamics in doped ceria. Both NMR lineshape analysis and spin-lattice relaxation measurements of oxygen ^{17}O [11–16] or doped nuclei such as ^{45}Sc [17–20] or ^{89}Y [21–23] can provide valuable information about ion movement and lattice dynamics in general. Spin-lattice relaxation of quadrupolar nuclei in the absence of electronic magnetism is dominated by coupling of nuclear quadrupole moment to electric field gradient (efg) fluctuations [24,25]. These fluctuations can be induced by thermal vibrations of the lattice or by changes of the lattice configuration near the nucleus, e.g. ion conduction related hopping. Temperature dependence of spin-lattice relaxation can reveal the activation barrier to the ion hopping and has been used widely to investigate ionic conduction in different compounds [11–13,26,27]. However, in most of the ionic conductors the NMR data yield much smaller activation energy than conductivity measurement (see review [26]), except in some cases, e. g. doped BaF_2 (fluorite structure), where the NMR relaxation and conductivity data are shown to be in good agreement [27]. It is argued that the activation energy from NMR is much lower because NMR relaxation is sensitive to local single ion hops, whereas the conductivity probes the long range transport where the highest barrier may determine the conductivity. But in simple structures like fluorite lattice, local jumps in the host lattice that would have significantly lower barrier than those responsible for

* Corresponding author. Tel.: +372 56687370.
E-mail address: subbi@kbfi.ee (J. Subbi).

0167-2738/$ – see front matter © 2013 Elsevier B.V. All rights reserved.
http://dx.doi.org/10.1016/j.ssi.2013.03.008

long range diffusion, are hard to imagine—there is just one sort of possible jumps in this high symmetry crystal. Situation can be different around dopants, as is demonstrated in this work and in our previous publication [20].

Spin-lattice relaxation of ^{17}O in oxygen conductors was investigated first by Fuda et al. in yttrium doped ceria [11,12], and later by Viefhaus et al. in yttrium stabilized zirconia (YSZ) [13]. Fuda et al. found two activated processes from two maxima. They assigned the relaxation maximum at $T = 600$ K to the mechanism of oxygen jumps via vacancies. The activation energy of the process was determined as $E_a = 0.49$ eV and, surprisingly, the jumping rate $1/\tau_c$ was found to be independent of dopant concentration. This activation energy is considerably smaller than activation energy of ionic conduction, 0.88 eV [6]. For YSZ the difference between the activation energy from conductivity measurements and that from the NMR relaxation is even larger. Reported activation energy values for YSZ from conductivity measurements are between 1.17 and 1.33 eV [28], about four times higher than the value ~0.3 eV from NMR relaxation found by Viefhaus et al. [13].

Recently our group has measured ^{17}O relaxation in lanthanum doped ceria at different lanthanum doping levels, and found two activated relaxation processes. Only one, giving relaxation maximum at 1070 K, and activation energy of 0.96 eV was obtained for oxygen vacancy jumps between available oxygen sites. The other, with relaxation maximum at 650 K, and activation energy of 0.45 eV had too short correlation time, and was interpreted as due to ceria lattice dynamics [15].

There are other methods to study molecular dynamics in crystals as well. Some time ago Gerhardt et al. [29] investigated scandium doped ceria with dielectric and acoustic relaxation methods, and found several relaxation processes in low temperature region. A comparison with our results will be presented in discussion.

What are then the activated processes in ionic conductors we see in spin-lattice relaxation, and how are they connected to the ionic conduction mechanism? These are the questions motivating us, and in this work we investigate relaxation processes in weakly scandium doped ceria, allowing investigation of isolated scandium centers.

Cerium oxide has fluorite structure with cubic symmetry, and both, cations and anions have cubic neighborhoods in pure ceria. This eliminates quadrupolar coupling, and both dipolar and quadrupolar nuclei have comparably narrow lines, if introduced to the lattice in low concentrations. Scandium ion is smaller than other three-valent ions commonly used for doping, and its solubility in ceria is limited due to size mismatch [30]. Due to small ion radius, 0.87 Å for Sc^{3+}, compared to 0.97 Å for Ce^{4+}, scandium ion neighborhood and dynamics are expected to be different from cerium ion neighborhood. It is expected to bind vacancy stronger than larger dopant ions, and provide lower ion conductivity [31].

Scandium is a good NMR nucleus with high sensitivity and modest quadrupole coupling, giving two lines in Sc doped ceria: an eight coordinated scandium and a seven coordinated scandium—oxygen vacancy complex [17–20].

In previous work [20] we presented a detailed investigation of oxygen dynamics in 0.5% scandium doped ceria from 60 K to 1073 K by solid state ^{45}Sc NMR line shape analysis. We showed that oxygen vacancy was strongly attached to the scandium in the seven coordinated scandium—oxygen vacancy complex, but even at room temperature the vacancy was moving freely around scandium atom between eight equivalent sites in a millisecond time scale.

In this work we present the first study of the temperature dependence of the ^{45}Sc spin-lattice relaxation in scandium doped ceria, allowing detailed study of local dynamics around individual scandium ions. We demonstrate that four different activated processes are involved in scandium doped ceria in the temperature range from 60 K to 1073 K, only one being associated with oxygen vacancy jumps. This vacancy jumping around isolated scandium ion, however, does not contribute to ionic diffusion. Thus, none of these four processes could be directly associated with long distance oxygen diffusion in scandium doped ceria.

Here we investigate the relaxation behavior of the same 0.5% scandium doped ceria material that we investigated in [20], and that work should be consulted for NMR spectra for which the relaxation is measured.

2. Experimental

Scandium doped ceria $Sc_xCe_{1-x}O_{2-x/2}$ with x = 0.005 (0.5%SDC) was synthesized by citrate route from corresponding nitrates [20,32]. Appropriate amounts of $Sc(NO_3)_3$ and $Ce(NO_3)_3$ aqueous solutions were added to neutralized oxalic acid solution. After precipitation the product was washed, dried and subsequently heated to 500 °C. For relaxation measurements the powders were isostatically pressed into 5 mm rods with length of 20 mm, and sintered at 1600 °C for 3 h. Part of the powder was calcined at 1600 °C without pressing for MAS NMR analysis.

^{45}Sc MAS NMR spectra were recorded on AVANCE-II-600, in 14.1 T magnetic field (^{45}Sc resonance frequency 145.8 MHz) using home built MAS probe and 4 mm zirconia rotors. The spectra were referenced to resonance frequency of $Sc(NO_3)_3$ solution in water. Different sample spinning speeds were used, 7 kHz was adequate for suppressing all dipolar broadening interactions.

Temperature dependence of ^{45}Sc spin-lattice relaxation of the static 0.5%SDC samples was measured at two magnetic fields 8.5 T and 4.7 T using saturation recovery pulse sequence. These measurements were carried out on a Bruker AMX 360 spectrometer using home built high temperature probe and low temperature probe. The latter was operating in He gas flow cryostat from Janis Research Company.

3. Results and discussion

3.1. Powder NMR spectra

^{45}Sc MAS NMR spectrum of 0.5%SDC powder is presented on Fig. 1. We have at room temperature only two narrow lines in SDC, corresponding to isolated 7-coordinated (7-Sc), and 8-coordinated (8-Sc) Sc centers at 36.1 ppm and −20.7 ppm, respectively.

The ratio of 7-Sc and 8-Sc ions depends on scandium concentration, defect association and availability of additional centers capable to bind oxygen vacancies. In the lattice of ceria the cations form a

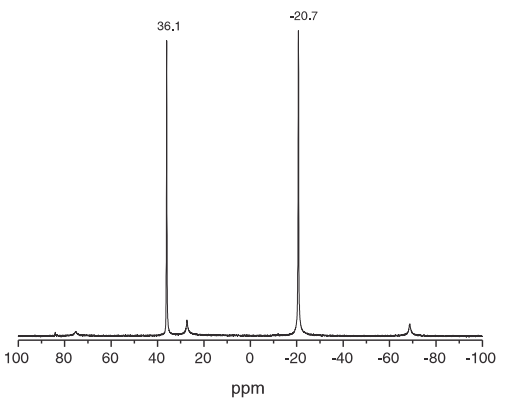

Fig. 1. ^{45}Sc MAS NMR spectrum of 0.5%SDC powder in 14.1 T magnetic field, at room temperature. The weak lines at 74, 27 and −68 ppm are rotational sidebands of the 8-Sc line.

fcc close packed sublattice, and every cation has 12 nearest neighbor cations. Therefore, in 0.5%SDC, at random distribution of scandium ions, only 6% of scandium ions form dimers, where scandium ion has another scandium ion as the nearest neighbor cation, and the spectra are dominated by single scandium ion lines. If the vacancies were distributed randomly in the lattice, the intensity of 7-Sc line would be only 1%. On the other hand, if there was significant attraction between scandium ions and vacancies, as suggested by earlier experiments [17,29] and calculations [8], we would see equal amount of 7-Sc and 8-Sc sites and a small number of neutral scandium – scandium dimer – vacancy complexes, as there is one oxygen vacancy formed per two scandium ions. The ratio of 7-Sc and 8-Sc is not altered, if the scandium dimer concentration is somewhat higher than predicted from random distribution of scandium ions, as the scandium dimer—vacancy complexes are neutral, and we see still equal amount of 7-Sc and 8-Sc sites. Experimentally, the exact ratio of 7-Sc to 8-Sc was hard to determine from spectra, as the distribution of intensity between sidebands was different for these sites. While MAS spectra gave 7-Sc to 8-Sc ratio 47:53, static spectra gave the ratio 54:46. Overall, the simple model of strong attraction of vacancies to scandium ions works well, and we rely on it in this work.

A remarkable feature here is the almost complete lack of rotational sidebands of 7-Sc-vacancy complex that should be of lower symmetry than 8-Sc site. The explanation comes from our previous work: At room temperature the vacancy is freely rotating around scandium ion, averaging out both quadrupolar and chemical shift anisotropies [20]. At room temperature almost equal line widths (~3 ppm) for the resonances of 7-Sc and 8-Sc sites show up in the spectra of static sample as well.

^{45}Sc NMR spectra at 100 K, 250 K and 723 K are presented in Fig. 2. On the high temperature side, around 500 K both lines become broader and at 633 K coalesced into one line in the middle, due to the fast oxygen vacancy hopping between scandium ions, as oxygen ions had become mobile in the ceria lattice. Detailed analysis of this process was given in [19] and in our previous publication [20]. On the low temperature side, the 7-Sc line first broadens at 218 K, and then obtains characteristic shape of a powder line due to chemical shift anisotropy at T < 188 K, with a width of 27 ppm. Below 100 K we did not detect any further change of the lineshape [20].

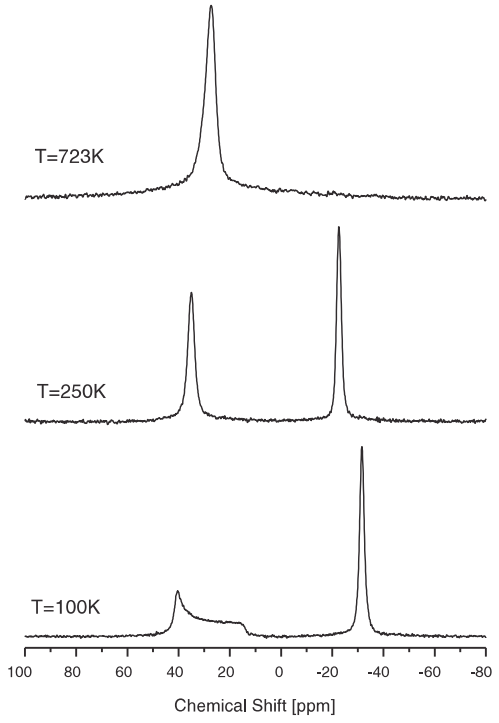

Fig. 2. Temperature dependence ^{45}Sc NMR spectra of 0.5%SDC static powder in 8.5 T magnetic field. Three characteristic spectra from different temperature regions are presented.

3.2. Temperature dependent spin-lattice relaxation

3.2.1. Theory

To make sense of our measured temperature dependencies of scandium T_1 relaxation, a short look into the theory of spin-lattice relaxation is necessary. There are different possible mechanisms for spin-lattice relaxation in solid lattice [25]. However, for an isolated quadrupole nucleus, in the absence of electronic magnetism, the dominating interaction causing relaxation is coupling of the nuclear quadrupole moment to the electrical field gradient (efg) fluctuations at the nucleus position. These fluctuations can be induced by thermal lattice vibrations or by sudden changes of molecular surroundings, e.g. oxygen vacancy jumps. Specifically, if the spin temperature assumption holds, it is proportional to the spectral density of these fluctuations at Larmor frequency ω_L:

$$T_1^{-1} = A[J(\omega_L) + 4J(2\omega_L)] \tag{1}$$

where A measures the quadrupolar coupling strength. This spectral density is the Fourier transform of the correlation function of the efg fluctuations

$$J(\omega_0) = \int_{-\infty}^{\infty} G(\tau)\exp(-i\omega_L\tau)d\tau. \tag{2}$$

If the fluctuations are due to uncorrelated jumps between different equivalent configurations in the lattice, e.g. wandering of the vacancy around scandium ion between 8 equivalent positions, the process can be described by an exponentially decaying correlation function with a single correlation time τ_c, and the spectral density is

$$J(\omega) = F_0^2\frac{2\tau_c}{1+\omega^2\tau_c^2} \tag{3}$$

where F_0 is the amplitude of the fluctuations. In the case for the classical BPP theory [25] the relaxation rate can be expressed in a form:

$$T_1^{-1} = C\left[\frac{\tau_c}{1+\omega_L{}^2\tau_c{}^2} + \frac{4\tau_c}{1+4\omega_L{}^2\tau_c{}^2}\right] \tag{4}$$

where C is a constant characterizing the amplitude of the fluctuations of the quadrupolar interaction, ω_L is the Larmor frequency. In the case of activated process the correlation time τ_c of the fluctuations follows exponential temperature dependence

$$\tau_c = \tau_0\exp\left(\frac{E_a}{k_BT}\right) \tag{5}$$

where E_a is the activation energy of the process, T is the temperature, and the pre-exponential factor τ_0^{-1} is the attempt frequency. In this case it is straightforward to determine activation energy from the slope in the Arrhenius plot $ln(T_1^{-1})$ vs $1/T$ at low temperatures where $\omega_L{}^2\tau_c{}^2 \gg 1$ or at high temperatures where $\omega_L{}^2\tau_c{}^2 \ll 1$. This relaxation rate depends on magnetic field, as the correlation time is compared to the Larmor frequency of the transition, and has maximum at $\omega_L\tau_c = 0.7$. In case this maximum is measured, one has a unique possibility to determine absolute value of the correlation time τ_c almost model free. However, if the different configurations in the process have different energies, the uncorrelated jump

assumption breaks down, as the system spends less time in the higher energy configurations. In the case of double well potential with inequivalent minima, Blinc [33] has shown that the approach is still usable with some modifications. If the energies of the configurations are E_1 and E_2, $\Delta E = E_2 - E_1$, the spectral density of the fluctuations can be expressed as

$$J(\omega) = F_0^2 \frac{2\tau_c}{1+\omega^2\tau_c^2}\frac{4a}{(1+a)^2} \tag{6}$$

where a is the ratio of the probabilities for the system to be in these configurations

$$a = e^{-\Delta E/kT} \tag{7}$$

and τ_c is now the average time between jumps,

$$\frac{1}{\tau_c} = W_{12} + W_{21} = (1+a)W_{12} \tag{8}$$

where W_{12} and W_{21} are transition probabilities between these configurations. We have here an additional temperature dependence through configuration occupancy ratio a. The temperature dependence of the correlation time is not strong, it can change only from $2W_{12}$ at $\Delta E \ll kT$ to W_{12} at $\Delta E \gg kT$, but $J(\omega)$ can change significantly due to exponential temperature dependence of a. This approach does not imply any detailed information about the potential form, just the energy difference and the principle of detailed balance at thermodynamic equilibrium. However, it implicitly assumes equal densities of states in both potential wells, and this is not so in general. Or, as we shall see in our case of 8-Sc, we have jumps between high symmetry equilibrium configuration and several higher energy configurations of lower symmetry (there cannot be just one higher energy configuration because of the high symmetry of the lattice), we have to modify the occupancy ratio, and the formula (7) becomes

$$a = a_0 e^{-\Delta E/kT}. \tag{9}$$

To have an idea how these considerations modify the analysis compared to standard BPP theory, we have made some simulations of relaxation temperature dependencies with different assumptions. Simulations in Fig. 3 show temperature dependence of the transition probability for the simple BPP model together with different energy site model with $a_0 = 1$ and $a_0 = 8$.

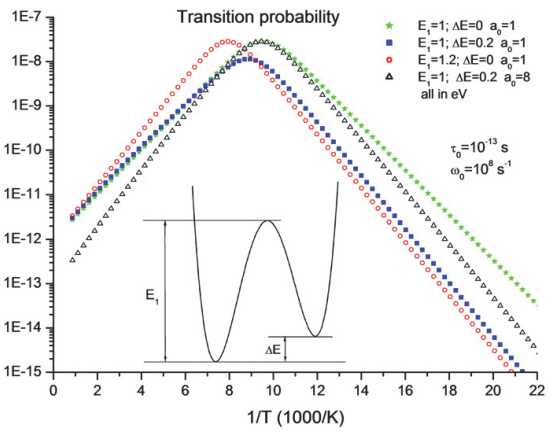

Fig. 3. Simulation of the transition probabilities for nuclear spin based on formulas (6) to (9).

In fact, in the case of unequal site energies, the exponential temperature dependencies of a and τ_c simply add in the low temperature side where $\omega_L^2\tau_c^2 \gg 1$, and the process looks like simple hopping between similar sites with activation energy $E_1 + \Delta E$. This result is not changed by different number of higher energy sites. The maximum of the relaxation curve and associated correlation time are, however, hard to interpret, as we seldom know detailed properties of these higher energy sites. On the high temperature side the temperature dependence of relaxation approaches that of the BPP theory, as ΔE becomes insignificant, but this range is experimentally hard to explore.

This situation is quite common in ionic conductivity analysis, as the different vacancy positions near dopant ion are often of different energy. The same applies to 8-Sc in our case. We know that the equilibrium configuration of the scandium ion has cubic symmetry, and that there is another configuration of lower symmetry at higher energy, separated by a potential barrier, but we do not know the energy of that configuration.

At low temperature, where the frequency of the jumps gets low compared to the Larmor frequency, the lattice phonon related quadrupole relaxation mechanism takes over. In a classical work [24] Kranendonk has shown that the phonon related relaxation is dominated by a two phonon Raman processes, where one phonon is absorbed and another created, with energy difference equal to spin transition energy. A Raman process induced relaxation is usually independent of magnetic field. In the harmonic approximation, the relaxation rate can be expressed as

$$T_1^{-1} = A\frac{f(\omega)}{\omega^2}\int \frac{e^{\hbar\omega/kT}}{\left(e^{\hbar\omega/kT}-1\right)^2}d\omega \tag{10}$$

where ω is the phonon frequency and $f(\omega)$ is the phonon density, and A characterizes the coupling of phonons to nuclear quadrupole moment. If the phonon density at the nucleus site can be approximated by Debye model, the relaxation rate is proportional to temperature squared, $T_1^{-1} \propto T^2$ in temperature range above the Debye temperature. In practice, the behavior is observed in many materials in temperature range above $T > 100$ K [25].

However, for phonon related relaxation of impurity centers, the applicability of the Debye model is not obvious. In Debye model the relaxation is dominated by low frequency acoustical phonons that all induce comparable but weak efg at nucleus site. The efg at the impurity nucleus in the lattice, on the other hand, can be dominated by local phonon modes that distort the neighborhood significantly, as shown by ^{139}La relaxation by rattling motion in an oversized cage [34,35]. If these local phonons have characteristic frequency, ω_c, we get from Eq. (10)

$$T_1^{-1} = A'\frac{e^{\hbar\omega_c/kT}}{\left(e^{\hbar\omega_c/kT}-1\right)^2} \tag{11}$$

and for temperatures $kT < \hbar\omega_c$, Eq. (11) can be approximated by

$$T_1^{-1} = Be^{-\hbar\omega/kT} \tag{12}$$

where B incorporates all temperature independent coupling parameters. This relaxation again looks like an activated process, however, it does not depend on the magnetic field. The formula (11) is obtained for a harmonic local vibration, and the exact temperature behavior of the relaxation depends sensitively on the real potential surface for the local motion [35]. This potential surface is not known in our case. However, the low temperature approximation in Eq. (12) depends only on the existence of the lowest excited level at energy ω_c, and is independent of the energy spectrum above this level.

So the magnetic field independent exponential temperature dependence of T_1 points to a Raman process induced by a local lattice vibration.

Measurements in different magnetic fields are important here to separate between different relaxation mechanisms.

3.2.2. Relaxation

Spin lattice relaxation in quadrupolar nuclei is, in general, multi-exponential, the exact ratios of different components depend on both excitation (initially prepared state), and spectral density of the perturbation that is causing relaxation [36–38]. In the limiting case of "extreme narrowing", when the correlation time of the perturbation is much smaller than reciprocal Larmor frequency, or when the thermal equilibrium between different spin states is maintained throughout the process, the relaxation is the single exponential, and $1/T_1 = 2W$ ($T_1 = \tau$, where τ is the correlation time), where W is the transition probability between spin levels for both single and double quantum transitions. However, when the correlation time is not short, as in the range where activated hopping dominates the process, single and double quantum transitions have different probabilities, and some deviations from single exponential relaxation emerge, producing faster relaxation components with small amplitude [39,40].

In our case the saturation radio frequency excitation field strength is 50 kHz. The nutation spectra were independent of the excitation field between 15 and 60 kHz and show that all transitions in Sc are excited and detected together. The saturation comb length was 10 ms, and provided even saturation of all transitions. We see small fast relaxation components in some cases, but their influence to total relaxation time is smaller than experimental uncertainty [39]. In all our analysis we use single exponential fitting to the saturation recovery curves.

Spin-lattice relaxation temperature dependence for 7-Sc and 8-Sc in two different magnetic fields are presented on Fig. 4. Four different relaxation processes can be separated, two for both centers. None of these processes could be directly associated with oxygen vacancy hopping processes, responsible for ion conductivity in scandium doped ceria, as the activation energy for ion conduction in scandium doped ceria is over 1 eV [19], three times higher than our highest activation energy. This is the sum of vacancy hopping barrier in pure ceria and vacancy binding energy to scandium ion, we know that vacancy is dominantly bound to scandium ion even at 800 °C [20]. This high barrier hopping, however, does not dominate scandium relaxation in the measured temperature range.

7-Sc has a low temperature relaxation process that does not depend on magnetic field, and a high temperature relaxation process that has characteristic magnetic field dependence of the activated hopping. Moreover, the high temperature relaxation has a maximum at 430 K in the 8.5 T magnetic field, and all parameters of the process can be determined: Activation energy $E_a = 0.37$ eV, attempt frequency $\tau_0^{-1} = 6.3 \times 10^{12}\ s^{-1}$, and squared amplitude of quadrupolar fluctuations $C = 2 \times 10^{10}\ s^{-2}$. We identify the high temperature process with the activated jumping of the oxygen vacancy around scandium ion, as the correlation time for this process at 220 K, determined from relaxation, fits well with the correlation time determined from the line broadening process, 70 μs. The low temperature relaxation has exponential temperature dependence as well, but the magnetic field independence points to the Raman process. We interpret this as a relaxation induced by a low symmetry local mode, the low activation energy of 0.026 eV (208 cm^{-1}) is plausible for this kind of movement.

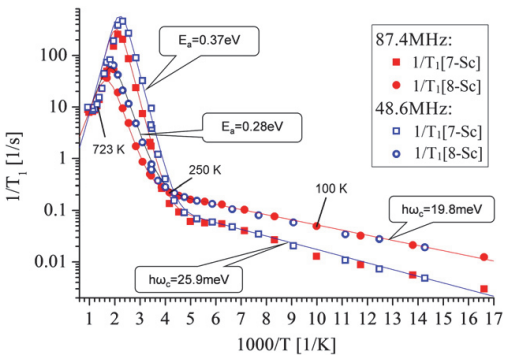

Fig. 4. ^{45}Sc spin-lattice relaxation rate $1/T_1$ for 7-Sc and 8-Sc centers in two different resonance fields over temperature range from 60 to 1073 K. Three temperatures are indicated, for which spectra are presented on Fig. 2. Continuous lines correspond to fits with indicated parameters.

The biggest uncertainties in the measured parameters come from the models used: simple activated hopping with one attempt frequency and fixed amplitude of efg fluctuation for high temperature processes, and a single frequency Raman process for the low temperature relaxation. Still, we believe that the high temperature apparent activation energies could be determined to better the 5% accuracy, however the characteristic frequency for the low temperature Raman process is only indicative of a distribution of Raman active local phonons, and can be used to assess the rigidity of the surroundings of dopant ions, 7-Sc and 8-Sc in our case.

8-Sc relaxation shows again two processes, one field independent at low temperature and one field dependent at higher temperature. At 600 K 8-Sc and 7-Sc coalesce due to vacancy movement in the lattice, and no separate relaxation process can be assigned to the centers.

These two processes have different activation energies and amplitudes from 7-Sc processes, and have to be treated as specific 8-Sc processes. The structure of the eight-coordinated scandium in the ceria lattice has been under discussion for a long time. It has been argued, based on anelastic and dielectric relaxation measurements, that 8-Sc cage in ceria should be lower than cubic symmetry [29], and low temperature relaxation mode corresponds to movement between different low symmetry configurations. Later calculations [41] tentatively supported this conclusion, but the result depended sensitively on the polarization parameters of scandium ion, and these were not known. In our previous publication [20] we showed that equilibrium structure of the 8-Sc has the symmetry of the undisturbed lattice that can be seen in Fig. 2 as well: the 8-Sc line stays narrow down to the lowest temperature.

The low temperature process involves vibration with a characteristic energy of 0.020 eV (160 cm^{-1}), even lower than 7-Sc. At the lowest temperature 8-Sc relaxes almost ten times faster than 7-Sc. The softness of this mode might explain the stronger chemical shift temperature dependence of 8-Sc than 7-Sc [20], since the oversized cage of 8-Sc is very flexible.

The high temperature process is an activated process with apparent activation energy of 0.28 eV, but this process has lower amplitude than vacancy rotation in 7-Sc. However, it is not hopping between equivalent sites. We know that the lowest energy position is of cubic symmetry, so the other (metastable) potential wells must be of higher energy. There are at least four of these potential wells, but could be more, depending on the exact symmetry breaking. Our analysis in the previous section shows that in this case the apparent activation energy is not the barrier height from the lowest energy position. Both amplitude and apparent activation energy of the process depend on the energy of the other site involved in the jumping. In our case the apparent exponential activation energy that is the sum of the barrier height and energy difference between potential wells that we do not know, and shows the upper limit to the barrier height.

Both these observations indicate that 8-Sc has complicated potential surface. The low temperature process shows that there are low frequency modes significantly distorting the symmetry of the 8-Sc cage, and the high temperature process can be explained only if we

assume a lower symmetry metastable configuration, separated by less than 0.28 eV barrier from symmetrical equilibrium configuration.

The processes seen in dielectric and inelastic relaxation study of Gerhardt et al. [29] agree with our high temperature processes: Their low temperature process with 0.23 eV activation energy corresponds to our 0.28 eV process in 8-Sc, and their high temperature A process with activation energy of 0.41 eV corresponds to vacancy rotation in 7-Sc, for what we measured the activation energy of 0.37 eV. However, the activation energies in dielectric relaxation and NMR were measured at different temperatures. In dielectric relaxation the activation energies were determined around 125 K and 230 K for 8-Sc and 7-Sc respectively, where the characteristic frequency of the processes was between 1 and 5 kHz. In our case the relaxation was measured between 250 K and 550 K, and we believe this is the reason for the somewhat different activation energies obtained.

4. Conclusions

Scandium spin-lattice relaxation temperature dependence in ceria matrix revealed four separate processes, two for 8-coordinated scandium and two for 7-coordinated scandium. However, none of these processes could be associated with oxygen vacancy hopping processes responsible for long-range ion conductivity in scandium doped ceria.

We have established that for 7-Sc, the high temperature process was an activated vacancy hopping around the scandium ion with activation energy 0.37 eV and the low temperature process was a Raman process involving local vibrations with characteristic energy 26 meV (208 cm^{-1}).

For 8-Sc, the high temperature process is an activated hopping between potential wells with different energy minima with apparent activation energy of 0.28 eV. This cannot be a vacancy related process, as there are no vacancies around. This can be, however, a switching between different metastable local potential minima of the unstable 8-Sc cage. We have shown that in this case the apparent activation energy of the process does not correspond to barrier height for hopping, but to barrier height plus energy difference between minima of corresponding potential wells. The low energy process is again a Raman process involving local vibrations with even lower characteristic energy 20 meV (160 cm^{-1}). This shows that the 8-coordinated scandium cage in ceria has very complicated potential surface with multiple minima due to small size of the scandium ion.

Acknowledgments

This study has been supported by the Estonian Science Foundation grant 8198, by grant SF0690034s09 from the Estonian Ministry of Education and by AS Elcogen.

References

[1] L. Vivier, D. Duprez, ChemSusChem 3 (2010) 654.
[2] A. Trovarelli, C. de Leitenburg, M. Boaro, G. Dolcetti, Catal. Today 50 (1999) 353.
[3] R.J. Gorte, AICHE J. 56 (2010) 1126.
[4] J. Gomes, O.A. Serra, J. Mater. Sci. 43 (2008) 546.
[5] T. Taniguchi, Y. Sonoda, M. Echikawa, Y. Watanabe, K. Hatakeyama, S. Ida, M. Koinuma, Y. Matsumoto, ACS Appl. Mater. Interfaces 4 (2012) 1010.
[6] J. Faber, G.C. Roux, A. Sylvestre, P. Abélard, Appl. Phys. A 49 (1989) 225.
[7] M. Mogensen, N.M. Sames, G.A. Topsett, Solid State Ionics 129 (2000) 63.
[8] M. Nakayama, M. Martin, Phys. Chem. Chem. Phys. 11 (2009) 3241.
[9] H. Hayashia, R. Sagawaa, H. Inabaa, K. Kawamurab, Solid State Ionics 131 (2000) 281.
[10] L. Minervini, M.O. Zacate, R.W. Grimes, Solid State Ionics 116 (1999) 339.
[11] K. Fuda, K. Kishio, S. Yamauchi, K. Fueki, J. Phys. Chem. Solids 4 (1984) 1253–1257.
[12] K. Fuda, K. Kishioa, S. Yamauchia, K. Fuekia, J. Phys. Chem. Solids 46 (1985) 1141.
[13] T. Viefhaus, T. Bolse, K. Müller, Solid State Ionics 177 (2006) 3063.
[14] N.J. Kim, J.F. Stebbins, Chem. Mater. 19 (2007) 5742.
[15] I. Heinmaa, T. Joon, H. Kooskora, J. Subbi, Solid State Ionics 181 (2010) 1309.
[16] M. Ando, I. Oikawa, Y. Noda, S. Ohki, M. Tansho, T. Shimizu, H. Kiyono, H. Maekawa, Solid State Ionics 192 (2011) 576.
[17] P. Jain, Hugo J. Avila-Paredes, C. Gapuz, S. Sen, S. Kim, J. Phys. Chem. C 113 (2009) 6553.
[18] S. Kim, P. Jain, Hugo J. Avila-Paredes, A. Thron, K. van Benthem, S. Sen, J. Mater. Chem. 20 (2010) 3855.
[19] Hugo J. Avila-Paredes, P. Jain, S. Sen, S. Kim, Chem. Mater. 22 (2010) 893.
[20] J. Subbi, I. Heinmaa, R. Põder, H. Kooskora, Solid State Ionics 225 (2012) 488.
[21] S. Sen, Hugo J. Avila-Paredes, S. Kim, J. Mater. Chem. 18 (2008) 3915.
[22] K. Kawata, H. Maekawa, T. Nemoto, T. Yamamura, Solid State Ionics 177 (2006) 1687.
[23] H. Maekawa, K. Kawata, Y. Xiong, N. Sakai, H. Yokokawa, Solid State Ionics 180 (2009) 314.
[24] J. Van Kranendonk, Physica 20 (1954) 781.
[25] A. Abragam, The Principles of Nuclear Magnetism, Oxford University Press, London, 1961.
[26] P. Heitjans, S. Indris, J. Phys. Condens. Matter 15 (2003) R1257.
[27] D.R. Figueroa, A.V. Chadwick, J.H. Strange, J. Phys. C Solid State Phys. 11 (1978) 55.
[28] J.W. Fergus, J. Power Sources 162 (2006) 30.
[29] R. Gerhardt, W.-K. Lee, A.S. Nowick, J. Phys. Chem. Solids 48 (1987) 563.
[30] P. Li, I. Chen, J.E. Penner-Hahn, T. Tien, J. Am. Ceram. Soc. 74 (1991) 958.
[31] R. Gerhardt-Anderson, A.S. Nowick, Solid State Ionics 5 (1981) 547.
[32] J.V. Herle, T. Horita, T. Kawada, N. Sakai, H. Yokokawa, M. Dokiya, J. Am. Ceram. Soc. 80 (1997) 933.
[33] R. Blinc, Adv. Magn. Reson. 3 (1968) 141.
[34] T. Dahm, K. Ueda, Phys. Rev. Lett. 99 (2007) 187003.
[35] Y. Nakai, K. Ishida, H. Sugawara, D. Kikuchi, H. Sato, Phys. Rev. B77 (2008) 041101.
[36] E.R. Andrew, D.P. Tunstall, Proc. Phys. Soc. 78 (1961) 1.
[37] M.I. Gordon, M.J.R. Hoch, J. Phys. C Solid State Phys. 11 (1978) 783.
[38] P.S. Hubbard, J. Chem. Phys. 53 (1970) 985.
[39] J. Reuben, Z. Luz, J. Phys. Chem. 80 (1976) 1357.
[40] T.E. Bull, S. Forsen, D.L. Turner, J. Chem. Phys. 70 (1979) 3106.
[41] A.N. Cormack, C.R.A. Catlow, A.S. Nowick, J. Phys. Chem. Solids 50 (1989) 177.

PUBLICATION 3

Reio Põder, Juhan Subbi, Helgi Kooskora, Ivo Heinmaa, *Vacancy association energy in scandium doped ceria: ^{45}Sc MAS NMR and 2D exchange spectroscopy study*, Solid State Ionics 267 (2014) 49-53.

Solid State Ionics 267 (2014) 49–53

Contents lists available at ScienceDirect

Solid State Ionics

journal homepage: www.elsevier.com/locate/ssi

Vacancy association energy in scandium doped ceria: ^{45}Sc MAS NMR and 2D exchange spectroscopy study

Reio Põder, Juhan Subbi, Helgi Kooskora, Ivo Heinmaa *

National Institute of Chemical Physics and Biophysics, 23 Akadeemia tee, Tallinn 12618, Estonia

ARTICLE INFO

Article history:
Received 16 June 2014
Received in revised form 29 August 2014
Accepted 9 September 2014
Available online xxxx

Keywords:
Ceria
Scandium
Oxygen dynamics
Solid state NMR
EXSY

ABSTRACT

Oxygen vacancy exchange between Sc ions in 0.5% Sc-doped ceria $Sc_{0.005}Ce_{0.995}O_{0.9975}$ is investigated by means of 2D exchange spectroscopy (EXSY). ^{45}Sc NMR spectrum of Sc-doped ceria contains two peaks—one corresponding to Sc ions coupled with an oxygen vacancy (Sc-7), and the other corresponding to Sc ions in a regular lattice site surrounded by eight oxygen ions (Sc-8). The vacancy exchange between these two Sc sites generates the cross-peaks in the EXSY spectrum. Relative amplitudes of the cross-peaks provide direct values of the exchange frequency at a given temperature. Arrhenius analysis of the exchange frequency gives the activation energy $E_a = 1.18$ eV for the vacancy hopping between Sc sites. Most of this energy barrier is due to association energy which binds the vacancy to Sc^{3+}. Large dopant–vacancy association energy in Sc doped ceria is demonstrated by ^{45}Sc NMR spectrum of La/Sc doubly doped sample, $Sc_xLa_xCe_{1-2x}O_{2-x}$, $x = 0.005$, where the only line of Sc-7 site shows that all vacancies are bound by Sc^{3+} ions.

1. Introduction

Doped ceria is an oxygen ion conductor which can be used in various applications, e.g. as a three-way catalyst in exhaust systems of car engines [1,2], in fluorescent screens [3,4], in gas sensors [5,6], and in solid oxide fuel cells (SOFC) [7–9]. To use ceria as an ionic conductor, e.g. in SOFC as an electrolyte, ceria is doped with aliovalent ions in order to introduce oxygen vacancies which become mobile and cause ionic conductivity at high temperatures. The most suitable dopants for this purpose are trivalent ions Gd^{3+} and Sm^{3+}. The reason for being the best dopants was proposed [8] that Gd^{3+} and Sm^{3+} fit into the ceria lattice without causing considerable lattice distortions. Optimal concentration for dopants is 10–20%.

Ionic conductivity (σ) is determined by the activation energy E_a for the vacancy diffusion and the temperature T:

$$\sigma T = \sigma_0 \exp\left(-\frac{E_a}{k_B T}\right), \quad (1)$$

where σ_0 is a pre-exponential factor and k_B is the Boltzmann constant. In commonly accepted description of doped ceria [8,10–14] the vacancies are bound to the dopant ions forming stable associates with a certain binding- or association energy E_{ass}. This is the energy which prevents the vacancies from being mobile. Therefore the activation energy is the sum of two contributions: $E_a = E_{ass} + E_{bulk}$, where E_{bulk} is the migration barrier for vacancy diffusion in the lattice of pure ceria. By definition E_{bulk} is dopant independent, thus the association energy is a key parameter to account the different ionic conductivities for different dopants.

A number of first-principles computational studies have recently been successfully applied to calculate the association energies and migration barriers in doped ceria [15–20]. The calculations show that in case of small trivalent dopants, smaller than Gd^{3+} ions [15,16], the oxygen vacancies occupy the nearest neighbor (NN) position, whereas in case of large dopants the vacancy occupies the next nearest neighbor (NNN) position. These calculations also provide energy barriers for vacancy migration in doped ceria and give a valuable hint for getting highest ionic conductivity in ceria [19]: the dopant must be large enough to avoid strong trapping of the vacancy in NN sites yet small enough to have easily surmountable migration barriers. The highest association energy $E_{ass} = 0.43$ eV was calculated for the NN vacancy at Sc^{3+} dopants [16].

There are not too many experimental techniques to study the mechanisms of the vacancy diffusion in atomic level. The main techniques used to study oxygen migration in doped ceria are based on the ac impedance analysis of the electrical conductivity [7,13]. The other techniques are dielectric relaxation measurements [21] and nuclear magnetic resonance (NMR). NMR has proved to be a very useful technique for studies of the local structure and dynamics in doped ceria [22–33]. In their pioneering work Fuda et al. [22,23] studied the temperature dependence of ^{17}O spin lattice relaxation in yttrium doped ceria (YDC).

* Corresponding author. Tel.: +372 6398350.
E-mail address: ivo.heinmaa@kbfi.ee (I. Heinmaa).

http://dx.doi.org/10.1016/j.ssi.2014.09.010
0167-2738/

At low doping level the relaxation vs temperature curve showed two characteristic maxima which were ascribed to two different relaxation processes. The relaxation process at low temperature (T < 600 K) was ascribed to vacancy hopping in pure ceria with activation energy of $E_a = 0.49$ eV. The relaxation process at higher temperatures was not assigned.

We found lately similar relaxation behavior of ^{17}O in La^{3+} doped ceria (LDC) [29]. In samples of low doping level we saw at temperatures T < 600 K the oxygen hopping with an activation energy of $E_a = 0.45$ eV. At higher temperature the relaxation process was described by the activation energy E_a=0.96 eV. The latter process was attributed to the vacancy diffusion through the lattice while the origin of the low temperature relaxation process was unclear at that time.

An interesting NMR work has been done on Sc^{3+} doped ceria (ScDC) [27–31,33]. There is one oxygen vacancy for every two Sc^{3+} dopant ions, thus half of the Sc dopants are coupled with a vacancy (7-Sc), and the other half have a regular surrounding of eight oxygen ions (8-Sc). Accordingly, there are two ^{45}Sc NMR lines in the spectrum of SDC—one corresponding to 7-Sc, and the other one corresponding to 8-Sc [26]. The analysis of the temperature dependence of the line shape in 5% Sc doped ceria [28] yielded the activation energy for ionic diffusion $E_a = 1.19$ eV in good agreement with the conductivity measurements. Recently we studied ^{45}Sc NMR spectrum and spin–lattice relaxation of ^{45}Sc in ScDC in a wide temperature region [30,31]. We discovered that the vacancy associated to the 7-Sc site starts hopping around the Sc ion already at low temperature, at T > 210 K. The relaxation measurements gave an activation energy for that motion $E_a = 0.37$ eV. In a very recent paper by Sen et al. this finding was perfectly confirmed. In the light of this finding, we believe that the low temperature relaxation of ^{17}O in YDC [22] and in LDC [29] is caused by the vacancy hopping around the dopant ion.

In this paper we present the activation energy measurements of the vacancy diffusion in 0.5% ScDC using exchange NMR spectroscopy (EXSY) [34,35]. As vacancies move between Sc ions, an exchange process takes place: when the vacancy leaves the site of 7-Sc, it becomes 8-Sc site and vice versa: when the vacancy reaches 8-Sc, it becomes 7-Sc. EXSY is a robust and straightforward tool for investigating such ionic exchange and has been successfully used e.g. in Li ion conductors [36,37]. In addition, using NMR spectrum of $La_{0.005}Sc_{0.005}Ce_{0.99}O_{1.995}$ doubly doped sample we will show that the association energy of the vacancy to Sc^{3+} is much larger than the energy which associates the vacancy to La^{3+} ions.

2. Experimental

The samples of scandium doped ceria $Sc_xCe_{1-x}O_{2-x/2}$, x = 0.005 and doubly doped $Sc_x La_xCe_{1-2x}O_{2-x}$, x = 0.005, are synthesized by citrate route from corresponding nitrate as described previously [29–31] (in the following we will use notations 0.5%ScDC, and 0.5%Sc0.5%LDC). Appropriate amounts of ScNO3, $La(NO_3)_3$ and $Ce(NO_3)_3$ aqueous solutions were added to neutralized oxalic acid solution. After precipitation the product was washed, dried and subsequently heated to 500 °C. For temperature dependent measurements the powder was isostatically pressed into a 5 mm rod with length of 20 mm, and sintered at 1600 °C for 3 h. The sample of 0.5%ScDC was used in our previous study [30,31].

^{45}Sc 2D exchange spectra of static 0.5%SDC sample were measured in 8.5T magnetic field (^{45}Sc resonance frequency 87.4 MHz) using home built high temperature probe and Bruker AVANCE-II-360 spectrometer.

High resolution ^{45}Sc MAS NMR spectra were recorded in 14.1T magnetic field (^{45}Sc resonance frequency 145.8 MHz) using Bruker AVANCE-II-600 spectrometer and home built MAS NMR probe for 4 mm zirconia rotors. The chemical shift is referenced to the resonance frequency of $Sc(NO_3)_3$ 0.06 M solution in D_2O.

3. Results

3.1. ^{45}Sc EXSY spectra and the vacancy exchange frequency

2D spectra of 0.5%ScDC were measured at temperatures of 240 °C, 260 °C, 280 °C and 295 °C. At these temperatures the lines of 7-Sc and 8-Sc were distinguishable and the vacancy exchange rate between them was slow enough to study the properties of vacancy exchange dynamics by 2D EXSY experiments. The pulse sequence for EXSY spectra was a standard sequence {p_1–t_1–p_2–τ_{mix}–p_3–acqusition}, where p_1, p_2 and p_3 are 90° pulses of appropriate phases, t_1 is an evolution (labeling) time, a delay incremented for indirect dimension (F1), and τ_{mix} is a mixing time for exchange process. The mixing time was varied from 0.3 ms to 5 ms, the number of slices in the indirect dimension was 256.

The EXSY spectra at 1 ms mixing time at given temperatures are shown in Fig. 1. The peaks on the diagonal at 42 ppm and −8 ppm belong to 7-Sc and 8-Sc sites, respectively. The cross-peaks appear after the mixing time when the ionic exchange has taken place. Relative amplitudes of the cross-peaks grow with growing mixing time. At short mixing time the amplitude of the cross peaks grow with rising temperature, as can be seen in Fig. 1. In 2D EXSY spectra the peak corresponding to 7-Sc sites is much smaller than 8-Sc peak. In ordinary 1D spectrum of the same sample the peaks have almost equal intensities (see Ref. [30]). The reason for such difference is that transverse relaxation time T_2 for 7-Sc site is much shorter than that for 8-Sc site: at 240 °C $T_2 = 0.33$ ms and 0.59 ms for 7-Sc and 8-Sc, respectively. Short T_2 causes considerable loss of the intensity during the evolution period t_1 of the experiment. It should not affect the exchange rate value since the latter is determined by modulation of z-component of the magnetization during the mixing time, τ_{mix}, where its decay is determined by longitudinal relaxation T_1 in both sites.

Relative amplitudes of the cross-peaks can be evaluated as [35]:

$$I_{AB}(\tau_{mix}) = I_{BA}(\tau_{mix}) = \frac{1-\exp(-R_C\tau_{mix})}{4}, \quad (2)$$

where τ_{mix} is the mixing time and R_C is the so called cross rate constant. At long mixing times, $R_C\tau_{mix} >> 1$, the cross peak amplitude approaches ¼. In the simplest case the cross rate constant gives directly the exchange frequency k, $R_C = 2k$. In case of fast and different T_1 relaxation at sites A and B the cross rate constant is evaluated as follows [35]:

$$R_C = 2\sqrt{k^2 + \frac{1}{4}\left(\frac{1}{T_{1A}} - \frac{1}{T_{1B}}\right)^2}, \quad (3)$$

where T_{1A} and T_{1B} are the spin–lattice relaxation times for the sites A and B, respectively.

In Fig. 2 the cross-peak intensities are plotted as a function of mixing time. The intensities in Fig. 2 are given as an average of the two cross peaks. The cross relaxation rate R_c was obtained by fitting the peak intensities by usual three parameter exponential function $I(\tau_{mix}) = A + B\exp(-R_C\tau_{mix})$, where the parameters A and B take into account uncertainties of the background integration of the 2D spectrum.

From the fittings we obtain the cross rate constant R_C and calculate the exchange rate k using Eq. (3) and previously measured T_1 values [31] as given in Table 1.

Despite of the fast and different relaxation rate at 7-Sc and 8-Sc sites, one can see that $k = R_C/2$ and corrections due to different relaxation times are irrelevant, except the case of 240 C.

Activation energy of the exchange rate E_A can be evaluated from the Arrhenius equation:

$$k(T) = k_0 \exp\left(\frac{-E_a}{k_B T}\right), \quad (4)$$

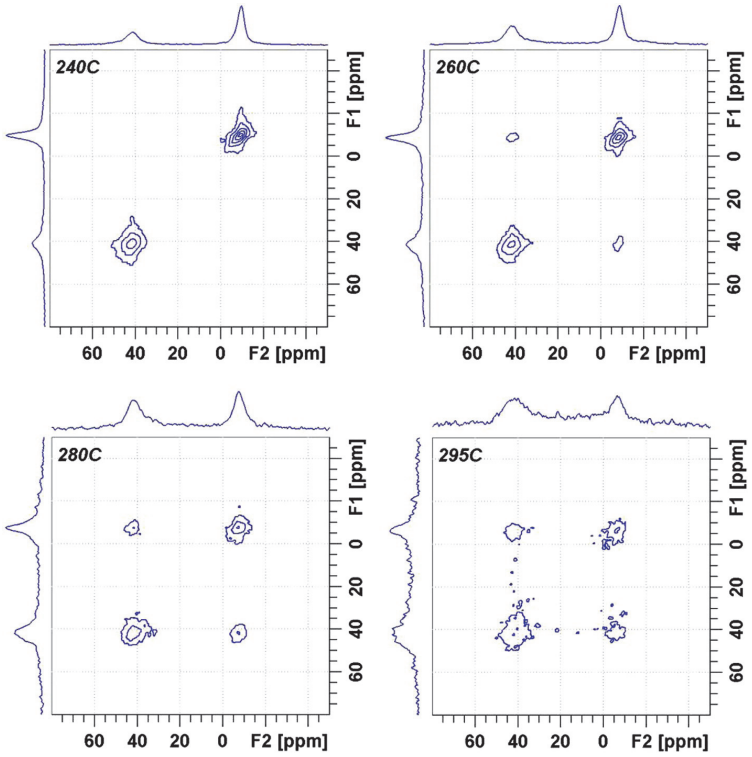

Fig. 1. ^{45}Sc NMR 2D EXSY spectra at temperatures between 240 °C and 295 °C, recorded with $\tau_{mix} = 1$ ms. The spectra are obtained by 256 slices in F1 dimension, each 128 accumulations, relaxation delay is 0.2 s.

where k_0 is the pre-exponential factor, an attempt frequency, and k_B is the Boltzmann constant. The Arrhenius plot in Fig. 3 reveals activation energy of the exchange process $E_a = 1.18 \pm 0.10$ eV and $k_0 = 5 \times 10^{13}$ s^{-1}.

The activation energy obtained in this work is in a good agreement with the results of Avila-Paredes et al. [28] $E_a = 1.19$ eV for 5%ScDC and with the very recent value $E_a = 1.2$ eV [33] for 0.5%ScDC from the fittings to the temperature dependence of the ^{45}Sc NMR line shapes. For comparison we added to the plot an exchange rate given in ref. [30] from the analysis of the spectrum at 633 K.

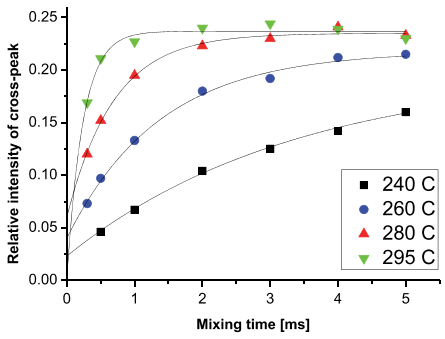

Fig. 2. Relative intensity of the cross-peaks as a function of mixing time. The curves present computer fit to the data by three parameter exponential function.

3.2. Vacancy association in Sc-doped ceria

The energy of vacancy association with Sc^{3+} ions in doped ceria can be compared with the association energy to the other dopants using NMR spectra of ^{45}Sc in doubly doped ceria. Fig. 4a shows the spectrum of La^{3+} and Sc^{3+} co-doped sample 0.5%La0.5%ScDC where only the line corresponding to the 7-Sc sites is present. The spectrum tells unambiguously that due to the higher association energy of Sc^{3+} all the vacancies induced by La^{3+} and Sc^{3+} in ceria lattice are associated with Sc ions. The spectrum of Sc^{3+} and Nb^{5+} co-doped sample 0.5%Nb0.5%ScDC sample (Fig. 4b) shows the case where only the line corresponding to 8-Sc sites is present. This means that no vacancies are present in donor and acceptor equally co-doped ceria. Similar spectrum is obtained for nano-sized (grain size ~25 nm) powder of 0.5%ScDC (Fig. 4c). Here the line of 7-Sc sites is missing because the vacancies are bound at the surface of the grains. After sintering of the same sample (3 h at 1300 °C) the spectrum becomes "normal" (Fig. 4d) showing two lines with nearly equal intensities.

Table 1
Experimental values of the cross rate constant $R_C/2$, spin–lattice relaxation times (from Ref 31) and calculated exchange frequency at studied temperatures.

Temperature [°C]	$R_C/2$ [s^{-1}]	T_{1A} (7-Sc) [ms]	T_{1B} (8-Sc) [ms]	k [s^{-1}]
240	148	6.6	18.5	140
260	365	9.7	13.5	365
280	726	14.2	16.7	726
295	2097	18.5	24.7	2097

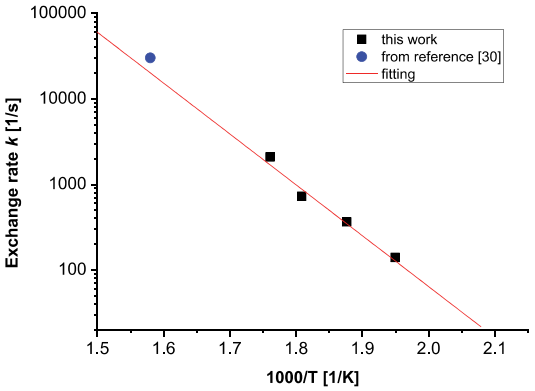

Fig. 3. Temperature dependence of the vacancy exchange rate k. The blue circle corresponds to the exchange rate at 633 K given in ref [30] by analysis of the spectrum where 7-Sc and 8-Sc lines become a single motionally averaged line. (For interpretation of the references to color in this figure legend, the reader is referred to the web version of this article.)

4. Discussion

Microscopic model of vacancy hopping in doped ceria involves quite many energy barriers [14–20]. From conductivity measurements only global activation energy for vacancy diffusion can be evaluated. The NMR experiments can provide the values of several hopping barriers if the fluctuation process causing nuclear relaxation is assigned correctly. So far the relaxation can be interpreted almost unambiguously at low doping levels only. At higher doping levels distribution of the activation barriers gives the temperature dependence of the nuclear relaxation which is difficult to interpret [23,29]. In Table 2 we have collected the vacancy hopping parameters in doped ceria obtained by NMR experiments. Here we have adopted the notations for the hopping pathways from Dholabhai et al. [17], where $E_{(1-1)}$ denotes the energy barrier for vacancy hopping between NN sites to the dopant, $E_{(2-2)}$ is that between NNN sites and E_a is the activation energy for global diffusion, from one dopant to another. We strongly believe that in LDC the low temperature relaxation of ^{17}O is caused by the vacancy hopping between the NNN sites to the dopant. The main arguments for that are i) the NMR spectrum of ^{139}La in LDC shows only one line [38] and ii) all the DFT calculations show that the vacancy in LDC occupies the NNN site to La^{3+} ion.

Vacancy association energy for ScDC can be obtained as $E_{ass} = E_a - E_{bulk}$. Unfortunately, experimental determination of E_{bulk} is difficult. It might be close to the $E_{(1-1)}$ value for YDC or $E_{(2-2)}$ value for LDC, hopping between the sites not much different from the pure lattice. Using the latest calculated value for $E_{bulk} = 0.47$ eV [18] (almost identical value $E_{bulk} = 0.482$ eV was obtained previously by Nakayama and Martin [16]), one obtains $E_{ass} = 0.71$ eV for ScDC, and $E_{ass} = 0.45$ eV for LDC. Such difference of the vacancy association energies for Sc^{3+} and La^{3+} dopants imply that at 300 K the probability to find vacancy at Sc^{3+} is ~10^4 times higher than that at La^{3+}. Indeed, ^{45}Sc NMR spectrum in Fig. 4a of co-doped compound $La_{0.005}Sc_{0.005}Ce_{0.01}O_{1.995}$, where one vacancy is introduced per one La and one Sc ion shows that all vacancies are bound by Sc ions.

^{45}Sc MAS NMR spectrum in Fig. 4c of nano-sized (grain diameter ~25 nm) ScDC powder shows that in this compound only the line corresponding to Sc-8 is present, consequently no vacancy is at Sc^{3+} ions since all the vacancies are bound by the surface of the grains. Thus, the energy which binds the vacancies to the surface is even larger than that binding the vacancy to Sc^{3+}. This experimental finding confirms earlier observation by Kim et al. [26] that oxygen vacancies in the surface region of ScDC are nearly immobile even at high temperatures. Here we have to point out a controversy between the spectrum in Fig. 4c and the spectra given in Ref 26 (Fig. 2): the spectrum in Fig. 4c shows only the line corresponding to Sc-8 sites, whereas the spectra of nano-sized ScDC in Ref [26] clearly show Sc-7 sites. We believe that the main reason of such different spectra is a different Sc concentration of the samples in Ref [26] (5%) compared to samples in this work (0.5%). We have noticed earlier [30] that in spectra of the ScDC samples with higher Sc concentration two new lines appear in the spectrum. One is belonging to Sc_2O_3 clusters and the other line, a broad shoulder next to regular Sc-7 line, we assigned to a cluster where two Sc ions bind one vacancy. The vacancy in such cluster is immobile and does not contribute to ionic conductivity.

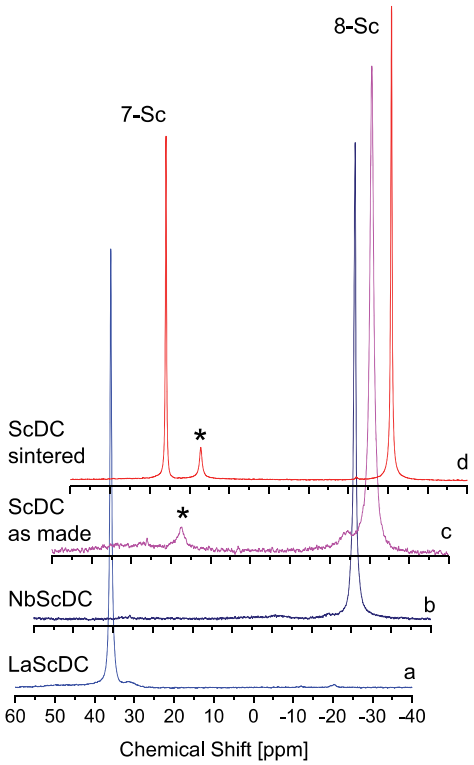

Fig. 4. ^{45}Sc MAS-NMR spectra of a) La^{3+} and Sc^{3+} co-doped sample 0.5%La0.5%ScDC, b) Nb^{5+} and Sc^{3+} co-doped sample 0.5%Nb0.5%ScDC, c) 0.5%ScDC nano-powder (grain size 25 nm) as grown at 500 °C, d) 0.5%ScDC sample sintered at 1300C. The asterisks denote spinning sidebands.

5. Conclusions

Oxygen vacancy exchange between Sc dopants in Sc-doped ceria is investigated with 2D NMR (EXSY). Normalized cross-peak intensities are plotted as a function on mixing time, the exchange rates at different

Table 2
Energy barriers for vacancy hopping in doped ceria from NMR experiments.

	ScDC	LDC	YDC
E_a	1.18 eV [This work] 1.19 eV [28] 1.2 eV [33]	0.92 eV [29]	
$E_{(1-1)}$	0.37 eV [31]		0.49 eV [22]
Theory:	0.32 eV [16]	0.85 eV [16]	0.53 eV [16]
$E_{(2-2)}$		0.45 eV [29]	

temperatures are found, and the activation energy of the process is determined through the Arrhenius analysis. The activation energy of the oxygen vacancy exchange process in Sc-doped ceria is found to be 1.18 +/− 0.10 eV. The association energy binding the vacancy to Sc^{3+} ions at the NN site was estimated to be 0.71 eV. It is considerably higher than 0.43 eV as predicted by DFT calculations [16]. We have shown that in co-doped sample 0.5%Sc0.5%LaDC the association energy binding the vacancy to Sc^{3+} is much larger than that which binds vacancy to La^{3+}. In nano-powder of ScDC all the vacancies are located at the surface of the grains.

Acknowledgments

We would like to thank Estonian Recearch Agency through the grant IUT23-7 and AS Elcogen through the contract 7-4/3/2013 for financial support.

References

[1] A. Trovarelli, C. de Leitenburg, M. Boaro, G. Dolcetti, Catal. Today 50 (1999) 353.
[2] R.J. Gorte, AIChE J 56 (2010) 1126.
[3] J. Gomes, O.A. Serra, J. Mater. Sci. 43 (2008) 546.
[4] T. Taniguchi, Y. Sonoda, M. Echikawa, Y. Watanabe, K. Hatakeyama, S. Ida, M. Koinuma, Y. Matsumoto, ACS Appl. Mater. Interfaces 4 (2012) 1010.
[5] T.S. Stefanik, H.L. Tuller, J. Eur. Ceram. Soc. 21 (2001) 1967.
[6] R. Moos, N. Izu, F. Rettig, S. Reiß, W. Shin, I. Matsubara, Sensors 11 (2011) 3439.
[7] H. Inaba, H. Tagawa, Solid State Ionics 83 (1996) 1.
[8] J.A. Kilner, Solid State Ionics 129 (2000) 13.
[9] L. Malavasi, C.A.J. Fisher, S.M. Islam, Chem. Soc. Rev. 39 (2010) 4370.
[10] D.Y. Wang, D.S. Park, J. Griffith, A.S. Nowick, Solid State Ionics 2 (1981) 95.
[11] R. Gerhardt-Anderson, A.S. Nowick, Solid State Ionics 5 (1981) 547.
[12] V. Butler, C.R.A. Catlow, B.E.F. Fender, J.H. Harding, Solid State Ionics 8 (1983) 109.
[13] J. Faber, G.C. Roux, A. Sylvestre, P. Abélard, Appl. Phys. A 49 (1989) 225.
[14] M. Mogensen, N.M. Sames, G.A. Topsett, Solid State Ionics 129 (2000) 65.
[15] D.A. Andersson, S.I. Simak, N.V. Skorodumova, I. Abrikosov, B. Johansson, Proc. Natl. Acad. Sci. U. S. A. 103 (2006) 3518.
[16] M. Nakayama, M. Martin, Phys. Chem. Chem. Phys. 11 (2009) 3241.
[17] P.P. Dholabhai, J.B. Adams, P. Crozier, R. Sharma, Phys. Chem. Chem. Phys. 12 (2010) 7904.
[18] P.P. Dholabhai, J.B. Adams, P. Crozier, R. Sharma, J. Chem. Phys. 132 (2010) 094104.
[19] A. Ismail, J. Hooper, J.B. Giorgi, T.K. Woo, Phys. Chem. Chem. Phys. 13 (2011) 6116.
[20] H. Wang, A. Chroneos, U. Schwingenschlögl, J. Chem. Phys. 138 (2013) 224705.
[21] R. Gerhardt, W.-K. Lee, A.S. Nowick, J. Phys. Chem. Solids 48 (1986) 563.
[22] K. Fuda, K. Kishio, S. Yamauchi, K. Fueki, Y. Onoda, J. Phys. Chem. Solids 45 (1984) 1253.
[23] K. Fuda, K. Kishio, S. Yamauchi, K. Fueki, J. Phys. Chem. Solids 46 (1985) 1141.
[24] S.B. Adler, J.W. Smith, J.A. Reimer, J. Chem. Phys. 98 (1993) 7613.
[25] N. Kim, J.F. Stebbins, Chem. Mater. 23 (2007) 5742.
[26] S. Kim, P. Jain, H.J. Avila-Paredes, et al., J. Mater. Chem. 20 (2010) 3855.
[27] P. Jain, H.J. Avila-Paredes, C. Gapuz, S. Sen, S. Kim, J. Phys. Chem. 113 (2009) 6553.
[28] H.J. Avila-Paredes, P. Jain, S. Sen, S. Kim, Chem. Mater. 22 (2010) 893.
[29] I. Heinmaa, T. Joon, H. Kooskora, J. Pahapill, J. Subbi, Solid State Ionics 181 (2010) 1309.
[30] J. Subbi, I. Heinmaa, R. Põder, H. Kooskora, Solid State Ionics 225 (2012) 488.
[31] J. Subbi, I. Heinmaa, R. Põder, H. Kooskora, Solid State Ionics 239 (2013) 15.
[32] M. Ando, I. Oikawa, S. Ohki, M. Tansho, T. Shimizu, H. Maekawa, H. Kiyono, Chem. Lett. 42 (2013) 57.
[33] S. Sen, T. Edwards, S.K. Kim, S. Kim, Chem. Mater. 26 (2014) 1918.
[34] J. Jeener, B.H. Meier, P. Bachmann, R.R. Ernst, J. Chem. Phys. 71 (1979) 4546.
[35] R.R. Ernst, G. Bodenhausen, A. Wokaun, Principles of Nuclear Magnetic Resonance in One and Two Dimensions, Oxford University Press, 1990.
[36] V.W.J. Verhoeven, I.M. de Shepper, G. Nachtegaal, A.P.M. Kentgens, E.M. Kelder, J. Schoonman, F.M. Mulder, Phys. Rev. Lett. 86 (2001) 4314.
[37] L.J.M. Davis, I. Heinmaa, G.R. Goward, Chem. Mater. 22 (2010) 769.
[38] W.M. O'Neill, M.A. Morris, Chem. Phys. Lett. 305 (1999) 389.

DISSERTATIONS DEFENDED AT
TALLINN UNIVERSITY OF TECHNOLOGY ON
NATURAL AND EXACT SCIENCES

1. **Olav Kongas**. Nonlinear Dynamics in Modeling Cardiac Arrhytmias. 1998.

2. **Kalju Vanatalu**. Optimization of Processes of Microbial Biosynthesis of Isotopically Labeled Biomolecules and Their Complexes. 1999.

3. **Ahto Buldas**. An Algebraic Approach to the Structure of Graphs. 1999.

4. **Monika Drews**. A Metabolic Study of Insect Cells in Batch and Continuous Culture: Application of Chemostat and Turbidostat to the Production of Recombinant Proteins. 1999.

5. **Eola Valdre**. Endothelial-Specific Regulation of Vessel Formation: Role of Receptor Tyrosine Kinases. 2000.

6. **Kalju Lott**. Doping and Defect Thermodynamic Equilibrium in ZnS. 2000.

7. **Reet Koljak**. Novel Fatty Acid Dioxygenases from the Corals *Plexaura homomalla* and *Gersemia fruticosa.* 2001.

8. **Anne Paju**. Asymmetric oxidation of Prochiral and Racemic Ketones by Using Sharpless Catalyst. 2001.

9. **Marko Vendelin**. Cardiac Mechanoenergetics *in silico*. 2001.

10. **Pearu Peterson**. Multi-Soliton Interactions and the Inverse Problem of Wave Crest. 2001.

11. **Anne Menert**. Microcalorimetry of Anaerobic Digestion. 2001.

12. **Toomas Tiivel**. The Role of the Mitochondrial Outer Membrane in *in vivo* Regulation of Respiration in Normal Heart and Skeletal Muscle Cell. 2002.

13. **Olle Hints**. Ordovician Scolecodonts of Estonia and Neighbouring Areas: Taxonomy, Distribution, Palaeoecology, and Application. 2002.

14. **Jaak Nõlvak**. Chitinozoan Biostratigrapy in the Ordovician of Baltoscandia. 2002.

15. **Liivi Kluge**. On Algebraic Structure of Pre-Operad. 2002.

16. **Jaanus Lass**. Biosignal Interpretation: Study of Cardiac Arrhytmias and Electromagnetic Field Effects on Human Nervous System. 2002.

17. **Janek Peterson**. Synthesis, Structural Characterization and Modification of PAMAM Dendrimers. 2002.

18. **Merike Vaher**. Room Temperature Ionic Liquids as Background Electrolyte Additives in Capillary Electrophoresis. 2002.

19. **Valdek Mikli**. Electron Microscopy and Image Analysis Study of Powdered Hardmetal Materials and Optoelectronic Thin Films. 2003.

20. **Mart Viljus**. The Microstructure and Properties of Fine-Grained Cermets. 2003.

21. **Signe Kask**. Identification and Characterization of Dairy-Related *Lactobacillus.* 2003

22. **Tiiu-Mai Laht**. Influence of Microstructure of the Curd on Enzymatic and Microbiological Processes in Swiss-Type Cheese. 2003.

23. **Anne Kuusksalu**. 2–5A Synthetase in the Marine Sponge *Geodia cydonium*. 2003.

24. **Sergei Bereznev**. Solar Cells Based on Polycristalline Copper-Indium Chalcogenides and Conductive Polymers. 2003.

25. **Kadri Kriis**. Asymmetric Synthesis of C_2-Symmetric Bimorpholines and Their Application as Chiral Ligands in the Transfer Hydrogenation of Aromatic Ketones. 2004.

26. **Jekaterina Reut**. Polypyrrole Coatings on Conducting and Insulating Substracts. 2004.

27. **Sven Nõmm**. Realization and Identification of Discrete-Time Nonlinear Systems. 2004.

28. **Olga Kijatkina**. Deposition of Copper Indium Disulphide Films by Chemical Spray Pyrolysis. 2004.

29. **Gert Tamberg**. On Sampling Operators Defined by Rogosinski, Hann and Blackman Windows. 2004.

30. **Monika Übner**. Interaction of Humic Substances with Metal Cations. 2004.

31. **Kaarel Adamberg**. Growth Characteristics of Non-Starter Lactic Acid Bacteria from Cheese. 2004.

32. **Imre Vallikivi**. Lipase-Catalysed Reactions of Prostaglandins. 2004.

33. **Merike Peld**. Substituted Apatites as Sorbents for Heavy Metals. 2005.

34. **Vitali Syritski**. Study of Synthesis and Redox Switching of Polypyrrole and Poly(3,4-ethylenedioxythiophene) by Using *in-situ* Techniques. 2004.

35. **Lee Põllumaa**. Evaluation of Ecotoxicological Effects Related to Oil Shale Industry. 2004.

36. **Riina Aav**. Synthesis of 9,11-Secosterols Intermediates. 2005.

37. **Andres Braunbrück**. Wave Interaction in Weakly Inhomogeneous Materials. 2005.

38. **Robert Kitt**. Generalised Scale-Invariance in Financial Time Series. 2005.

39. **Juss Pavelson**. Mesoscale Physical Processes and the Related Impact on the Summer Nutrient Fields and Phytoplankton Blooms in the Western Gulf of Finland. 2005.

40. **Olari Ilison**. Solitons and Solitary Waves in Media with Higher Order Dispersive and Nonlinear Effects. 2005.

41. **Maksim Säkki**. Intermittency and Long-Range Structurization of Heart Rate. 2005.

42. **Enli Kiipli**. Modelling Seawater Chemistry of the East Baltic Basin in the Late Ordovician–Early Silurian. 2005.

43. **Igor Golovtsov**. Modification of Conductive Properties and Processability of Polyparaphenylene, Polypyrrole and polyaniline. 2005.

44. **Katrin Laos**. Interaction Between Furcellaran and the Globular Proteins (Bovine Serum Albumin β-Lactoglobulin). 2005.

45. **Arvo Mere**. Structural and Electrical Properties of Spray Deposited Copper Indium Disulphide Films for Solar Cells. 2006.

46. **Sille Ehala**. Development and Application of Various On- and Off-Line Analytical Methods for the Analysis of Bioactive Compounds. 2006.

47. **Maria Kulp**. Capillary Electrophoretic Monitoring of Biochemical Reaction Kinetics. 2006.

48. **Anu Aaspõllu.** Proteinases from *Vipera lebetina* Snake Venom Affecting Hemostasis. 2006.

49. **Lyudmila Chekulayeva**. Photosensitized Inactivation of Tumor Cells by Porphyrins and Chlorins. 2006.

50. **Merle Uudsemaa**. Quantum-Chemical Modeling of Solvated First Row Transition Metal Ions. 2006.

51. **Tagli Pitsi**. Nutrition Situation of Pre-School Children in Estonia from 1995 to 2004. 2006.

52. **Angela Ivask**. Luminescent Recombinant Sensor Bacteria for the Analysis of Bioavailable Heavy Metals. 2006.

53. **Tiina Lõugas**. Study on Physico-Chemical Properties and Some Bioactive Compounds of Sea Buckthorn (*Hippophae rhamnoides* L.). 2006.

54. **Kaja Kasemets**. Effect of Changing Environmental Conditions on the Fermentative Growth of *Saccharomyces cerevisae* S288C: Auxo-accelerostat Study. 2006.

55. **Ildar Nisamedtinov**. Application of ^{13}C and Fluorescence Labeling in Metabolic Studies of *Saccharomyces* spp. 2006.

56. **Alar Leibak**. On Additive Generalisation of Voronoï's Theory of Perfect Forms over Algebraic Number Fields. 2006.

57. **Andri Jagomägi**. Photoluminescence of Chalcopyrite Tellurides. 2006.

58. **Tõnu Martma**. Application of Carbon Isotopes to the Study of the Ordovician and Silurian of the Baltic. 2006.

59. **Marit Kauk**. Chemical Composition of $CuInSe_2$ Monograin Powders for Solar Cell Application. 2006.

60. **Julia Kois**. Electrochemical Deposition of $CuInSe_2$ Thin Films for Photovoltaic Applications. 2006.

61. **Ilona Oja Açik**. Sol-Gel Deposition of Titanium Dioxide Films. 2007.

62. **Tiia Anmann**. Integrated and Organized Cellular Bioenergetic Systems in Heart and Brain. 2007.

63. **Katrin Trummal**. Purification, Characterization and Specificity Studies of Metalloproteinases from *Vipera lebetina* Snake Venom. 2007.

64. **Gennadi Lessin**. Biochemical Definition of Coastal Zone Using Numerical Modeling and Measurement Data. 2007.

65. **Enno Pais**. Inverse problems to determine non-homogeneous degenerate memory kernels in heat flow. 2007.

66. **Maria Borissova**. Capillary Electrophoresis on Alkylimidazolium Salts. 2007.

67. **Karin Valmsen**. Prostaglandin Synthesis in the Coral *Plexaura homomalla*: Control of Prostaglandin Stereochemistry at Carbon 15 by Cyclooxygenases. 2007.

68. **Kristjan Piirimäe**. Long-Term Changes of Nutrient Fluxes in the Drainage Basin of the Gulf of Finland – Application of the PolFlow Model. 2007.

69. **Tatjana Dedova**. Chemical Spray Pyrolysis Deposition of Zinc Sulfide Thin Films and Zinc Oxide Nanostructured Layers. 2007.

70. **Katrin Tomson**. Production of Labelled Recombinant Proteins in Fed-Batch Systems in *Escherichia coli*. 2007.

71. **Cecilia Sarmiento**. Suppressors of RNA Silencing in Plants. 2008.

72. **Vilja Mardla**. Inhibition of Platelet Aggregation with Combination of Antiplatelet Agents. 2008.

73. **Maie Bachmann**. Effect of Modulated Microwave Radiation on Human Resting Electroencephalographic Signal. 2008.

74. **Dan Hüvonen**. Terahertz Spectroscopy of Low-Dimensional Spin Systems. 2008.

75. **Ly Villo**. Stereoselective Chemoenzymatic Synthesis of Deoxy Sugar Esters Involving *Candida antarctica* Lipase B. 2008.

76. **Johan Anton**. Technology of Integrated Photoelasticity for Residual Stress Measurement in Glass Articles of Axisymmetric Shape. 2008.

77. **Olga Volobujeva**. SEM Study of Selenization of Different Thin Metallic Films. 2008.

78. **Artur Jõgi**. Synthesis of 4'-Substituted 2,3'-dideoxynucleoside Analogues. 2008.

79. **Mario Kadastik**. Doubly Charged Higgs Boson Decays and Implications on Neutrino Physics. 2008.

80. **Fernando Pérez-Caballero**. Carbon Aerogels from 5-Methylresorcinol-Formaldehyde Gels. 2008.

81. **Sirje Vaask**. The Comparability, Reproducibility and Validity of Estonian Food Consumption Surveys. 2008.

82. **Anna Menaker**. Electrosynthesized Conducting Polymers, Polypyrrole and Poly(3,4-ethylenedioxythiophene), for Molecular Imprinting. 2009.

83. **Lauri Ilison**. Solitons and Solitary Waves in Hierarchical Korteweg-de Vries Type Systems. 2009.

84. **Kaia Ernits**. Study of In_2S_3 and ZnS Thin Films Deposited by Ultrasonic Spray Pyrolysis and Chemical Deposition. 2009.

85. **Veljo Sinivee**. Portable Spectrometer for Ionizing Radiation "Gammamapper". 2009.

86. **Jüri Virkepu**. On Lagrange Formalism for Lie Theory and Operadic Harmonic Oscillator in Low Dimensions. 2009.

87. **Marko Piirsoo**. Deciphering Molecular Basis of Schwann Cell Development. 2009.

88. **Kati Helmja**. Determination of Phenolic Compounds and Their Antioxidative Capability in Plant Extracts. 2010.

89. **Merike Sõmera**. Sobemoviruses: Genomic Organization, Potential for Recombination and Necessity of P1 in Systemic Infection. 2010.

90. **Kristjan Laes**. Preparation and Impedance Spectroscopy of Hybrid Structures Based on $CuIn_3Se_5$ Photoabsorber. 2010.

91. **Kristin Lippur**. Asymmetric Synthesis of 2,2'-Bimorpholine and its 5,5'-Substituted Derivatives. 2010.

92. **Merike Luman**. Dialysis Dose and Nutrition Assessment by an Optical Method. 2010.

93. **Mihhail Berezovski**. Numerical Simulation of Wave Propagation in Heterogeneous and Microstructured Materials. 2010.

94. **Tamara Aid-Pavlidis**. Structure and Regulation of BDNF Gene. 2010.

95. **Olga Bragina**. The Role of Sonic Hedgehog Pathway in Neuro- and Tumorigenesis. 2010.

96. **Merle Randrüüt**. Wave Propagation in Microstructured Solids: Solitary and Periodic Waves. 2010.

97. **Marju Laars**. Asymmetric Organocatalytic Michael and Aldol Reactions Mediated by Cyclic Amines. 2010.

98. **Maarja Grossberg**. Optical Properties of Multinary Semiconductor Compounds for Photovoltaic Applications. 2010.

99. **Alla Maloverjan**. Vertebrate Homologues of Drosophila Fused Kinase and Their Role in Sonic Hedgehog Signalling Pathway. 2010.

100. **Priit Pruunsild**. Neuronal Activity-Dependent Transcription Factors and Regulation of Human *BDNF* Gene. 2010.

101. **Tatjana Knjazeva**. New Approaches in Capillary Electrophoresis for Separation and Study of Proteins. 2011.

102. **Atanas Katerski**. Chemical Composition of Sprayed Copper Indium Disulfide Films for Nanostructured Solar Cells. 2011.

103. **Kristi Timmo.** Formation of Properties of $CuInSe_2$ and $Cu_2ZnSn(S,Se)_4$ Monograin Powders Synthesized in Molten KI. 2011.
104. **Kert Tamm**. Wave Propagation and Interaction in Mindlin-Type Microstructured Solids: Numerical Simulation. 2011.
105. **Adrian Popp**. Ordovician Proetid Trilobites in Baltoscandia and Germany. 2011.
106. **Ove Pärn**. Sea Ice Deformation Events in the Gulf of Finland and This Impact on Shipping. 2011.
107. **Germo Väli**. Numerical Experiments on Matter Transport in the Baltic Sea. 2011.
108. **Andrus Seiman**. Point-of-Care Analyser Based on Capillary Electrophoresis. 2011.
109. **Olga Katargina**. Tick-Borne Pathogens Circulating in Estonia (Tick-Borne Encephalitis Virus, *Anaplasma phagocytophilum*, *Babesia* Species): Their Prevalence and Genetic Characterization. 2011.

110. **Ingrid Sumeri**. The Study of Probiotic Bacteria in Human Gastrointestinal Tract Simulator. 2011.

111. **Kairit Zovo**. Functional Characterization of Cellular Copper Proteome. 2011.

112. **Natalja Makarytsheva**. Analysis of Organic Species in Sediments and Soil by High Performance Separation Methods. 2011.

113. **Monika Mortimer**. Evaluation of the Biological Effects of Engineered Nanoparticles on Unicellular Pro- and Eukaryotic Organisms. 2011.

114. **Kersti Tepp**. Molecular System Bioenergetics of Cardiac Cells: Quantitative Analysis of Structure-Function Relationship. 2011.

115. **Anna-Liisa Peikolainen**. Organic Aerogels Based on 5-Methylresorcinol. 2011.

116. **Leeli Amon**. Palaeoecological Reconstruction of Late-Glacial Vegetation Dynamics in Eastern Baltic Area: A View Based on Plant Macrofossil Analysis. 2011.

117. **Tanel Peets**. Dispersion Analysis of Wave Motion in Microstructured Solids. 2011.

118. **Liina Kaupmees**. Selenization of Molybdenum as Contact Material in Solar Cells. 2011.

119. **Allan Olspert**. Properties of VPg and Coat Protein of Sobemoviruses. 2011.

120. **Kadri Koppel**. Food Category Appraisal Using Sensory Methods. 2011.

121. **Jelena Gorbatšova**. Development of Methods for CE Analysis of Plant Phenolics and Vitamins. 2011.

122. **Karin Viipsi**. Impact of EDTA and Humic Substances on the Removal of Cd and Zn from Aqueous Solutions by Apatite. 2012.

123. **David Schryer**. Metabolic Flux Analysis of Compartmentalized Systems Using Dynamic Isotopologue Modeling. 2012.

124. **Ardo Illaste**. Analysis of Molecular Movements in Cardiac Myocytes. 2012.

125. **Indrek Reile**. 3-Alkylcyclopentane-1,2-Diones in Asymmetric Oxidation and Alkylation Reactions. 2012.

126. **Tatjana Tamberg**. Some Classes of Finite 2-Groups and Their Endomorphism Semigroups. 2012.

127. **Taavi Liblik**. Variability of Thermohaline Structure in the Gulf of Finland in Summer. 2012.

128. **Priidik Lagemaa**. Operational Forecasting in Estonian Marine Waters. 2012.

129. **Andrei Errapart**. Photoelastic Tomography in Linear and Non-linear Approximation. 2012.

130. **Külliki Krabbi**. Biochemical Diagnosis of Classical Galactosemia and Mucopolysaccharidoses in Estonia. 2012.

131. **Kristel Kaseleht**. Identification of Aroma Compounds in Food using SPME-GC/MS and GC-Olfactometry. 2012.

132. **Kristel Kodar**. Immunoglobulin G Glycosylation Profiling in Patients with Gastric Cancer. 2012.

133. **Kai Rosin**. Solar Radiation and Wind as Agents of the Formation of the Radiation Regime in Water Bodies. 2012.

134. **Ann Tiiman**. Interactions of Alzheimer's Amyloid-Beta Peptides with Zn(II) and Cu(II) Ions. 2012.

135. **Olga Gavrilova**. Application and Elaboration of Accounting Approaches for Sustainable Development. 2012.

136. **Olesja Bondarenko**. Development of Bacterial Biosensors and Human Stem Cell-Based *In Vitro* Assays for the Toxicological Profiling of Synthetic Nanoparticles. 2012.

137. **Katri Muska**. Study of Composition and Thermal Treatments of Quaternary Compounds for Monograin Layer Solar Cells. 2012.

138. **Ranno Nahku**. Validation of Critical Factors for the Quantitative Characterization of Bacterial Physiology in Accelerostat Cultures. 2012.

139. **Petri-Jaan Lahtvee**. Quantitative Omics-level Analysis of Growth Rate Dependent Energy Metabolism in *Lactococcus lactis*. 2012.

140. **Kerti Orumets**. Molecular Mechanisms Controlling Intracellular Glutathione Levels in Baker's Yeast *Saccharomyces cerevisiae* and its Random Mutagenized Glutathione Over-Accumulating Isolate. 2012.

141. **Loreida Timberg**. Spice-Cured Sprats Ripening, Sensory Parameters Development, and Quality Indicators. 2012.

142. **Anna Mihhalevski**. Rye Sourdough Fermentation and Bread Stability. 2012.

143. **Liisa Arike**. Quantitative Proteomics of *Escherichia coli*: From Relative to Absolute Scale. 2012.

144. **Kairi Otto**. Deposition of In_2S_3 Thin Films by Chemical Spray Pyrolysis. 2012.

145. **Mari Sepp**. Functions of the Basic Helix-Loop-Helix Transcription Factor TCF4 in Health and Disease. 2012.

146. **Anna Suhhova**. Detection of the Effect of Weak Stressors on Human Resting Electroencephalographic Signal. 2012.

147. **Aram Kazarjan**. Development and Production of Extruded Food and Feed Products Containing Probiotic Microorganisms. 2012.

148. **Rivo Uiboupin**. Application of Remote Sensing Methods for the Investigation of Spatio-Temporal Variability of Sea Surface Temperature and Chlorophyll Fields in the Gulf of Finland. 2013.

149. **Tiina Kriščiunaite**. A Study of Milk Coagulability. 2013.

150. **Tuuli Levandi**. Comparative Study of Cereal Varieties by Analytical Separation Methods and Chemometrics. 2013.

151. **Natalja Kabanova**. Development of a Microcalorimetric Method for the Study of Fermentation Processes. 2013.

152. **Himani Khanduri**. Magnetic Properties of Functional Oxides. 2013.

153. **Julia Smirnova**. Investigation of Properties and Reaction Mechanisms of Redox-Active Proteins by ESI MS. 2013.

154. **Mervi Sepp**. Estimation of Diffusion Restrictions in Cardiomyocytes Using Kinetic Measurements. 2013.

155. **Kersti Jääger**. Differentiation and Heterogeneity of Mesenchymal Stem Cells. 2013.

156. **Victor Alari**. Multi-Scale Wind Wave Modeling in the Baltic Sea. 2013.

157. **Taavi Päll**. Studies of CD44 Hyaluronan Binding Domain as Novel Angiogenesis Inhibitor. 2013.

158. **Allan Niidu**. Synthesis of Cyclopentane and Tetrahydrofuran Derivatives. 2013.

159. **Julia Geller**. Detection and Genetic Characterization of *Borrelia* Species Circulating in Tick Population in Estonia. 2013.

160. **Irina Stulova**. The Effects of Milk Composition and Treatment on the Growth of Lactic Acid Bacteria. 2013.

161. **Jana Holmar**. Optical Method for Uric Acid Removal Assessment During Dialysis. 2013.

162. **Kerti Ausmees**. Synthesis of Heterobicyclo[3.2.0]heptane Derivatives *via* Multicomponent Cascade Reaction. 2013.

163. **Minna Varikmaa**. Structural and Functional Studies of Mitochondrial Respiration Regulation in Muscle Cells. 2013.

164. **Indrek Koppel**. Transcriptional Mechanisms of BDNF Gene Regulation. 2014.

165. **Kristjan Pilt**. Optical Pulse Wave Signal Analysis for Determination of Early Arterial Ageing in Diabetic Patients. 2014.

166. **Andres Anier**. Estimation of the Complexity of the Electroencephalogram for Brain Monitoring in Intensive Care. 2014.

167. **Toivo Kallaste**. Pyroclastic Sanidine in the Lower Palaeozoic Bentonites – A Tool for Regional Geological Correlations. 2014.

168. **Erki Kärber**. Properties of ZnO-nanorod/In_2S_3/$CuInS_2$ Solar Cell and the Constituent Layers Deposited by Chemical Spray Method. 2014.

169. **Julia Lehner**. Formation of Cu_2ZnSnS_4 and $Cu_2ZnSnSe_4$ by Chalcogenisation of Electrochemically Deposited Precursor Layers. 2014.

170. **Peep Pitk**. Protein- and Lipid-rich Solid Slaughterhouse Waste Anaerobic Co-digestion: Resource Analysis and Process Optimization. 2014.

171. **Kaspar Valgepea**. Absolute Quantitative Multi-omics Characterization of Specific Growth Rate-dependent Metabolism of *Escherichia coli*. 2014.

172. **Artur Noole**. Asymmetric Organocatalytic Synthesis of 3,3'-Disubstituted Oxindoles. 2014.

173. **Robert Tsanev**. Identification and Structure-Functional Characterisation of the Gene Transcriptional Repressor Domain of Human Gli Proteins. 2014.

174. **Dmitri Kartofelev**. Nonlinear Sound Generation Mechanisms in Musical Acoustic. 2014.

175. **Sigrid Hade**. GIS Applications in the Studies of the Palaeozoic Graptolite Argillite and Landscape Change. 2014.

176. **Agne Velthut-Meikas**. Ovarian Follicle as the Environment of Oocyte Maturation: The Role of Granulosa Cells and Follicular Fluid at Pre-Ovulatory Development. 2014.

177. **Kristel Hälvin**. Determination of B-group Vitamins in Food Using an LC-MS Stable Isotope Dilution Assay. 2014.

178. **Mailis Päri**. Characterization of the Oligoadenylate Synthetase Subgroup from Phylum Porifera. 2014.

179. **Jekaterina Kazantseva**. Alternative Splicing of *TAF4*: A Dynamic Switch between Distinct Cell Functions. 2014.

180. **Jaanus Suurväli**. Regulator of G Protein Signalling 16 (RGS16): Functions in Immunity and Genomic Location in an Ancient MHC-Related Evolutionarily Conserved Synteny Group. 2014.

181. **Ene Viiard**. Diversity and Stability of Lactic Acid Bacteria During Rye Sourdough Propagation. 2014.

182. **Kristella Hansen**. Prostaglandin Synthesis in Marine Arthropods and Red Algae. 2014.

183. **Helike Lõhelaid**. Allene Oxide Synthase-lipoxygenase Pathway in Coral Stress Response. 2015.

184. **Normunds Stivrinš**. Postglacial Environmental Conditions, Vegetation Succession and Human Impact in Latvia. 2015.

185. **Mary-Liis Kütt**. Identification and Characterization of Bioactive Peptides with Antimicrobial and Immunoregulating Properties Derived from Bovine Colostrum and Milk. 2015.

186. **Kazbulat Šogenov**. Petrophysical Models of the CO_2 Plume at Prospective Storage Sites in the Baltic Basin. 2015.

187. **Taavi Raadik**. Application of Modulation Spectroscopy Methods in Photovoltaic Materials Research. 2015.